AD-A112 244 NAVAL OCEAN SYSTEMS CENTER SAN DIEGO CA F/G 17/2
OPTICAL COMMUNICATIONS USING RETROMODULATION TECHNIQUES.(U)
SEP 80 R P BOCKER, B M MEANA, B C MOORADIAN
UNCLASSIFIED NOSC/TR-614 NL

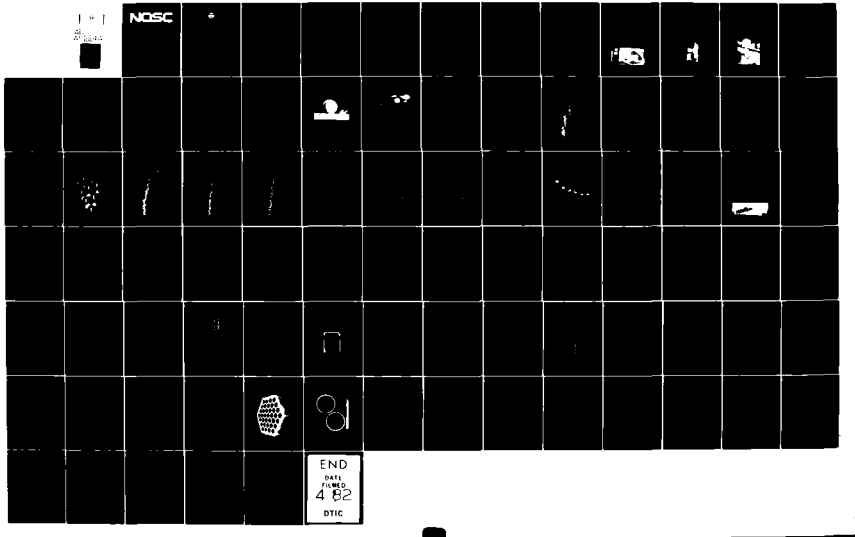

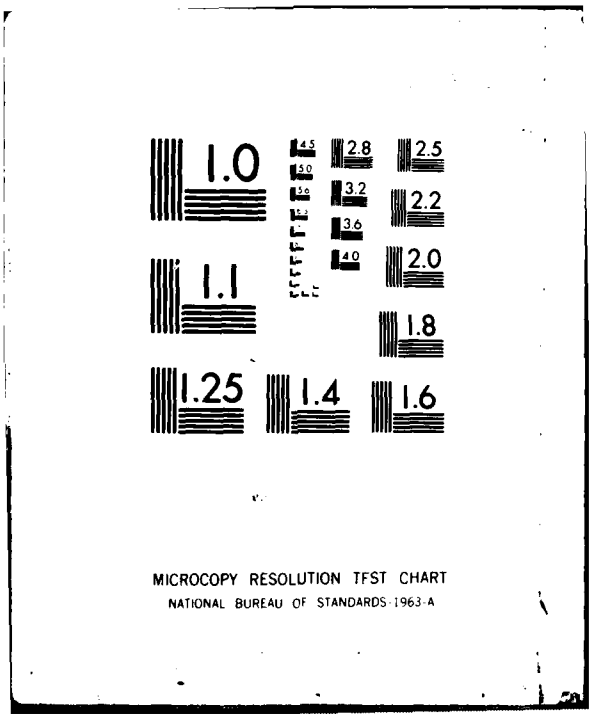
1.0
1.1
1.25
1.4
1.6
1.8
2.0
2.2
2.5
2.8
3.2
3.6
4.0
4.5
5.0
MICROCOPY RESOLUTION TFST CHART
NATIONAL BUREAU OF STANDARDS-1963-A

(11)

NOSC

NOSC TR 614

Technical Report 614

OPTICAL COMMUNICATIONS USING RETROMODULATION TECHNIQUES

RP Bocker
GM Meana
GC Mooradian

September 1980

Final Report: June 1978 - August 1979

Prepared for
Naval Electronic Systems Command

Approved for public release; distribution unlimited

NAVAL OCEAN SYSTEMS CENTER
SAN DIEGO, CALIFORNIA 92152

NAVAL OCEAN SYSTEMS CENTER, SAN DIEGO, CA 92152

AN ACTIVITY OF THE NAVAL MATERIAL COMMAND

SL GUILLE, CAPT, USN
Commander

HL BLOOD
Technical Director

ADMINISTRATIVE INFORMATION

The work reported herein was conducted during FY 78 and 79 for the Naval Electronic Systems Command under the Survivable Communications Block Program, program element 62721N, subproject XF2182091.

Released by
MS Kvigne, Head
Communications Research
and Technology Division

Under authority of
HD Smith, Head
Communications Systems
and Technology Department

ACKNOWLEDGEMENTS

The authors would like to thank the Naval Electronic Systems Command for their support of this program. Also special thanks go to R. Anderson, K. Davies, R. Krautwald, J. Marabeas, M. Monahan, R. Patterson, R. Pierce, L Ruth, E. Schumacher, H. Taylor, and M. Taylor for their help on various problem areas in this program.

UNCLASSIFIED

SECURITY CLASSIFICATION OF THIS PAGE *(When Data Entered)*

REPORT DOCUMENTATION PAGE		READ INSTRUCTIONS BEFORE COMPLETING FORM
1. REPORT NUMBER NOSC Technical Report 614 (TR 614)	2. GOVT ACCESSION NO. AD-A112 244	3. RECIPIENT'S CATALOG NUMBER
4. TITLE *(and Subtitle)* OPTICAL COMMUNICATIONS USING RETROMODULATION TECHNIQUES		5. TYPE OF REPORT & PERIOD COVERED Final Report: June 1978 – August 1979 6. PERFORMING ORG. REPORT NUMBER
7. AUTHOR(s) RP Bocker GM Meana GC Mooradian		8. CONTRACT OR GRANT NUMBER(s)
9. PERFORMING ORGANIZATION NAME AND ADDRESS Naval Ocean Systems Center San Diego, CA 92152		10. PROGRAM ELEMENT, PROJECT, TASK AREA & WORK UNIT NUMBERS 62721N, XF2182091
11. CONTROLLING OFFICE NAME AND ADDRESS Naval Electronic Systems Command Washington, DC		12. REPORT DATE September 1980 13. NUMBER OF PAGES 86
14. MONITORING AGENCY NAME & ADDRESS*(if different from Controlling Office)*		15. SECURITY CLASS. *(of this report)* Unclassified 15a. DECLASSIFICATION/DOWNGRADING SCHEDULE

16. DISTRIBUTION STATEMENT *(of this Report)*

Approved for public release; distribution unlimited

17. DISTRIBUTION STATEMENT *(of the abstract entered in Block 20, if different from Report)*

18. SUPPLEMENTARY NOTES

19. KEY WORDS *(Continue on reverse side if necessary and identify by block number)*

Optical communications
Laser communications
Lithium niobate
Air-to-underwater communications
PLZT
Communications security
Antijamming measure

20. ABSTRACT *(Continue on reverse side if necessary and identify by block number)*

Experiments were conducted in two-way voice communications by means of an optical system employing retromodulation techniques. Several materials were used as large-aperture modulators: lithium niobate and lead lanthanum zirconate titanate. Results are reported concerning means of reducing scintillation effects. The effects at the air-water interface are described.

DD FORM 1 JAN 73 1473 EDITION OF 1 NOV 68 IS OBSOLETE
S/N 0102-LF-014-6601

UNCLASSIFIED

SECURITY CLASSIFICATION OF THIS PAGE *(When Data Entered)*

CONTENTS

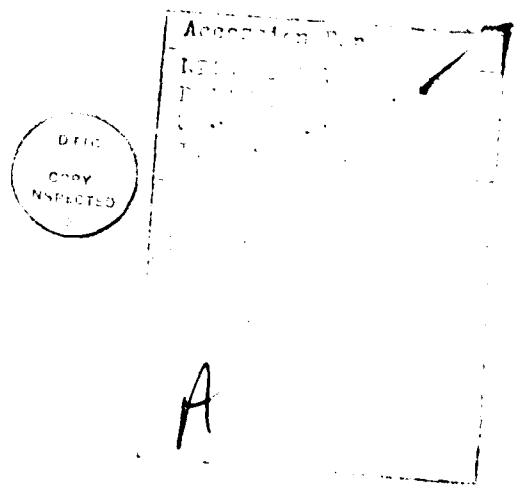

INTRODUCTION

The Navy currently has no means of communication which is not significantly susceptible to jamming, intercept, spoofing, and direction-finding. At present, the fleet cannot perform maneuvers in the presence of a hostile observer without divulging the radio frequency in use, thereby yielding information on frequencies against which the hostile observer could employ his disruptive or deceptive countermeasures. In addition, current radio frequency communications systems suffer from limitations due to limited data rates, spectrum crowding, vulnerability due to omnidirectionality, high cost, and large size, weight, and power requirements.

This has forced communications systems to utilize higher and higher portions of the electromagnetic spectrum, including optical frequencies. The use of the optical portion of the spectrum for communications is not new. Many laboratory and limited field demonstrations have been conducted. However, development of reliable military optical communications links operating through a realistic atmosphere and on real naval platforms has yet to be accomplished. NOSC and other laboratories have, for the last several years, pursued optical communications with the intent to address real Navy and DoD communication requirements. This has resulted in the development of a broad technological base from which to develop optical communications equipment optimized for naval requirements and operational platforms. However, this technology is neither simple, inexpensive, nor easy to support when a system using it is deployed.

For naval applications, requirements such as antijam (AJ) and low probability of intercept (LPI) become dominant, and techniques for operation from rolling, pitching ships in adverse atmospheres, with rapid acquisition call-up times, are mandatory. Size, weight, prime power, invulnerability to radio frequency interference, and relief from spectrum crowding also become important system considerations. Bandwidth, however, while significant, is perhaps the least required capability for naval applications. Therefore, confronted by the operations requirements and the technology available, NOSC has responded with a suite of systems exploiting optical frequencies, including, for example, SAOCS (Submarine to Aircraft Optical Communications System) and OCCULT (Optical Covert Communications Using Laser Transceivers).

While these systems address diverse requirements, utilize different optical communication technologies, and are characterized by a wide level of complexities, they share one feature. This is the principle that the inherent high-antenna-gain properties with optical frequencies can be used to compensate for moderate power sources. The inherent antenna gain permits system power budgets to look encouraging, as well as providing AJ and LPI capabilities at the expense of required narrow beams and system complexity. This, then, increases pointing and tracking requirements and increases severely the acquisition problems of the links. The retromodulation technique described in this report represents an attempt to utilize the high antenna gain of optical antennas while simultaneously reducing the system complexity of one part of the link.

BACKGROUND

Optical communications systems, like other types, require terminals at both ends of the communication link for the two-way transfer of information. Shown in Fig. 1 is a schematic depicting a conventional optical communications system. It is noted that the two active terminals comprising the system are basically identical. The key components making up either one of these terminals are a laser transmitter, an optical modulator, pointing and tracking optics, an optical collector, an optical detector, and supporting electronics. The conventional optical communications system depicted in Fig. 1 can be simplified through the use of an optical retroreflector. A retroreflector is a device having the property of returning light incident upon it back along the same path with a divergence limited only by the diffraction of the retroreflector itself (see Fig. 2). If the reflected signal is then modulated, an extremely useful communications tool is possible, using a passive component as one element in a two-way system. The total system complexity is then significantly reduced. For example, only a single optical light source is required with a pointing and tracking system. The passive terminal reciprocal pointing and tracking is accomplished automatically. Also, since the link requires only the active terminal to be pointed at the passive terminal, spatial acquisition is greatly aided. When a simple, wide-angle receiver is placed in conjunction with the modulated retroreflector, a passive transceiver is produced. This is a communications transceiver that contains no active radiators and no tracking systems.

The basic optical communications system employing the retromodulation concept is shown schematically in Fig. 3. Although there are many variations on this scheme, all operate on the same principle. The active terminal, so termed because it actively emits radiation, is composed of a light source, a modulator operating on, perhaps, a subcarrier to discriminate against the modulated retroreturn subcarrier frequency, a receiver coaxial with and boresighted to the transmitter axis, and a pointing and tracking system. The passive terminal, so termed because it reflects only radiation that is incident on it and does not generate any, is composed of a retroreflector with an optical modulator placed in front of it to encode the information on a separate subcarrier, plus a simple wide-angle receiver. The basic mode of operation is for the active terminal to transmit information to the passive terminal in a conventional manner and to simultaneously interrogate the passive terminal. It is the concept of interrogation of the passive terminal that leads to an important characteristic of the system. It allows the active terminal located on a single platform to interrogate and communicate to many passive terminals, but by fundamentals it prohibits the passive terminal from initiating communications. It is noted that, since the beam returned from the retroreflector is independent of the source-beam divergence used to illuminate it, some applications may permit an omnidirectional source, thereby simplifying the active terminal. In addition, the passive terminal operates over a wide range of incidence angles and is insensitive to the nature of the incident light, whether it be from a highly coherent laser or an incoherent incandescent light of wide or narrow spectral bandwidth. Additional discussion on the retromodulation technique with potential areas of application may be found in Ref. 1.

All components required to synthesize an optical communications system employing the retromodulation technique are off-the-shelf components, except for one, namely, the large-area modulator required in front of the retroreflector in the passive terminal. In FY77 a study and experimental investigation was performed at NOSC using internal IR/IED funds

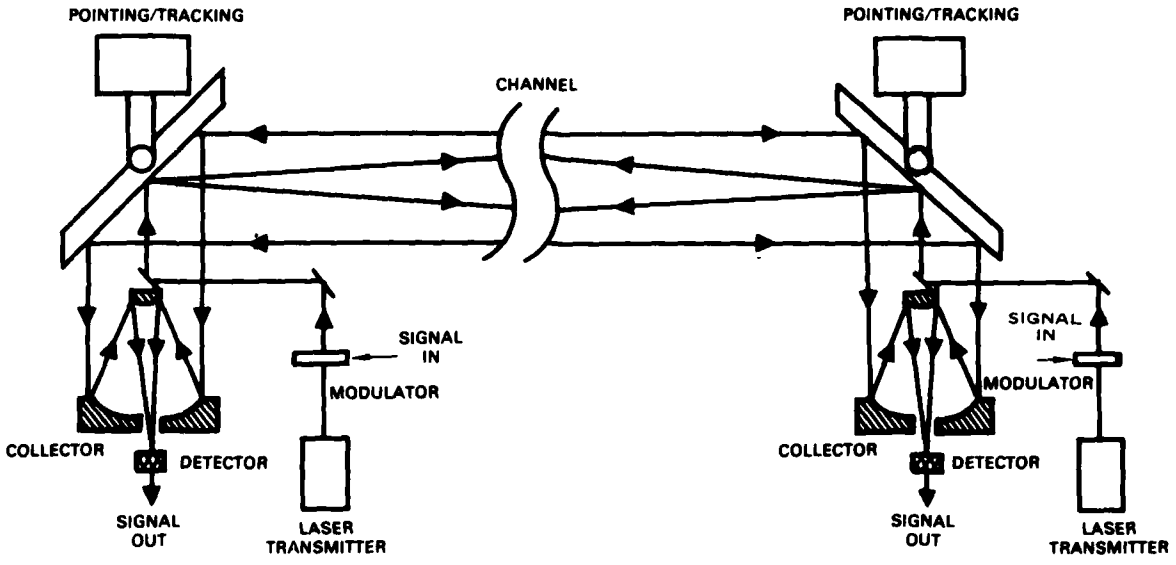

Figure 1. Conventional optical communications system.

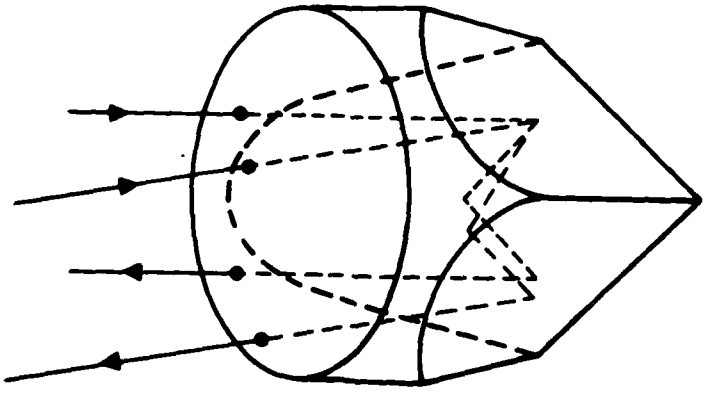

Figure 2. Light path through a corner-cube retroreflector.

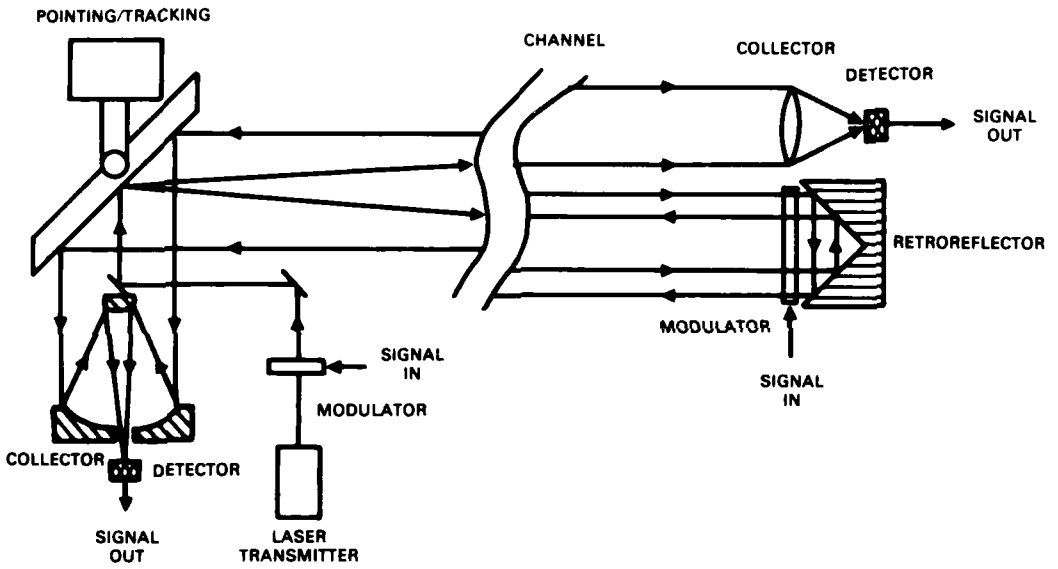

Figure 3. Optical communications system employing retromodulation technique.

to identify, classify, and evaluate various active optical materials for their potential use as a large-aperture, wide-acceptance-angle modulator (Ref. 2). As a result of this program, it was found that two optical materials showed a great deal of promise as large-aperture modulator candidates with good field-of-view properties. These materials are lithium niobate ($LiNbO_3$), an electrooptical Pockels crystal, and lead lanthanum zirconate titanate (PLZT), a ferroelectric ceramic.

NELEX 310, recognizing the potential usefulness of the retromodulation technique for special naval communications applications, authorized its incorporation into the Electrooptical Techniques for Survivable Communications Block Program in FY78. A technology base program was initiated for atmospheric line-of-sight scenarios, with primary emphasis on extending the useful operating range, extending the angular coverage of the passive terminal, determining the trade-offs between incoherent light and coherent laser light, and reducing atmospheric scintillation effects through aperture averaging. In FY79 emphasis was shifted toward scenarios involving air-to-underwater optical communications, where the passive terminal was placed underwater. Emphasis was placed on the effects of a randomly varying air-water interface on the optical communications system's performance. In addition, NELEX 304 sponsored work on the development of a very large optical modulator for underwater applications. Key experiments performed in FY78 and FY79 addressing the issues at hand and the results of the very-large-aperture development program (see Appendix E) are described in this report.

Four experiments were performed which will be described in much greater detail: 1) a demonstration of voice communications over a retromodulated light beam, 2) the

scintillation effects on retroreflected light beams, 3) the effects of aperture averaging as a means of reducing scintillation effects, and 4) the air-water interface effects on retroreflected optical light beams.

EXPERIMENT 1

VOICE COMMUNICATIONS OVER A RETROREFLECTED OPTICAL LIGHT BEAM

OBJECTIVE

The principal objective of this experiment was to design, fabricate, and assemble an optical communications preprototype system using the retromodulation concept to transmit and receive voice information over a realistic line-of-sight atmospheric communications channel.

APPROACH

Three optical terminals were fabricated. Two of these terminals were active in nature, one using a helium-neon laser transmitter (0.633 μm) and the other an incoherent white-light source. Two active terminals were fabricated for purposes of comparison. The third terminal fabricated was a hand-held battery-operated passive terminal. Off-the-shelf components were used for all terminals. However, the large-area modulator required in the passive terminal was fabricated and tested by NOSC. As indicated, either lithium niobate or lead lanthanum zirconate titanate could be used as the large-area modulator. Lithium niobate was selected at the time due to its superior optical quality, hence higher antenna gain, compared with PLZT ceramic.

Figure 4 shows the passive terminal designed, fabricated, and assembled at NOSC. This terminal is embodied in a unit having dimensions of 6.6 by 8.2 by 22.8 cm. All optics

Figure 4. Hand-held battery-operated passive optical communications terminal employing the retromodulation principle.

and driver and support electronics are totally contained in this unit. The upper optics port shown in Fig. 4 contains a simple lens element collector and a solid-state photodiode detector. In addition, a narrowband (~30 Å FWHM)* interference filter can be easily inserted or retracted from this port to discriminate against background light radiation if the terminal is used in daytime. The lower port contains the $LiNbO_3$ crystal modulator and a solid-glass corner-cube retroreflector with silver-coated rear reflecting surfaces. The $LiNbO_3$ crystal used in the passive terminal has the dimensions 4.5 by 0.3 by 5.5 cm. Aluminum interdigital electrodes were fabricated on one of the large flat surfaces of the crystal as a means for electrical excitation. The overall antenna gain of the $LiNbO_3$ and corner-cube combination is over 110 dB. A detailed description of the theory of operation of the $LiNbO_3$ crystal along with laboratory experimental results may be found in Appendix C of this report. As indicated in Appendix C, the optical transmission of the crystal for the retroreflected beam obeys a cosine square type response to applied voltage. The half-wave voltage for this crystal configuration is approximately 800 V. Hence, in order to operate the crystal in the linear region of the cosine square curve, the crystal needs to be biased to a dc level of about 400 V, then driven about this bias with the desired modulated ac signal (voice). The driver electronics were so designed that an input of 10 V dc to the circuitry would yield a 400-V potential difference across the electrodes of the modulator. In addition, an input ac modulating signal of 1 V peak-to-peak would give rise to a 300-V peak-to-peak signal across the modulator. The amplifier used for this purpose is essentially a tuned circuit device with a moderate Q-value about some preselected frequency. The operating frequency chosen was 18 kHz with a 5-kHz bandwidth. This operating frequency is adjustable by varying the ferrite core of the required step-up transformer. The transformer is a 40/900 turn step-up and is fed by two current amplifiers driven 180 deg out of phase to allow for the wide ac voltage swing. The load of the amplifiers, namely, the lithium niobate crystal modulator, has a capacitance of about 175 pF.

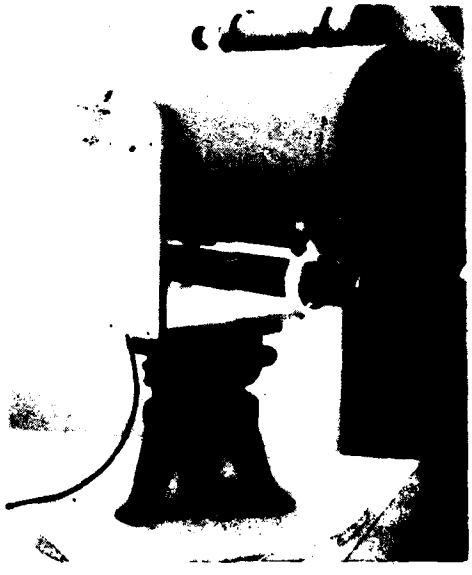

Figure 5. He[illegible]on[illegible] active optical communications [illegible]inal.

*Full-width half-maximum.

The active terminal utilizing the helium-neon laser is of conventional design (Fig. 5). The laser has an output power of 3.5 mW at 0.633 μm and is boresighted via folding mirrors to be coaxial with the optical axis of a 20-cm-aperture Cassegrainian receiver telescope. The voice signal information is transmitted over the 0.633-μm laser beam by frequency modulating (FM) the laser current. A 63-kHz subcarrier with 5-kHz bandwidth was employed. The return beam from the passive terminal is detected at the focal plane of the receiver telescope with a silicon photodiode detector using the method of direct energy detection. The active terminal operates with a modulation format that is relatively narrowband FM (modulation index equal to 1.0) and with conventional phase-lock loop audio demodulation. As the receiver noise is parabolic with frequency, preemphasis is applied to the modulator and deemphasis to the receiver. In addition, both the active and passive terminals have AGC in the audio-modulation circuits to prevent overmodulation.

The second active terminal assembled utilizes an incoherent broadband white-light source (Fig. 6). In particular, a 1-kW Army xenon short-arc searchlight, manufactured by Xerox Corporation, was retrofitted with an optical receiver. The receiver consisted of a 12.5-cm-diameter Fresnel plastic collecting lens and a solid-state silicon photodiode detector located in the rear focal plane of the lens. No optical blocking filters were employed. No attempt was made to modulate the searchlight current*, so that only one-way communication

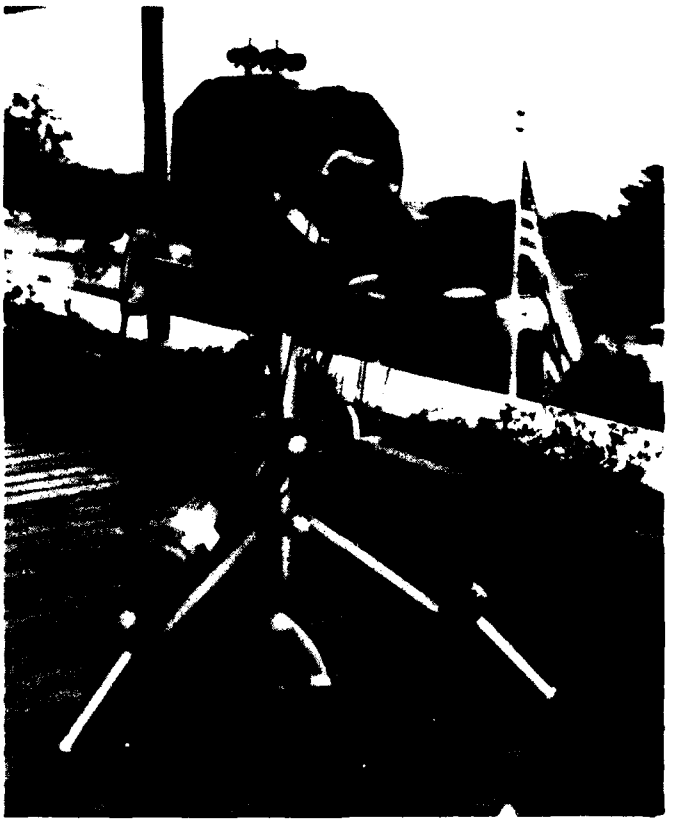

Figure 6. Xenon short-arc active optical communications terminal.

*Searchlight current modulation had already been studied at NUSC. See Ref. 3.

from the passive terminal to the active terminal was possible when the xenon searchlight was employed. The receiver driver electronics in the active terminal employing the xenon searchlight are identical to those employed in the terminal using the helium-neon laser.

Table 1 contains pertinent information describing the parameters associated with the various terminals. This information, used with the system equations described in Appendix A for predicting signal-to-noise ratios for an atmospheric line-of-sight optical communications system employing retromodulation techniques, can be used to give insights into overall system performance when used in a realistic communication channel.

RESULTS

An optical communications test link was established at NOSC between buildings 4 and 593. The distance between these buildings is approximately 1.6 km. The first set of measurements was concerned with determining the validity of the signal-to-noise equation presented in Appendix A for predicting system performance when using the retromodulation technique for direct energy detection. During mid-June 1978 initial measurements were made on clear days in the early morning, when atmospheric scintillation was still at a minimum. The detector output of the helium-neon laser active terminal was monitored with a spectrum

Table 1.

Terminal Parameters*.

Helium-Neon Laser Active Terminal			Hand-Held Passive Terminal		
λ_c	=	6328×10^{-8} cm	ϕ_m	=	8 arc-s
f_c	=	4.74×10^{14} s^{-1}	Ω_m	=	4.7×10^{-9} sr
P_a	=	3.5×10^{-3} W	A_m	=	20 cm^2
ϕ_a	=	160 arc-s	E_m	=	0.3
Ω_a	=	1.87×10^{-6} sr	M_m	=	0.9
A_d	=	295 cm^2			
E_d	=	0.9			
G	=	1.0			
S_d	=	0.35 A/W			
η	=	0.7			
B_o	=	5000 s^{-1}			
I_d	=	10^{-7} A			
T	=	300 °K			
R_l	=	100 Ω			

* These parameters are defined in Appendix A.

analyzer. The signal-to-noise ratio (SNR) consistently measured between +30 and +34 dB. Using the equations in Appendix A with the parametric values listed in Table 1 in conjunction with the following information:

Atmospheric extinction coefficient	(2.5×10^{-4} m^{-1})
Range between terminals	(1.6 km)
Blue-sky spectral irradiance	(2.4×10^{-6} W/cm^2 - Å)
Blocking filter bandwidth	(30 Å)
Active terminal receiver area	(295 cm^2)

we find the following:

$$P_S = 3.9 \times 10^{-7} W$$
$$N_T = 8.2 \times 10^{-17} W$$
$$N_D = 1.6 \times 10^{-20} W$$
$$N_B = 1.1 \times 10^{-15} W$$
$$N_P = 2.2 \times 10^{-20} W$$

which yields a predicted SNR at the detector output of

$$SNR = 1575 (\sim 32 dB)$$

The model is, therefore, in excellent agreement with the measurements made. It is noted that these measurements were made under background-limited conditions.

Further daytime field-testing of the preprototype optical communications system at ranges up to 1.6 km was extremely successful. The hand-held battery-operated passive terminal provided continuous, high-quality, two-way communications with the helium-neon laser active terminal in a duplex mode. This level of performance was maintained while the unit was jostled about, randomly rotated through angles of ±30 deg, and even in the presence of light fog (visibility of approximately 0.8 km). At ranges of the order of 1.6 km, atmospheric scintillation became noticeable, especially near mid-afternoon, but communications remained highly intelligible. The excellent performance of the preprototype system, most notably the passive terminal, was encouraging indeed. Flexibility in both the physical and electrical design of this unit will permit greatly improved performance through a design optimization effort. In addition to improved performance, considerable reduction in size and weight can be achieved with LSI technology and miniaturized hardware.

The last set of tests conducted under this first experiment concerned using the passive terminal with the incoherent white-light-source active terminal. Field testing was conducted between ground stations and from a small power boat to shore over ranges up to 2.5 km. High-quality, one-way, voice communication was demonstrated even though the passive unit was hand-held and transmission was through water spray on the fast-moving boat. Of perhaps the greatest importance in the demonstration was the discovery that an unpolarized white-light source can be used as an effective alternative to a coherent laser source as a communications medium.

EXPERIMENT 2

SCINTILLATION EFFECTS ON RETROREFLECTED LIGHT BEAMS

OBJECTIVE

The principal objective of this experiment was to determine the effects of atmospheric scintillation on optical communication systems employing the retromodulation concept.

APPROACH

Preliminary tests conducted in the field using the preprototype optical communications systems employing the retromodulation technique indicate that signal fading can, at times, be a serious problem. That is, during communications there will be time intervals for which the signal-to-noise level drops to a point where either serious fading or temporary loss of transmission occurs, particularly for those ranges where the SNR is marginal in the first place. These problems can only be attributed to the degrading atmospheric channel effects, namely amplitude modulation of the return signal as it propagates through the channel due to scintillation arising from atmospheric turbulence.

The basic tests to be performed under this experiment were designed to measure the "scintillation index" associated with optical signal returns from a single modulated retroreflector. Time of day and the nature of the light source used were important items to be considered in the tests. To put things in a little better perspective, consider the following. Suppose we have the means for electrically generating an amplitude-modulated sinusoidal signal, using a waveform synthesizer, of the form (Ref. 4)

$$g(t) = A(1 + M \cos w_o t) \cos w_c t \,. \tag{1}$$

A is a constant of proportionality which incorporates signal strength level, M is the modulation index ($0 \leqslant M \leqslant 1$), w_c is the driver frequency, and w_o the frequency associated with the waveform envelope ($w_o \sim 500$ Hz, $w_c \sim 20$ kHz). Let us suppose the modulation index M is unknown and that we wish to devise an experimental technique to measure M, given g(t) as the input. One technique for measuring M goes as follows. First the signal g(t) is passed through an electrical circuit which rectifies and low-pass-filters g(t). The output of this circuit is the modulation envelope, namely,

$$f(t) = B(1 + M \cos w_o t) \,. \tag{2}$$

B is simply a new constant of proportionality. The mean value of f(t) is determined by

$$\mu = \lim_{T \to \infty} (1/T) \int_0^T f(t)\, dt \tag{3}$$

which when evaluated gives $\mu = B$. The mean square value of f(t) is determined by

$$\psi^2 = \lim_{T\to\infty} (1/T) \int_0^T f^2(t)\, dt \tag{4}$$

which yields

$$\psi^2 = B^2(1 + M^2/2). \tag{5}$$

The variance is given by

$$\sigma^2 = \psi^2 - \mu^2 \tag{6}$$

which yields

$$\sigma^2 = B^2M^2/2. \tag{7}$$

σ, the standard deviation, is thus given by

$$\sigma = BM/\sqrt{2}. \tag{8}$$

Dividing σ by μ gives the important result

$$\sigma/\mu = M/\sqrt{2}. \tag{9}$$

Thus measuring the standard deviation σ and the mean μ of the envelope and dividing these two quantities according to Eq. (9) gives a means for directly measuring the quantity M. For the case of a randomly varying signal envelope associated with atmospheric amplitude modulation, the ratio σ/μ is referred to as the scintillation index. Of course, in any practical computation of σ/μ the integration time interval would be finite; thus one should not expect the scintillation index to remain stationary, as would be the case for a purely deterministic signal as given by Eq. (2). Measuring the scintillation index associated with atmospheric scintillation, using the technique just described, gives the means for comparing signal returns for various times of the day as well as for different light sources employed in the active terminal. An important point to note is that the ratio σ/μ eliminates the constant B, which contains signal strength levels that may be slowly varying in time. Shown in Fig. 7 are some representative plots of various periodic deterministic envelope waveforms over one period. Also included are the computed ratios of σ/μ for each of these waveforms. It should be obvious from Fig. 7 that higher values of σ/μ would result in longer and deeper signal fading. The ideal case would correspond to a σ/μ ratio of zero, that is, no amplitude modulation, hence no signal fading.

The actual experimental setup for measuring the scintillation index is depicted in the schematic diagram of Fig. 8. A single modulated retroreflector and both the laser and white-light active terminals described in experiment 1 were employed in this experiment. The actual communications link used was between buildings 4 and 593 at NOSC. The distance between these buildings is 1.6 km. The modulated retroreflector used in this experiment was different from the one used in experiment 1. Lithium niobate was again used in combination with a solid-glass corner-cube retroreflector whose rear reflecting surfaces were silver coated. The design of the housing and driver first used for this modulating retroreflector was modified for this experiment. No receiver was required in the passive terminal. Figure 9 shows the passive

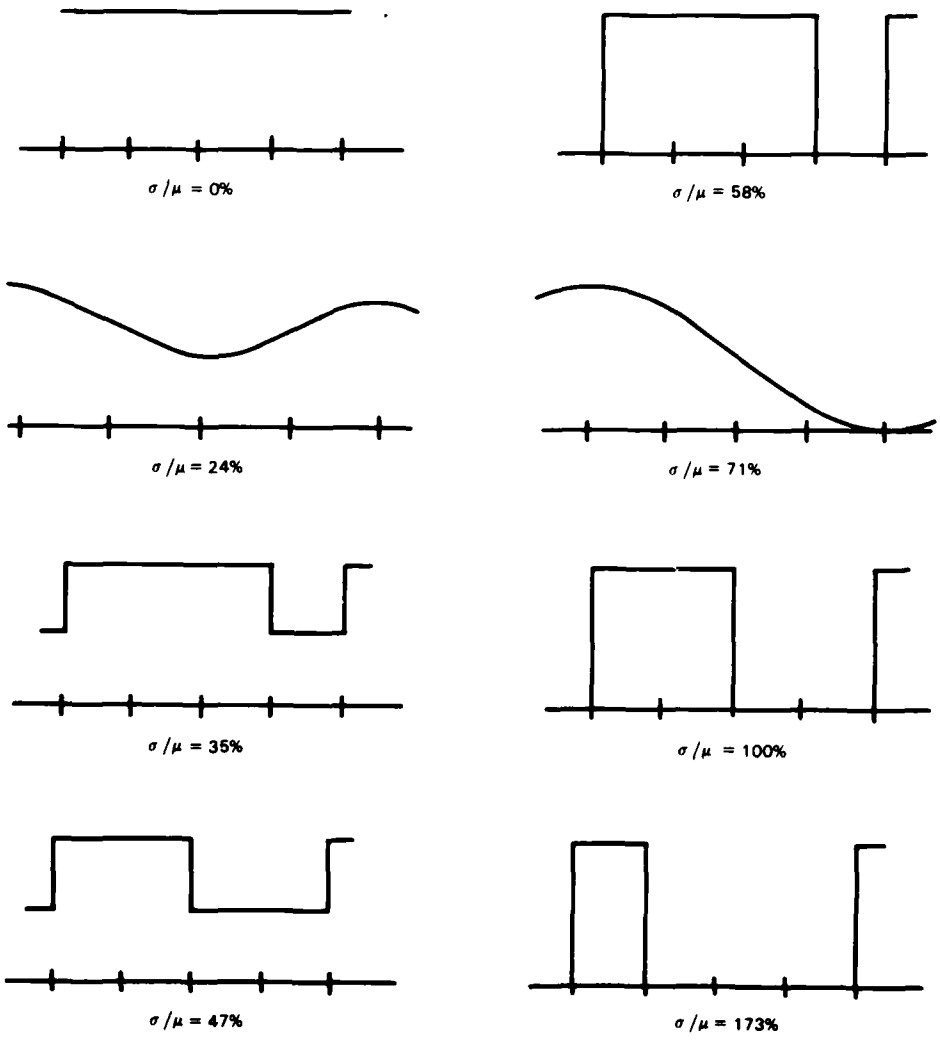

Figure 7. Deterministic waveform envelopes and associated σ/μ ratio.

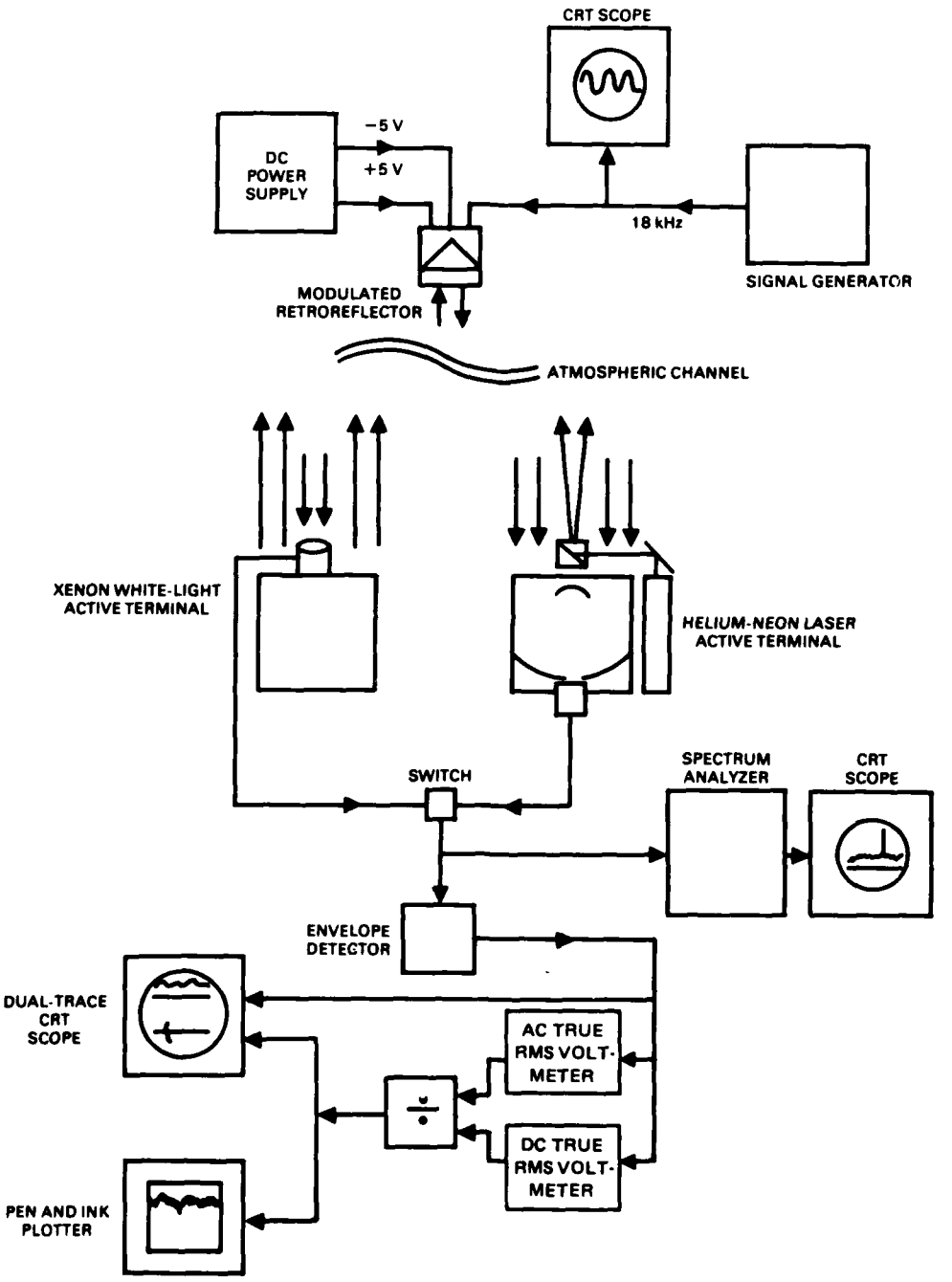

Figure 8. Experimental setup for experiment 2.

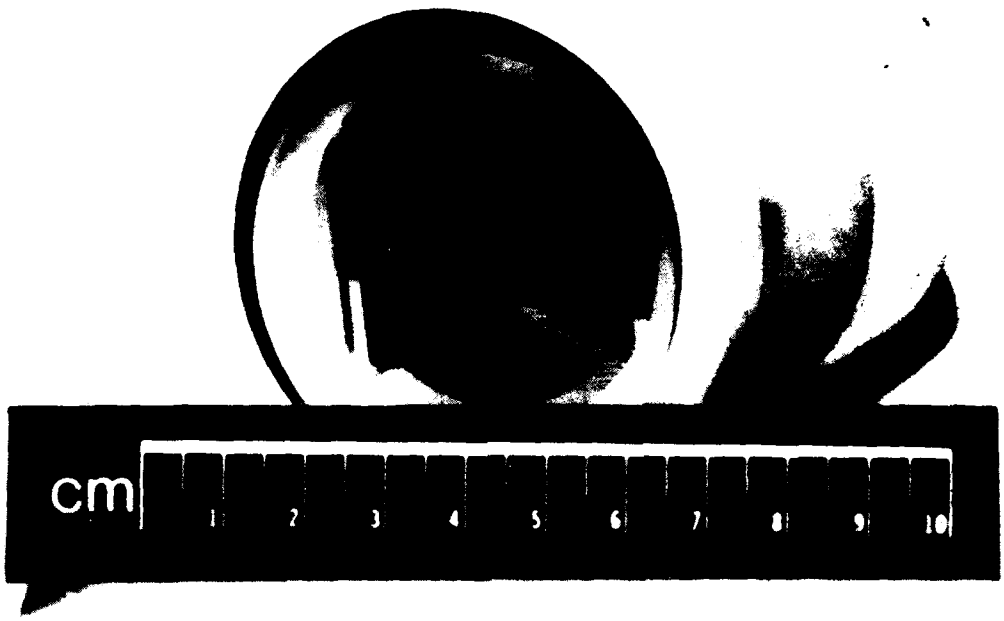

Figure 9. Lithium niobate passive unit used in experiment 2.

unit used in this experiment, and Fig. 10 the disassembled passive unit, depicting its simplicity. Figure 11 is a schematic diagram of the driver electronics for this unit. The modulated retro-reflector was driven by a Wavetek signal generator, which supplies a continuous 18-kHz carrier, 1-V peak-to-peak signal. The driver electronics internal to the modulator assembly convert this signal to a 600-V peak-to-peak ac signal across the terminals of the crystal modulator. A dc power supply which delivers 10 V to the modulator is used for biasing the crystal modulator to approximately 400 V via internal modulator electronics. Hence any incident light beam impinging upon the modulated retroflector would be returned to the light source with the 18-kHz-carrier information impressed upon it.

A capability of switching back and forth between the helium-neon laser and white-light source active terminals was set up for experimental comparative purposes. The light beam

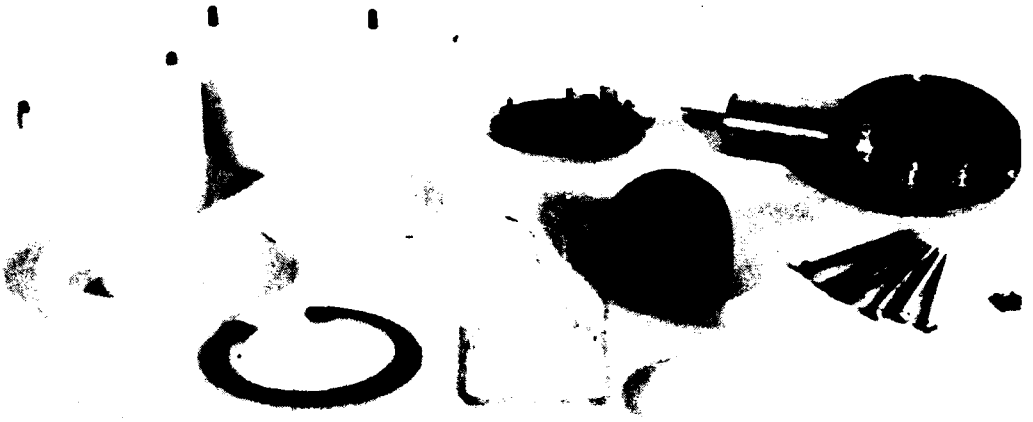

Figure 10. Lithium niobate passive unit disassembled.

received at the detector, after having made a double pass through the atmosphere was monitored with an electronic spectrum analyzer, by means of which signal-to-noise ratios could be readily measured. This same signal was also sent through an envelope detector circuit, previously described. The resulting envelope signal (real positive) was displayed on a cathode ray tube (CRT) as well. This envelope signal was also sent through two rms voltmeters one operating in the ac rms mode, the other in the dc mode. The signals from both voltmeters were sent into an analog divider, where the ratio of the ac rms to dc voltage was computed and displayed both on a CRT and recorded as a function of time with a pen and ink plotter. Both the true-rms voltmeters were set at 10-s response time settings. Thus the setup depicted in Fig. 8 allowed us to measure the scintillation index associated with the atmospheric channel without concern for light source levels, absorption within the atmospheric channel, or other multiplicative constants arising from within the electronics.

RESULTS

Measurements were made between 19 and 22 June 1978 between 8 am and 9 pm. During this time of the year the sun rises in San Diego at about 5:40 am and sets at 8:00 pm. For the 4 days in which measurements were made, the days were clear, with a visibility of about 15 km. At the beginning of each day the system was calibrated using an injected laboratory test signal from a Wavetek signal generator. Specifically, an 18-kHz carrier with a 300-Hz square or sine wave envelope (100% modulation index) was used.

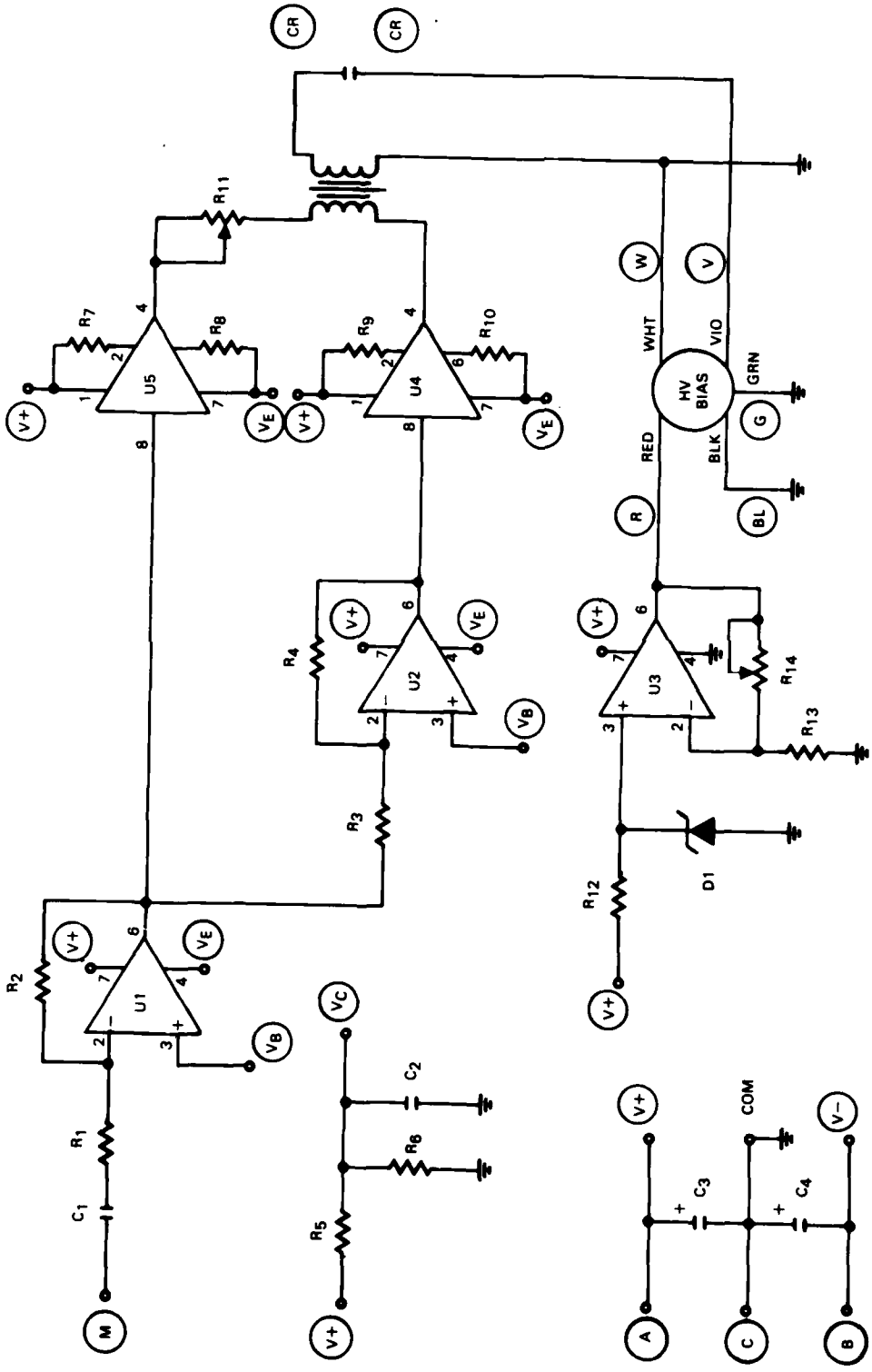

Figure 11. Schematic circuit diagram of driver electronics used in lithium niobate passive unit.

Figure 12 typifies the data recorded during these 4 days. Scintillation index is plotted along the ordinate and time along the abscissa. One inch along the horizontal scale corresponds to 100 s of data. Shown in this figure are five windows of data, each window 200 s long. These windows correspond to data being taken at 2, 4, 6, 7, and 8 pm, respectively, using the helium-neon laser light active terminal on 19 June 1978. Figure 13 is similar to Fig. 12, except that the white-light-source active terminal was employed. Inserting an infrared filter in front of the xenon short-arc lamp in the white-light-source active terminal allowed us to take data in the near-infrared portion of the spectrum. Figure 14 is typical of the data observed for the near-infrared radiation. On 22 June 1978 data were taken every half-hour from 8 am to 9 pm using the three spectral sources. A summary of the data is shown in Fig. 15. The data may be interpreted as follows. At 11 am, for example, the scintillation index for the helium-neon laser light source was about 137% with fluctuations of ±20%. For the white-light source, the scintillation index was measured at 47% with fluctuations of ±5%. The scintillation index for the near-infrared mode was measured as 35% with ±5% fluctuations. It is noted that in the early hours of the day and late in the day the effects of atmospheric scintillation are considerably less than at midday. Also, the effects of atmospheric scintillation are greatly reduced when the white-light or near-infrared light sources are employed. It is believed the principal reason for this is that the laser beam diameter at the active terminal is about 1 mm, whereas the white-light and infrared beam diameters at the active terminal are approximately 350 mm. The beneficial effects of aperture averaging are definitely on the side of a large-diameter light beam.

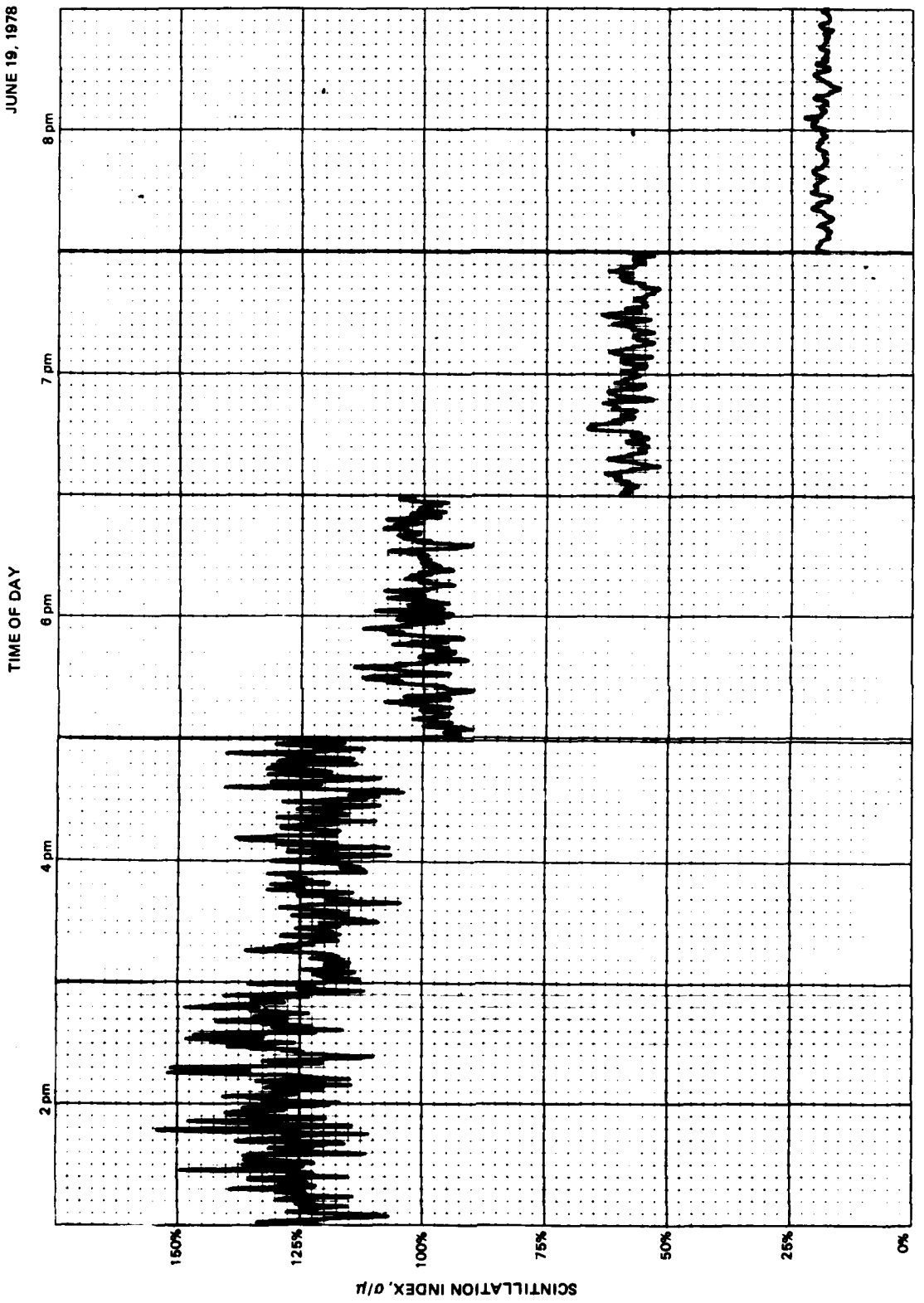

Figure 12. Scintillation index for helium-neon laser light source.

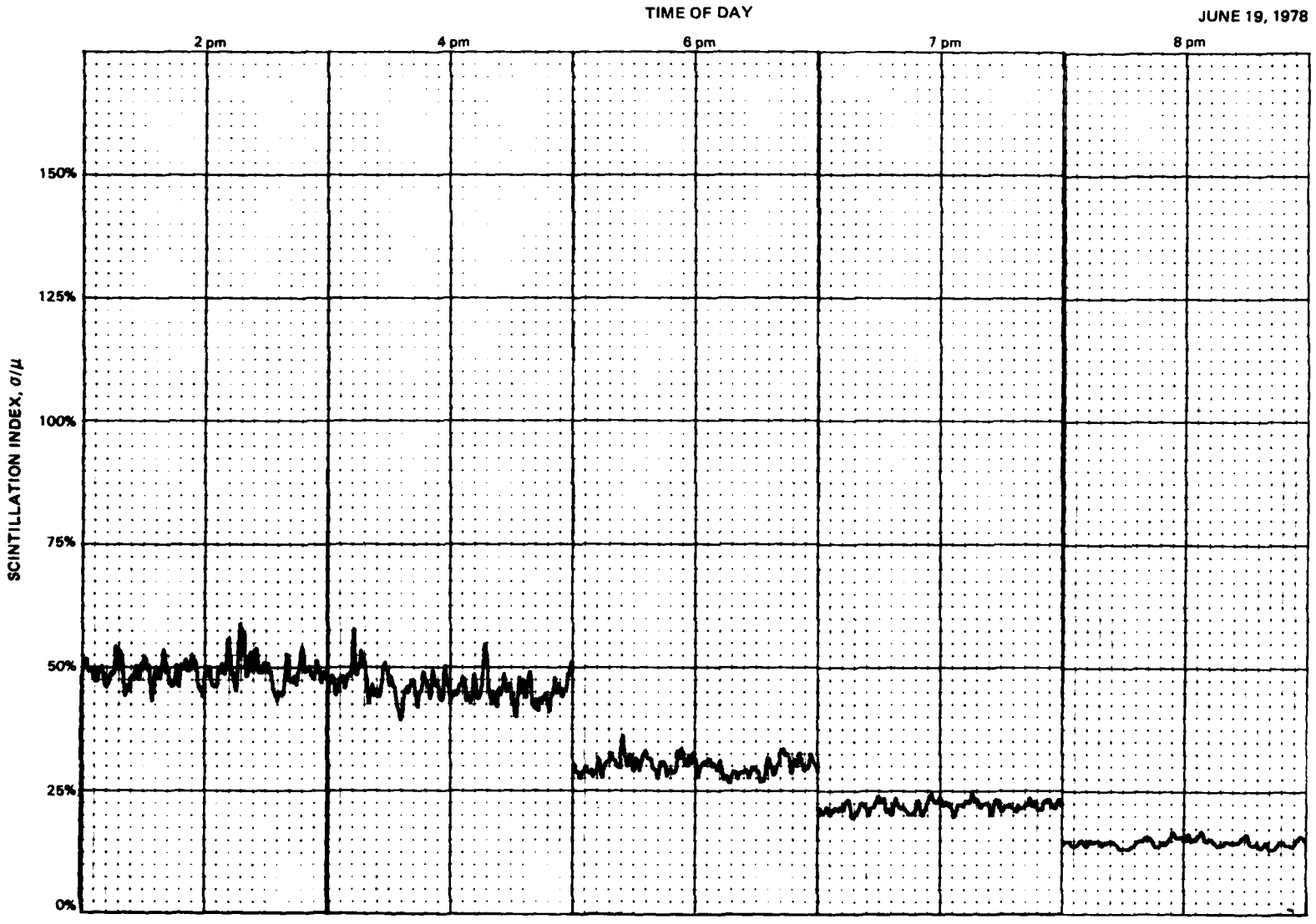

Figure 13. Scintillation index for a white-light source.

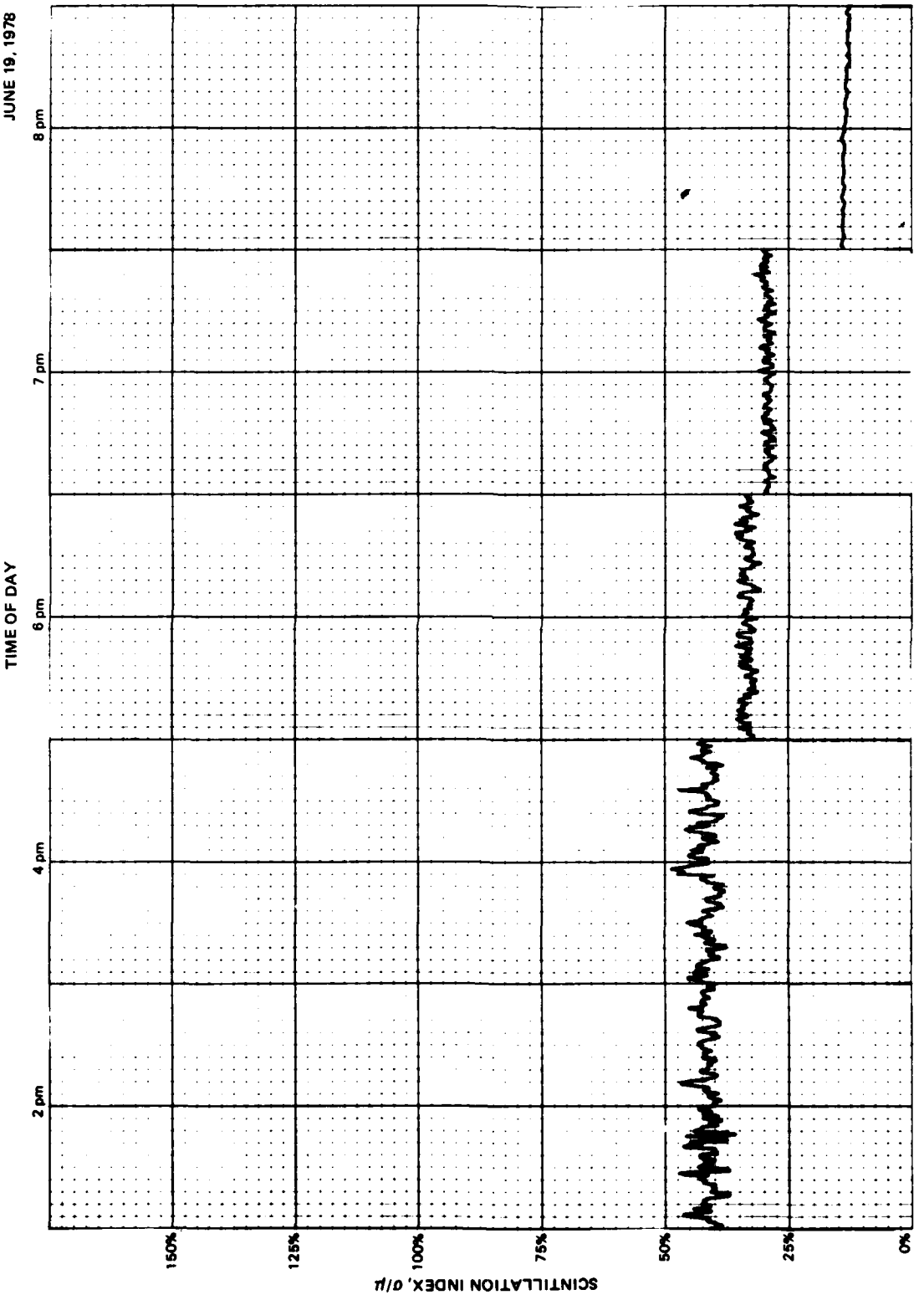

Figure 14. Scintillation index for near-infrared light source.

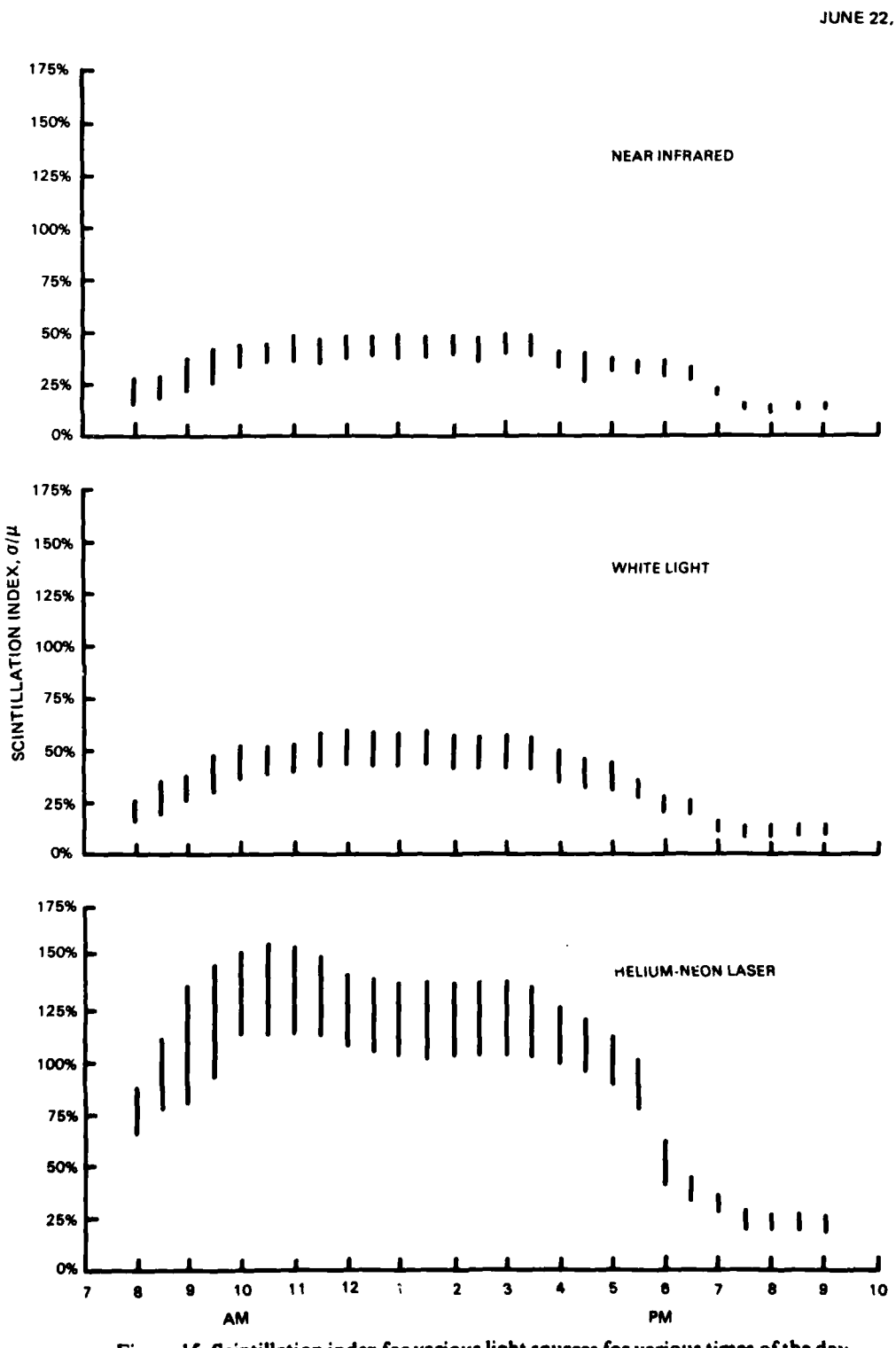

Figure 15. Scintillation index for various light sources for various times of the day.

EXPERIMENT 3

APERTURE AVERAGING AS A MEANS OF REDUCING SCINTILLATION EFFECTS

OBJECTIVE

The principal objective of this experiment was to determine to what extent atmospheric scintillation may be reduced by applying aperture-averaging techniques.

APPROACH

Experiment 2 was primarily concerned with determining the scintillation index associated with atmospheric turbulence over a 1.6-km test link, employing a single modulated retroreflector in the passive terminal and both laser and white light from the active terminal. It has been proposed that if two or more modulated retroreflectors were employed in the passive terminal, the degrading effects of atmospheric turbulence might be reduced. This experiment was designed to test this hypothesis. The idea to be tested goes as follows. If two modulated retroreflectors are spatially separated by a distance greater than the "decorrelation" distance ($\sim$6 cm) of the turbulence scale size, then the signal return from each modulator may be added, giving rise to an overall signal whose fading is reduced. This technique is referred to as "aperture averaging." The decorrelation distance is defined as that distance between the two retroreflectors for which the degrading atmospheric channel effects on each of the returned optical beams are essentially uncorrelated.

The basic tests to be performed under this experiment were designed to measure the scintillation index associated with optical returns from two or more retroreflectors modulated in parallel over the 1.6-km test link at NOSC using, again, both laser and white light. The experimental setup (Fig. 16) used in this experiment is basically the same as that used in experiment 2, the principal difference being that two or more modulated retroreflectors are employed. Figure 17 shows ten lithium niobate retromodulators fabricated at NOSC for this test as well as future tests associated with the modulated retroreflection concept. Each of the units shown in this figure is identical to the one employed in experiment 2.

RESULTS

Measurements were made between 29 June and 3 July 1978 during the daylight hours. During this period the days were clear, with visibility of about 15 km. The same calibration procedures used in experiment 2 were also employed in this experiment. In addition, the SNRs at the active terminal detectors were measured for each of the retromodulators being driven in parallel. Adjustments were made such that the SNR associated with each modulator in the array was the same. Typically, the SNR for a single retromodulator for the 1.6-km range, using the helium-neon laser terminal, was 35 dB. For the incoherent xenon white-light terminal the SNR was typically 45 dB.

Figures 18, 19, and 20 are very typical of scintillation index data taken using the helium-neon laser terminal at various times of the day. Scintillation index is plotted along the ordinate and time along the abscissa. One inch along the horizontal scale corresponds to 100 s of data. In each of these three figures there are ten windows of data, each 100 s in duration, taken at various times of the day. Figure 18 corresponds to the case of a single retromodulator. Figures 19 and 20 correspond to the case of two modulated retroreflectors driven in parallel

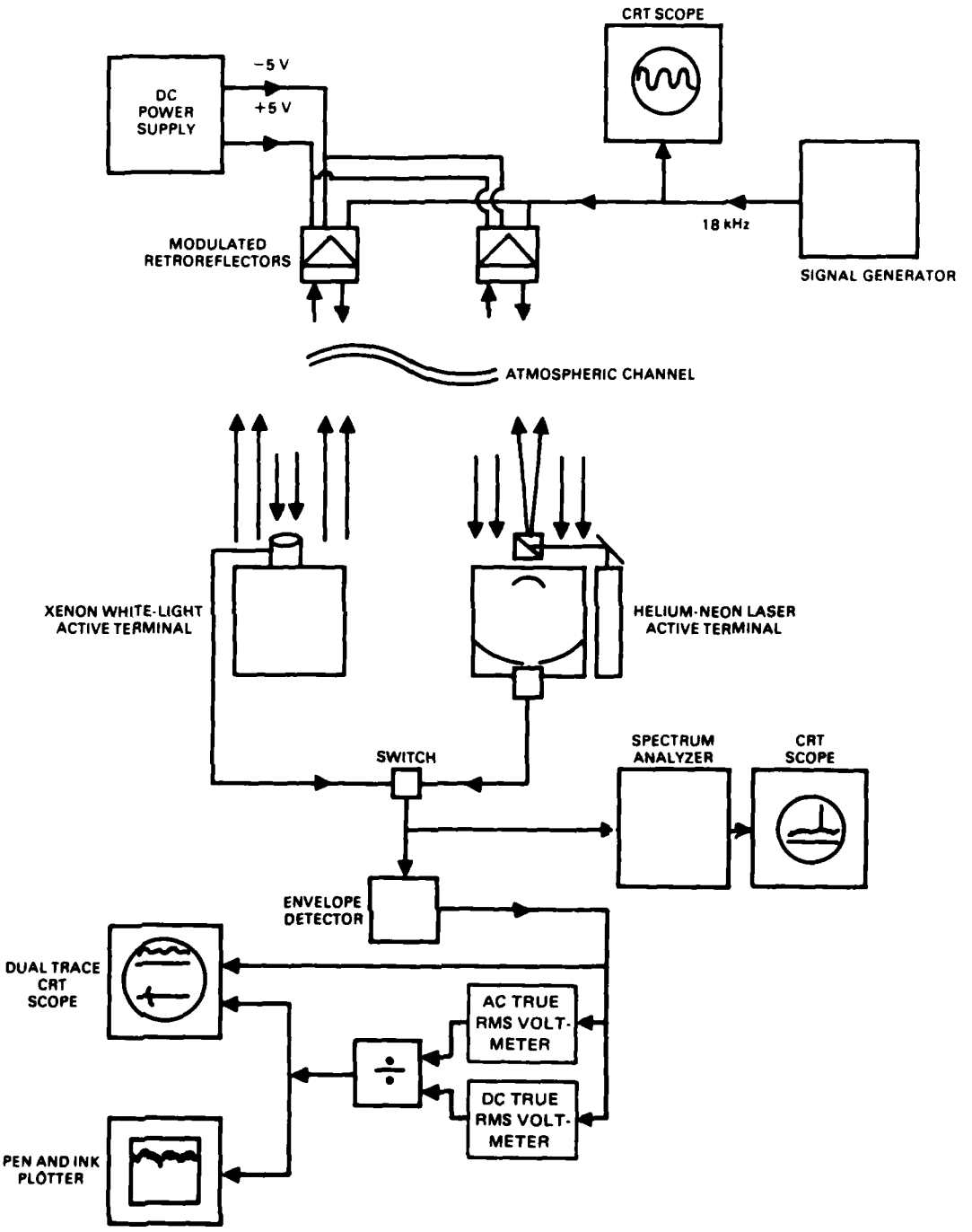

Figure 16. Experimental setup for experiment 3.

Figure 17. Array of ten lithium niobate retromodulators.

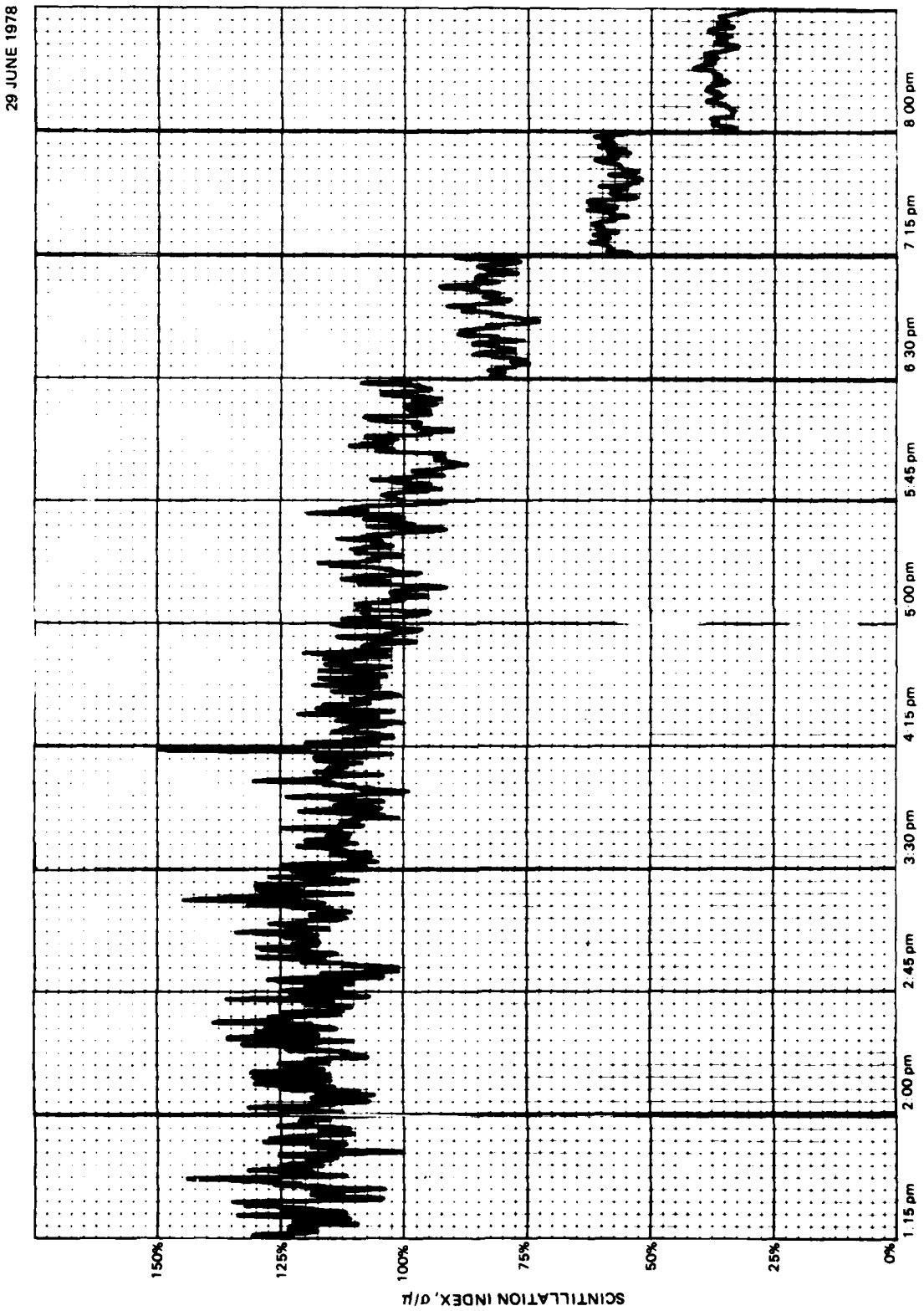

Figure 18. Scintillation index for a single modulated retroreflector using laser light.

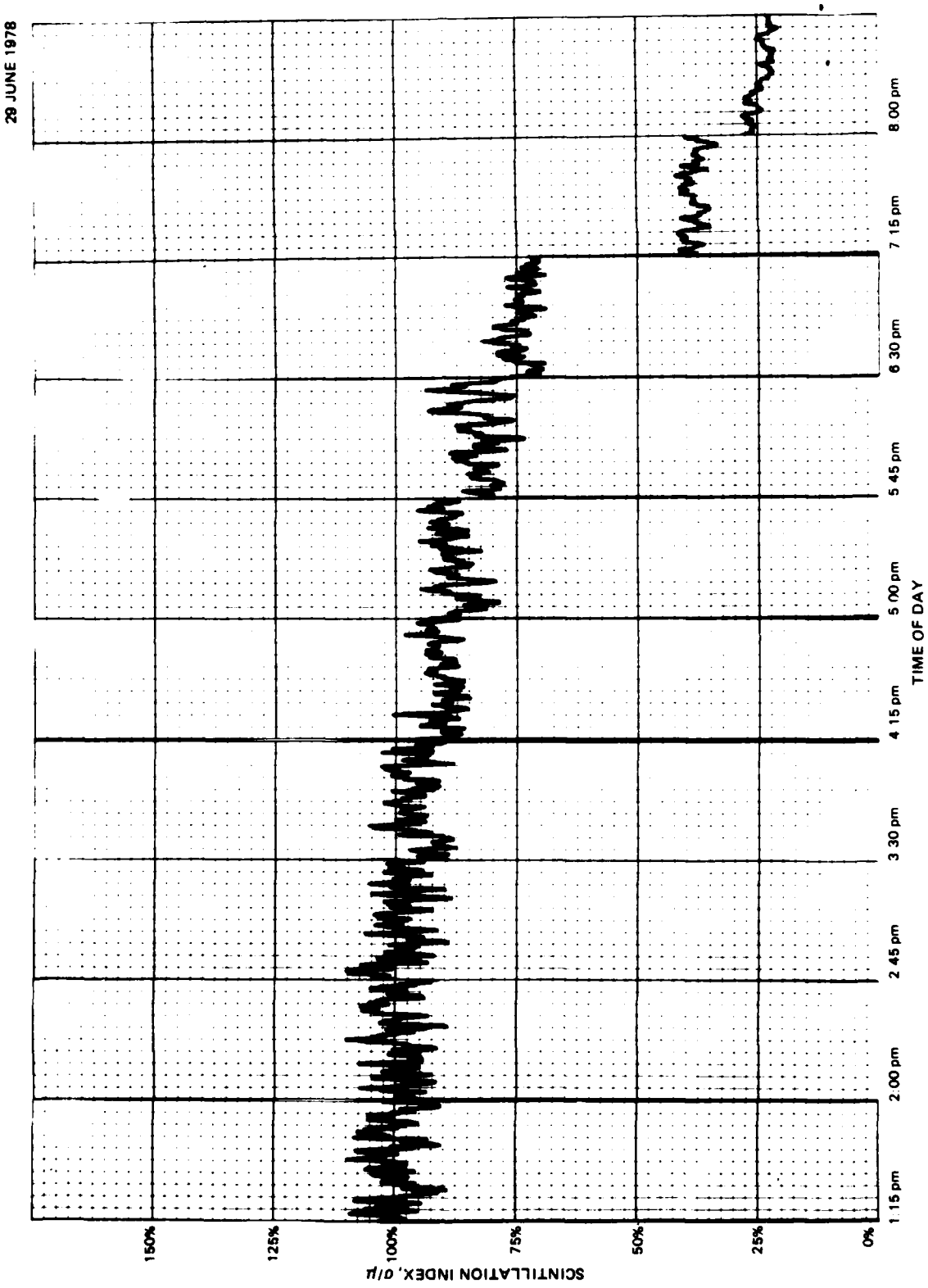

Figure 19. Scintillation index for two separated (8 cm) retromodulators using laser light.

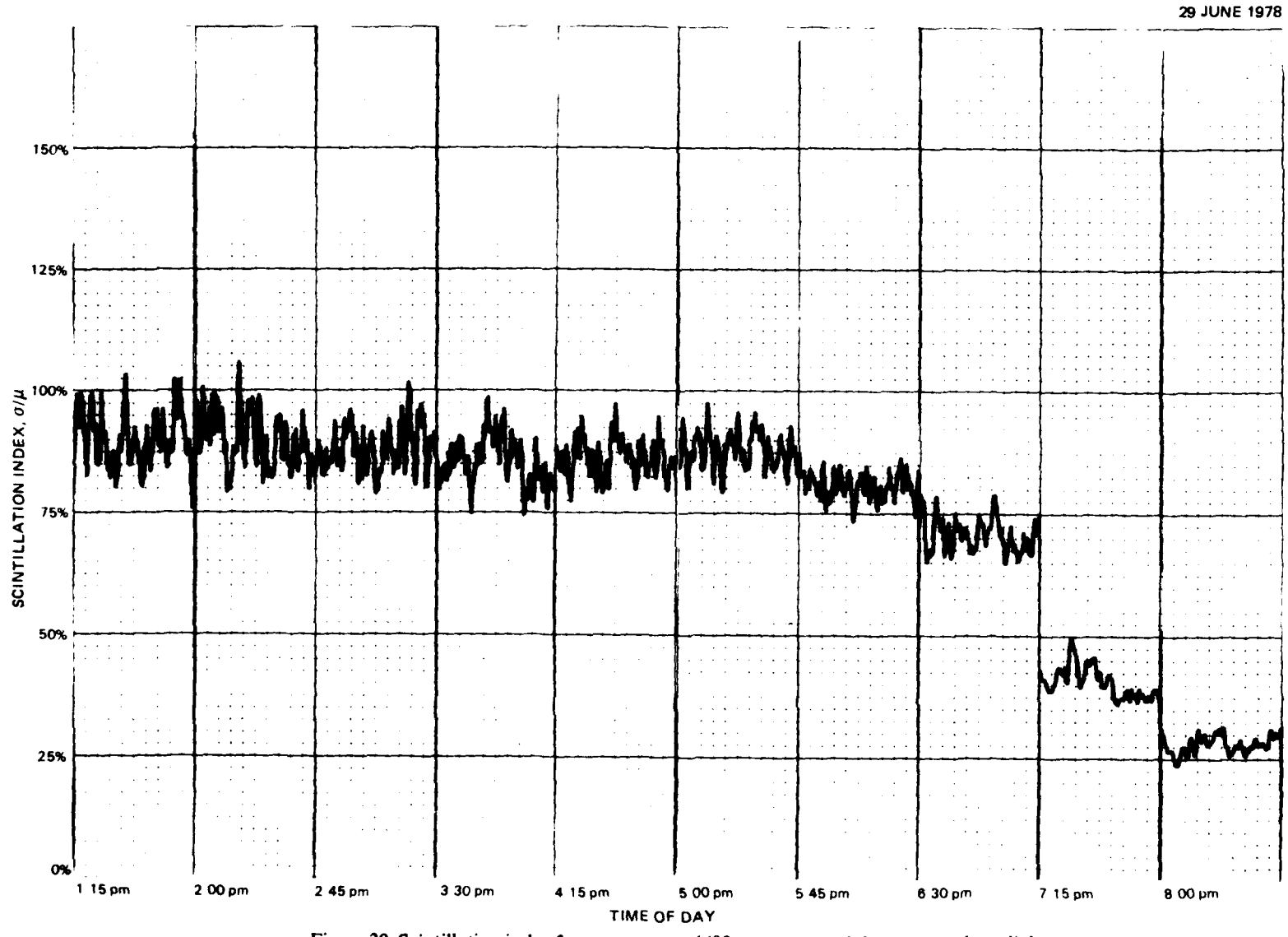

Figure 20. Scintillation index for two separated (80 cm) retromodulators using laser light.

whose center-to-center spacings are 8 and 80 cm, respectively. Comparing these figures, we find that, on the average, the scintillation index associated with the two reflectors separated 8 cm is 0.80 times the scintillation index associated with a single reflector. This represents an improvement of 20% in reducing the value of the scintillation index. Similarly, the scintillation index associated with two reflectors separated 80 cm is 0.77 times the scintillation index associated with a single reflector. This corresponds to an improvement of 23%.

Figures 21, 22, and 23 typify scintillation index data taken using the white-light source at various times of the day. As before, 1 in. on the horizontal axis corresponds to 100 s of data. In each of these figures there are five windows of data. Figure 21 represents the single-retroreflector case. Figures 22 and 23 represent the two-reflector case for 8- and 80-cm separations, respectively. Comparing these figures, we find improvements of 4% and 9% for separations of 8 and 80 cm.

Figure 24 shows results of scintillation index values for a passive terminal containing anywhere from one to six modulated retroflectors in a linear array with 8-cm spacing between adjacent retroreflectors using the helium-neon laser light. It is quite obvious from this figure that the scintillation index decreases in value with increasing number of reflectors. Empirically, the scintillation index for the case of n reflectors ($1 \leqslant n \leqslant 6$) is approximately $n^{-1/2}$ times the scintillation index for a single retroreflector for 8-cm separation using the 0.633-μm light. This corresponds to an improvement of $1-n^{-1/2}$. The curve in Fig. 25 represents the improvement predicted using the aforementioned empirically derived formula.

Based on results obtained for both experiments 2 and 3, it is apparent that aperture averaging does indeed reduce the degrading effects of atmospheric scintillation, hence signal fading. One can either increase the diameter of the outgoing light beam at the active terminal or employ several modulated retroreflectors in the passive terminal or both. Increasing the separation between retroreflectors has much less effect on reducing the scintillation index when compared to the gains made by increasing the area (number) of retromodulators.

EXPERIMENT 4

AIR-WATER INTERFACE EFFECTS ON RETROREFLECTED OPTICAL LIGHT BEAMS

OBJECTIVE

The principal objective of this experiment was to determine the effects of a randomly varying air-water interface on optical communication systems employing the retromodulation concept for an air-to-underwater communications scenario.

APPROACH

Preliminary tests conducted in the laboratory (Ref. 1) indicate that optical communications systems employing the retromodulation technique could be utilized for air-to-underwater communications. That is, if a passive optical communications terminal employing a modulated retroreflector were used underwater and an active terminal employing a light source were used above the surface, then, in principle, information transfer is possible between the two terminals. In Appendix B the system equations for the air-to-underwater scenario are presented for the case of a perfectly flat air-water interface. Basically, these system equations are the same as those used for predicting system performance for the

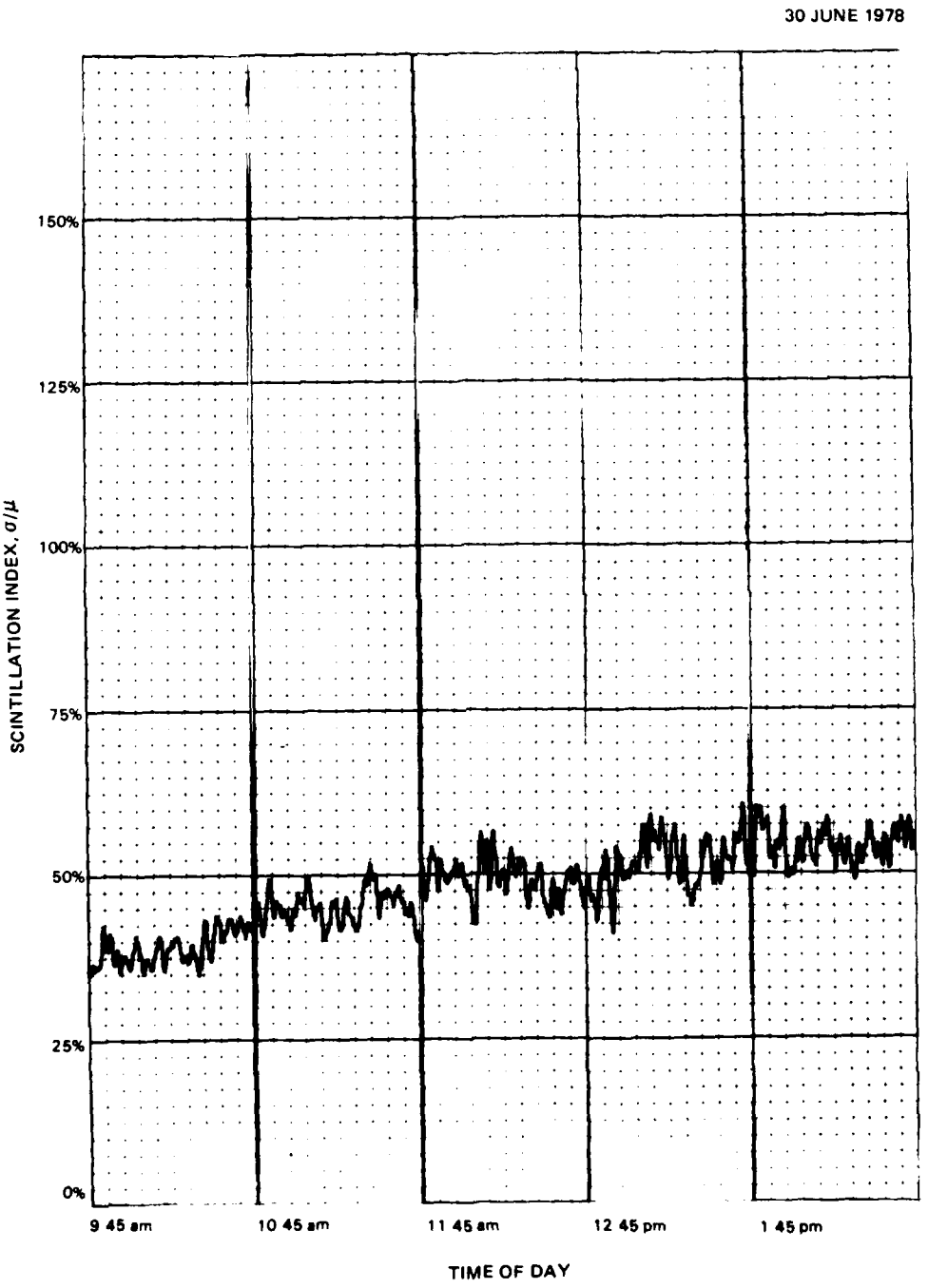

Figure 21. Scintillation index for a single modulated retroreflector using white light.

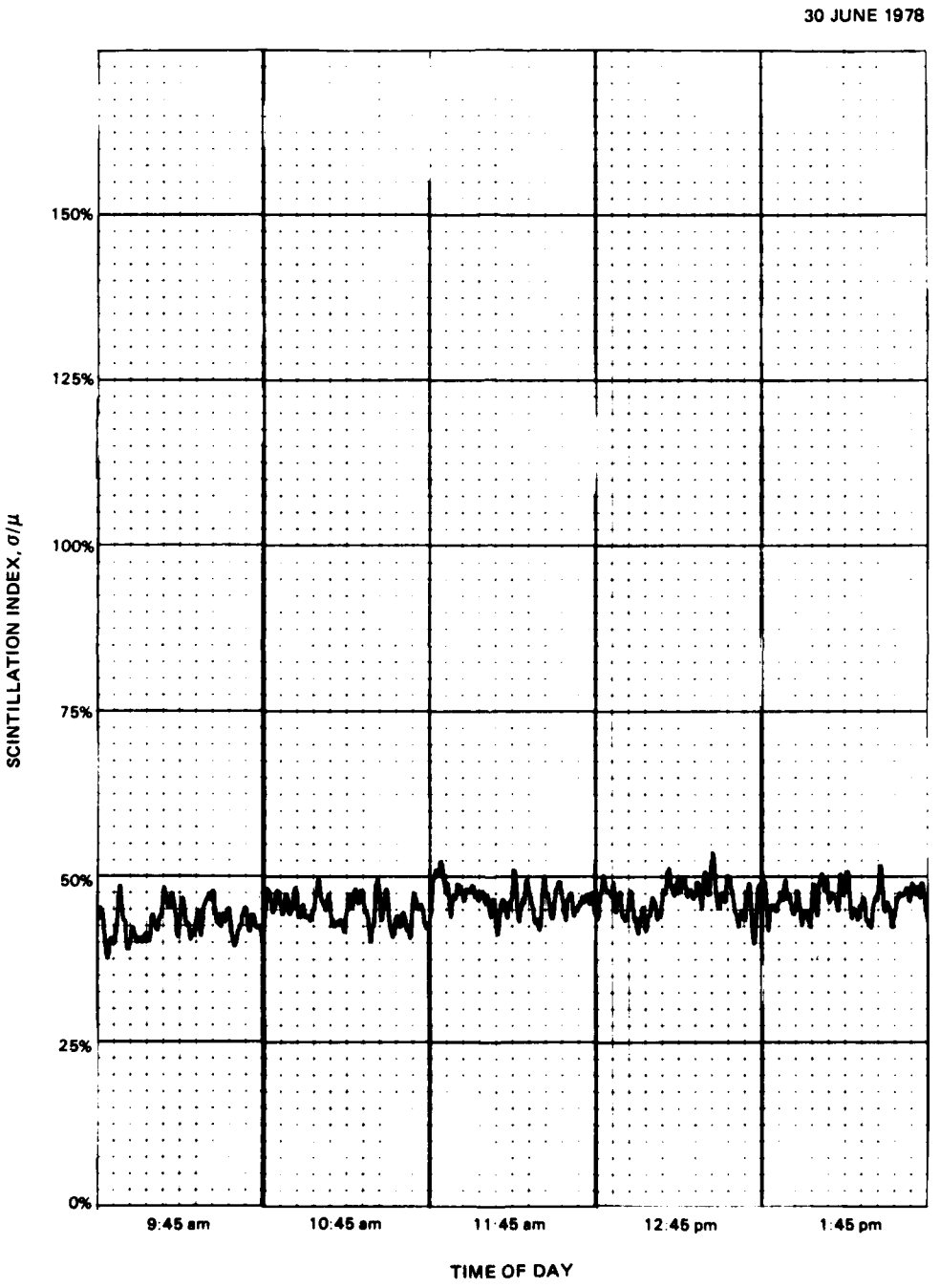

Figure 22. Scintillation index for two separated (8 cm) retromodulators using white light.

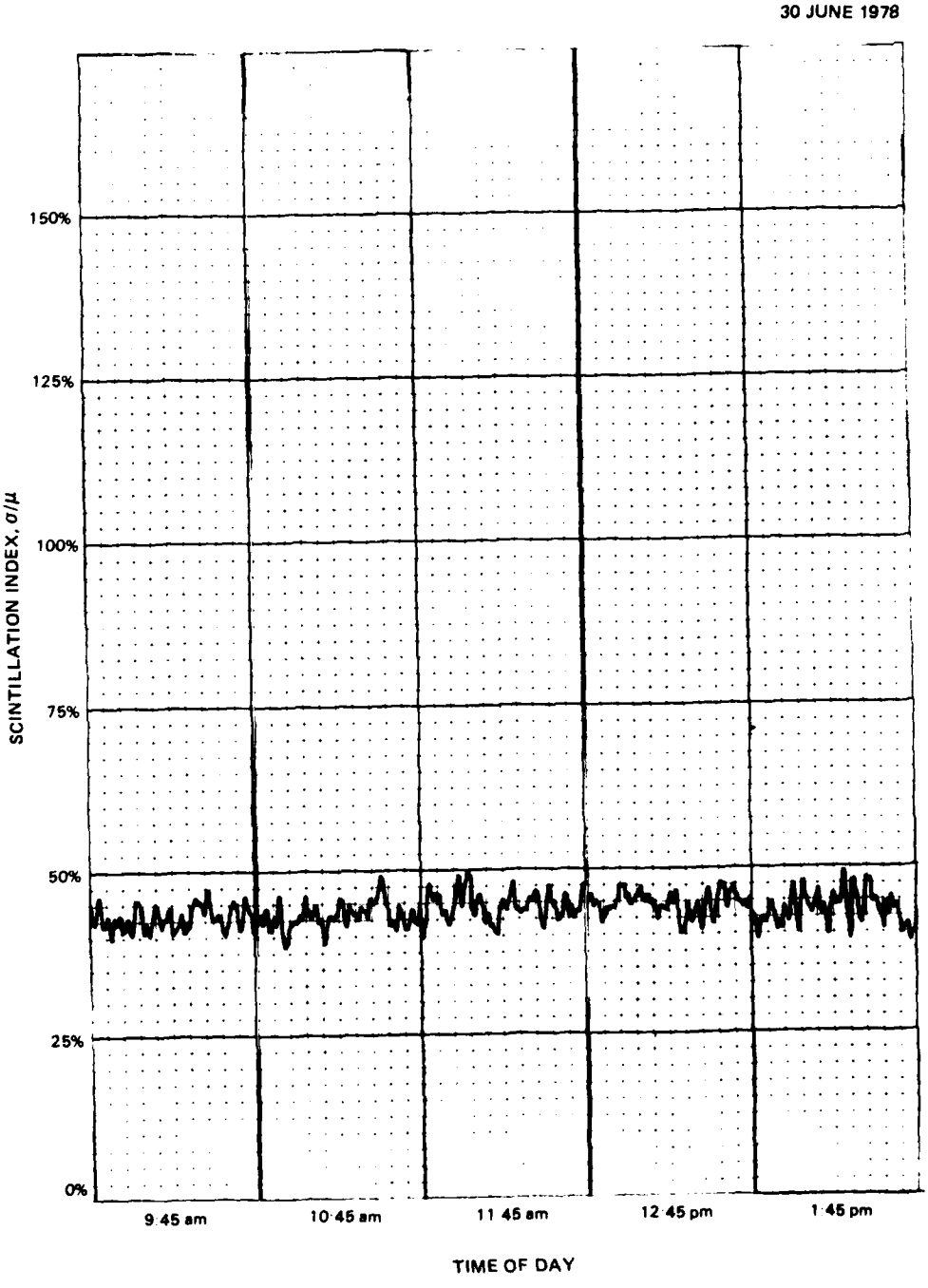

Figure 23. Scintillation index for two separated (80 cm) retromodulators using white light.

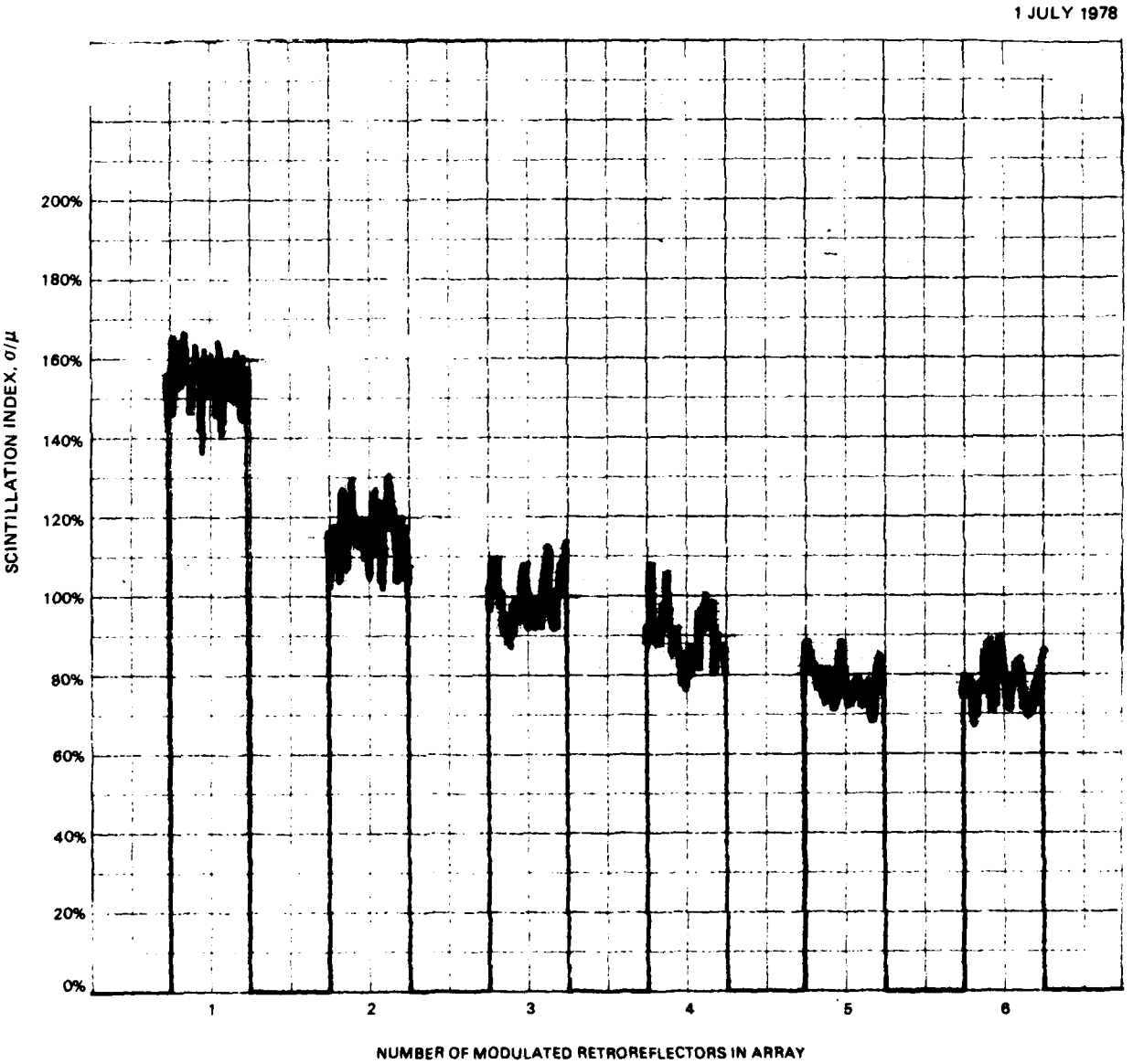

Figure 24. Scintillation index versus number of retromodulators for laser light.

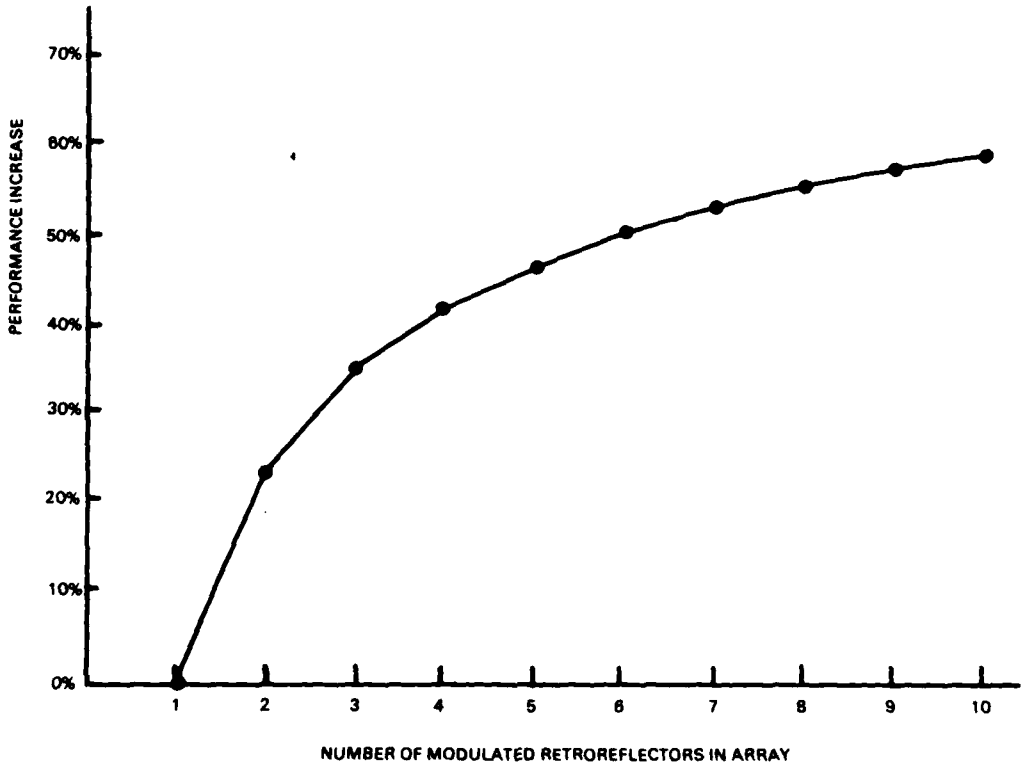

Figure 25. Performance increase in scintillation index reduction as a function of the number of modulated retroreflectors comprising the array for 8-cm separation using 0.633-μm light.

atmospheric line-of-sight communications scenario (Appendix A), except that additional loss terms due to underwater absorption and scattering as well as air-water interface are included. For the case of a perfectly flat air-water interface, the only losses at the interface arise from what are termed "Fresnel reflection losses," which amount to 2% for normal incidence for each pass through the interface. Of course these losses increase with increasing angle of incidence. However, laboratory tests and experiments show that the losses incurred at a randomly varying air-water interface can be rather significant due to additional beam-spreading effects introduced by refraction at the randomly varying wave surfaces. In Appendix F a simplified model is derived for predicting the additional losses which might be expected due to a randomly varying air-water interface. As is evident from the results presented there, the additional losses may amount to many tens of decibels.

In addition, the preliminary tests performed in the laboratory (Ref. 1) employed both $LiNbO_3$, and PLZT as the large-area modulating elements. Both were modulated using frequency modulation techniques for comparative purposes. Each optical modulator works on entirely different principles. The $LiNbO_3$, again, behaves like a tunable phase diffraction grating modulator (see Appendix C), whereas the PLZT behaves more like a conventional Kerr cell, requiring polarizers for its operation (see Appendix D). For the case of the air-to-underwater laboratory experiments, it was found that communication was impossible

using the $LiNbO_3$ in the phase grating mode, whereas good-quality voice communication was possible using the PLZT. A tenable explanation for why $LiNbO_3$ gave poor results is that when used in a phase grating mode, the refraction effects at the randomly varying interface were so degrading that the various diffraction orders exiting the modulated retroreflector were actually mixed spatially, thus distorting the communications signal of interest beyond recognition, regardless of the SNR. However, if the signal-to-noise ratio is large enough to compensate for beam-spreading losses at the interface, then high-quality voice transmission can be obtained, using PLZT as the modulator element, without any distortion effects. However, as indicated, the beam-spreading losses introduced at a randomly varying air-water interface can be considerable and thus greatly affect what operating ranges one can achieve in practice.

The tests conducted under experiment 4 were designed to experimentally measure the additional losses incurred at the air-water interface due to random wave activity in a field environment. The actual experimental setup employed is depicted in Fig. 26. A variety of retroreflectors and retroreflecting materials used in combination with a 10-cm-diameter PLZT modulator were employed in the passive terminal located underwater. The incoherent-white-light active terminal employed in the previous experiments was exclusively used in this experiment. The actual communications link established at NOSC was between the hut atop Pedro Tower adjacent to building A-45 and the TRANSDEC sonar pool testing facilities (Fig. 27). Pedro Tower is approximately 33 m high and the slant range between the active and passive terminals was approximately 120 m. The passive terminal was packaged in a watertight canister whose clear entrance window has a diameter of 15 cm. The driver electronics used for the PLZT are identical to those described in Appendix D and were located inside building 419 at TRANSDEC. A coaxial cable connected to the driver with the passive terminal modulator. A 60- by 90-cm flat mirror was used to divert light from the active terminal to the passive terminal to obtain near-normal angles of incidence. A Wavetek signal generator was used to deliver an 18-kHz test signal to the modulated retroreflector. By means of an electronic spectrum analyzer, the SNR associated with the retroreturn was measured back at the active terminal's optical receiver for both flat and agitated air-water-interface conditions.

RESULTS

Tests were conducted during the daylight hours in June of 1979. Calibration tests were made daily before 8 am at both the TRANSDEC pool and Pedro Tower facilities. The reason for this is that before 8 am during the month of June, there is little or no breeze from the Pacific Ocean to agitate the air-water-interface. Hence, for all practical purposes the interface is flat before 8 am. The underwater canister containing the passive terminal was lowered to a depth such that its entrance window was approximately 8 cm below the air water interface. This was to insure that the measurements dealt principally with losses at the air-water interface. The SNR associated with the 18-kHz retroreturn for the 10-cm PLZT ceramic with various retroreflective materials was repeatedly measured to be +42 dB for an array of silver-coated 2.5-cm-diameter glass corner cubes, +21 dB for a prismatic array of plastic, aluminum-coated corner cubes of 1 mm diameter, and approximately +4 dB for 3M-Scotchlight glass bead retroreflecting material. These measurements were obtained when the active terminal's xenon short-arc lamp was set in the narrowbeam mode, which corresponds to a beam divergence of 2 deg full-angle. The half-angles of the beam intensity

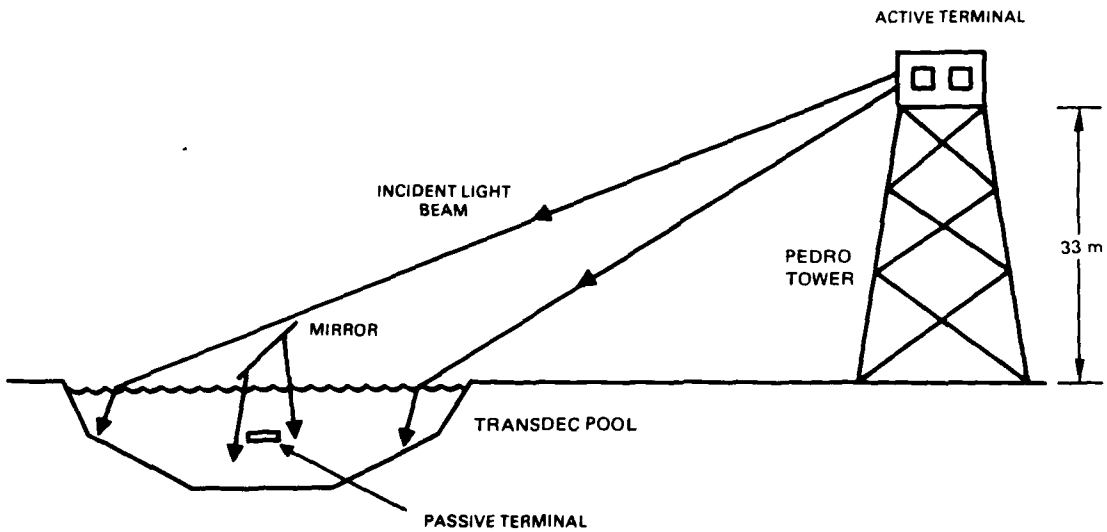

Figure 26. Setup for air-to-underwater test link.

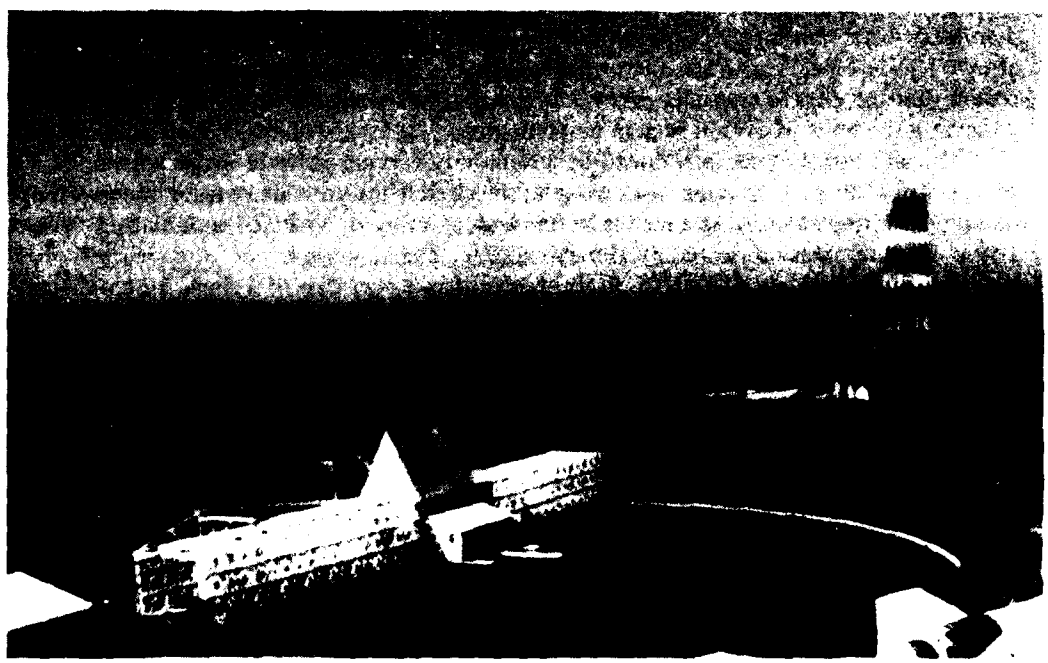

Figure 27. Air-to-underwater optical test link at the Pedro Tower/TRANSDEC pool facilities.

profiles for the retroreflected returns for the various PLZT/retroreflector combinations were measured earlier in the laboratory. The PLZT ceramic modulator employed was not of high optical quality when compared with that of the $LiNbO_3$ crystal modulators. The full-width half-maximum angles measured for the combinations of PLZT with the array of solid glass corner cubes, prismatic array, and 3M-Scotchlight for 0.633-μm illumination were approximately 4, 10, and 24 deg, respectively.

During the afternoon hours at the TRANSDEC pool facilities, the prevailing winds from the Pacific Ocean are enough to agitate the air-water interface, producing at the test location capillary waves with approximately one-dimensional wave structure. A variety of wave amplitude-to-period ratios were measured. In addition, the signal-to-noise ratios associated with the retroreturns under these conditions were measured. For the case of the 3M-Scotchlight material, the signal was buried in the background noise when the surface was agitated. Shown in Figure 28 is a summary of data obtained for the corner-cube array and prismatic retroreflecting materials. For purposes of comparison, the one-dimensional theoretical loss curves generated in Appendix F are superimposed. During the measurement process, the SNR fluctuates in time about a mean. This accounts for the error bars in the plot. It is noted the experimental data are in fairly good agreement with the theoretical predictions.

It is evident from Fig. 28 that the losses incurred at an agitated air-water interface are higher for the array of 2.5-cm-diameter glass corner cubes than for the plastic prismatic array of 1-mm-diameter corner cubes. The reason for this is that the retroreflected rays from the prismatic array travel more closely along the paths from which they came. This is a result of the fact that the rays reflected within (i.e., internally) the smaller 1-mm prismatic array cubes are spatially translated laterally much less than in the larger 2.5-cm corner cubes. Hence, the prismatic array more closely approximates a true retroreflector, i.e., one with zero ray displacement. However, the intrinsic gain (for zero wave activity) of the 2.5-cm-diameter corner-cube array is approximately 21 dB greater than that of the plastic prismatic array. This is a result of the higher optical quality of the glass corner cubes. It is for this reason that the glass corner-cube array actually outperformed the prismatic array when judged on the basis of overall system performance.

The additional losses introduced by a randomly varying air-water interface can be compensated for by increasing, for example, the overall aperture area of the underwater modulated retroreflector. As a means to this end, an array of 37 PLZT modulators, each of 10 cm diameter, was fabricated by Honeywell, Inc. The increase in aperture area will produce a gain of approximately +16 dB in system performance over that of a single 10-cm-diameter PLZT modulator. Appendix E describes in detail the 37-element PLZT modulator array.

The modulator is presently at NOSC; however, due to funding limitations the 37-element array has not been tested in either the laboratory or the field.

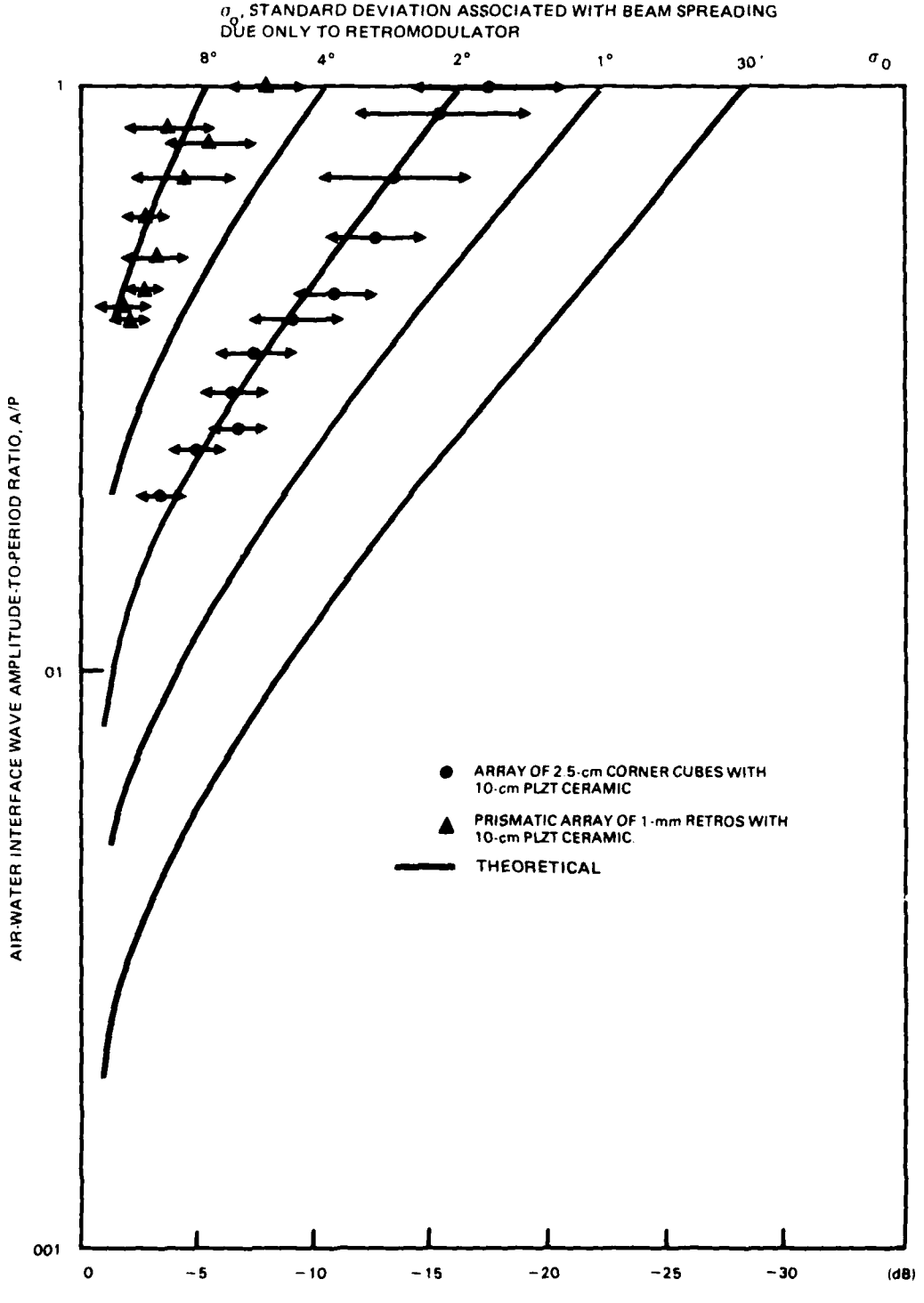

Figure 28. Experimental beam-spread losses due to wave activity at the air-water interface.

CONCLUSIONS

An optical communications system employing a modulated retroreflector in place of one of the two light sources normally used in a conventional optical communications system has been fabricated and tested successfully at NOSC. The transfer of voice information over a line-of-sight atmospheric link was repeatedly demonstrated using either a 3.5-mW HeNe laser (0.633 μm) or a 1-kW incoherent white/near-infrared xenon short-arc light source. Ranges up to 1.6 and 2.5 km were easily achieved using the laser and xenon light sources, respectively. For all atmospheric line-of-sight tests, acoustic-grade $LiNbO_3$ crystals ($\sim$5 cm aperture) were employed as the large-area modulator located in front of the retroreflector. These crystals were used in a phase diffraction grating mode, hence polarizers were not required. The crystals were frequency modulated at 18 kHz with a 4-kHz bandwidth to accommodate voice information. Tests revealed that atmospheric scintillation does indeed degrade system performance in terms of signal fading. However, these degrading effects are much less pronounced during nighttime operation. It was further demonstrated that the degrading effects of atmospheric scintillation could be reduced greatly using aperture-averaging techniques. Increasing the diameter of the transmitted light beam or employing more than one modulated retroreflector reduces the scintillation effects. Experimental results were in good agreement with the link power budget equation predictions of overall system performance. It was firmly established that the retromodulation technique greatly reduces the complexity of one of the terminals of a conventional two-way optical communications system in terms of hardware, acquisition, and pointing and tracking requirements.

Further tests were conducted at NOSC to determine if the retromodulation technique could be used for air-to-underwater communications applications in the presence of a randomly varying air-water interface. For these tests a 10-cm-diameter PLZT modulator, in combination with an array of corner cube retroreflectors, was placed in a waterproof canister and submerged underwater at the TRANSDEC sonar testing facility at NOSC. The active incoherent xenon searchlight transmitter and receiver terminal used in the atmospheric optical communications tests was placed atop Pedro Tower adjacent to the TRANSDEC sonar pool. The active terminal was used to illuminate the underwater retromodulator as well as detect information sent back by the retromodulator. It was found that high-quality voice information could be transferred from the underwater modulator through the randomly varying air-water interface to the active terminal using frequency modulation techniques. The PLZT was modulated at 18 kHz with a 5-kHz bandwidth to accommodate voice information. However, these tests revealed that the beam spreading introduced by refraction at the randomly varying air-water interface gave rise to tremendous losses (tens of dB) over and above those introduced by a perfectly flat air-water interface (Fresnel losses). To compensate for these additional losses, an array of 37 PLZT modulators, each with a diameter of 10 cm, was fabricated by Honeywell, Inc. and delivered to NOSC for underwater testing. However, due to funding limitations the 37-element PLZT array modulator has not yet been tested.

RECOMMENDATIONS

The feasibility of using a modulated retroreflector for atmospheric line-of-sight optical communications has been successfully demonstrated for ranges up to 1.6 km using a 3.5-mW HeNe laser and to 2.5 km using a 1-kW xenon searchlight. It is highly recommended that this technique be pursued for more realistic ranges, say, 16 km (10 miles). Using existing off-the-shelf technology, a range of 16 km should be easily obtainable. To achieve ranges of this order, a 140-dB improvement in system performance would be required to offset the increased geometrical and atmospheric extinction losses. The 140-dB improvement could be obtained, for example, by increasing the laser transmitter power from 3.5 mW (HeNe gas laser) to 5 W (argon gas laser), thereby giving an additional 63 dB.

Expanding the transmitted laser beam diameter by a factor of 20 (~25 mm) achieves an additional 52 dB in transmitter antenna gain. Using high-quality corner-cube retroreflectors and using optical-grade $LiNbO_3$ crystals, as opposed to acoustic-grade material, gives another 12 dB. Increasing the retromodulator diameter from 50 to 75 mm gives an additional 7 dB. Employing a 300-mm-aperture receiver telescope in place of the present 200-mm receiver, which has a 50-mm-diameter obscuration, produces an additional 4 dB; and using a 15-Å interference filter (instead of 30 Å) for rejection of background radiations gains yet another 3 dB. By these means, the additional 140 dB required is obtained.

As for the air-to-underwater type applications, considerable more work needs to be done to give confidence levels comparable to those associated with the atmospheric line-of-sight type applications. In particular, work needs to be done in testing the 37-element PLZT modulator. The effects of the air-water interface on system performance need to be better understood, particularly for open-ocean water. Retroreflector arrays of better optical quality must be obtained and characterized. A blue-green laser light source in the active terminal should be employed to take advantage of the water window at these wavelengths, and a narrowband optical filter should be employed at the active terminal's receiver to minimize the effects of the solar background for daytime operation.

REFERENCES

1. Reference available to qualified requestors.

2. Naval Ocean Systems Center, Large-Aperture Optical Modulator Materials, NOSC TR 165 by R. P. Bocker, et al., Oct. 1977.

3. Naval Underwater Systems Center, Optical Communications Systems Developed by NUSC, New London, NUSC TD 4965 by Albert W. Middleton, June 1975.

4. P. F. Panter, *Modulation, Noise, and Spectral Analysis*, (McGraw-Hill, New York 1965).

5. W. K. Pratt, *Laser Communication Systems*, (John Wiley & Sons, Inc., New York, 1969), pp. 177-178.

6. G. R. Fowles, *Introduction to Modern Optics*, (Holt, Rinehart, and Winston, Inc., New York, 1968), pp. 49-53.

7. I. P. Kaminow and E. H. Turner, *Proc. IEEE* 54, 1374 (1966).

8. H. Engan, *IEEE Trans. Elec. Dev.* ED-16, 1014 (1969).

9. J. W. Goodman, *Introduction to Fourier Optics*, (McGraw-Hill, New York, 1968), pp. 57-70.

10. J. D. Zook, D. Chen and G. N. Otto, *Appl. Phys. Lett.* 11, 159 (1967).

11. A. Papoulis, *Probability, Random Variables, and Stochastic Processes*, (McGraw-Hill, New York, 1965).

12. I. S. Gradshteyn and I. M. Ryzhik, *Table of Integrals, Series, and Products*, (Academic Press, New York, 1965).

APPENDIX A

SYSTEM EQUATIONS FOR THE ATMOSPHERIC COMMUNICATIONS LINK

This appendix presents the fundamental equations pertinent to describing the performance of an optical communications system utilizing the retroreflector/modulator concept. These equations describe a simple model which was developed to evaluate potential applications of the concept and to understand past and future experimental results. No effort has been made to analyze the magnitude and temporal characteristics of signal scintillation, which are expected to be significant and may, under adverse conditions, establish the limiting sensitivity of the system.

A common performance criterion of communication theory is the SNR, defined as the ratio of the average signal power to average noise power at some point in the receiver chain. For the optical communications systems under consideration, the methods of direct detection have been employed. In the direct detection optical receiver, the laser carrier passes through an optical bandpass filter, which serves to reject background radiation, and impinges on the surface of a photodetector. The photodetector produces an output current proportional to the instantaneous intensity of the carrier; it may be regarded as a linear intensity-to-current converter or a quadratic (square law) converter of optical electric field-to-detector current. An electrical low-pass filter having a bandwidth sufficient to pass the information signal follows the photodetector and limits the amount of photodetector noise. The SNR at the receiver output, in terms of the average carrier and background radiation power incident upon the photodetector, is given by (Ref. 5)

$$SNR = (G^2 S_d^2 P_s^2 R_l) / (N_T + N_D + N_B + N_P) \qquad \text{(A-1)}$$

where

G = effective gain of the photodetector
S_d = photodetector responsivity
P_s = received signal power
R_l = effective load resistance
N_T = thermal noise term
N_D = detector dark current noise term
N_B = background noise term
N_P = photon shot noise term.

The photodetector responsivity is given by

$$S_d = \eta q / h f_c \qquad \text{(A-2)}$$

where

η = Detector quantum efficiency
f_c = Laser carrier frequency
q = Electronic charge (1.59×10^{-19} C)
h = Planck's constant (6.63×10^{-34} J-S)

The four noise terms appearing in Eq. (A-1) are due to separate noise sources. The thermal noise power term, N_T, is given by

$$N_T = 4kTB_o \tag{A-3}$$

where

B_o = system electrical bandwidth
T = effective thermal noise temperature of the detector
k = Boltzmann's constant (1.38×10^{-23} J/°K).

The detector dark current noise power, N_D, is given by

$$N_D = 2qB_oG^2I_dR_l \tag{A-4}$$

where

I_d = detector dark current.

The noise power received from background sources is N_B and is given by

$$N_B = 2qB_oG^2S_dP_BR_l \tag{A-5}$$

where

P_B = received background power.

The signal photon shot noise term, N_P, is given by

$$N_P = 2qB_oG^2S_dP_sR_l\,. \tag{A-6}$$

It is noted the thermal noise term and dark current noise term depend solely on the optical photodetector characteristics. Therefore, with an appropriate receiver design, these noise terms can be minimized. The background noise term depends upon both the photodetector characteristics and background power detected by the receiver. Examples of background noise sources are direct sunlight, blue-sky light, moonlight, starlight, and bioluminescent light, just to mention a few. With properly designed optical bandpass filters, the background noise term can be minimized. The signal photon shot noise term depends upon both detector

characteristics and the signal power received. For the case when the thermal, dark current, and background noise terms are minimized and the shot noise term dominates, then a condition of signal photon shot-noise-limited operation exists. This represents the optimum mode for a direct detector receiver, the direct detection receiver SNR is maximum for carrier shot-noise-limited operation.

The received signal power is dependent upon characteristics of the active terminal light source, the outlink channel geometry, the passive terminal retroreflector/modulator combination, the backlink channel geometry, and the active terminal optical receiver. Symbolically,

$$P_s = \begin{bmatrix}\text{Active Terminal}\\ \text{Light Source}\end{bmatrix}\begin{bmatrix}\text{Outlink}\\ \text{Channel}\end{bmatrix}\begin{bmatrix}\text{Passive Terminal}\\ \text{Retromodulator}\end{bmatrix}\begin{bmatrix}\text{Backlink}\\ \text{Channel}\end{bmatrix}\begin{bmatrix}\text{Active Terminal}\\ \text{Optical Receiver}\end{bmatrix}$$

Referring to Fig. A-1, the mathematical expression for the signal power, P_s, is given by

$$P_s = (P_a/\Omega_a)\,(e^{-br}/r^2)\,(A_m E_m M_m/\Omega_m)\,(e^{-br}/r^2)\,(E_d A_d), \qquad \text{(A-7)}$$

where

P_a = transmitter power of the active terminal
Ω_a = solid angle of the transmitted laser light cone
A_m = area of the retroreflector/modulator entrance aperture
E_m = transmission efficiency of the retroreflector/modulator
M_m = retroreflector/modulator transmitter modulation index
Ω_m = solid angle of the retroreflected laser light cone
E_d = transmission efficiency of the active terminal receiver
A_d = area of the active terminal optical receiver aperture
r = range between active and passive terminals
b = atmospheric extinction coefficient

Equation (A-7) corresponds to the case when the transmitted laser beam spot size at the passive terminal receiver is larger than the passive terminal entrance aperture. This condition holds for the geometries considered. Further discussion on this point may be found in Ref. 1.

The solid angles Ω_a and Ω_m appearing in Eq. (A-7) are related to the half-angles of the corresponding cones by

$$\Omega_a = 2\pi(1 - \cos\phi_a) \qquad \text{(A-8)}$$

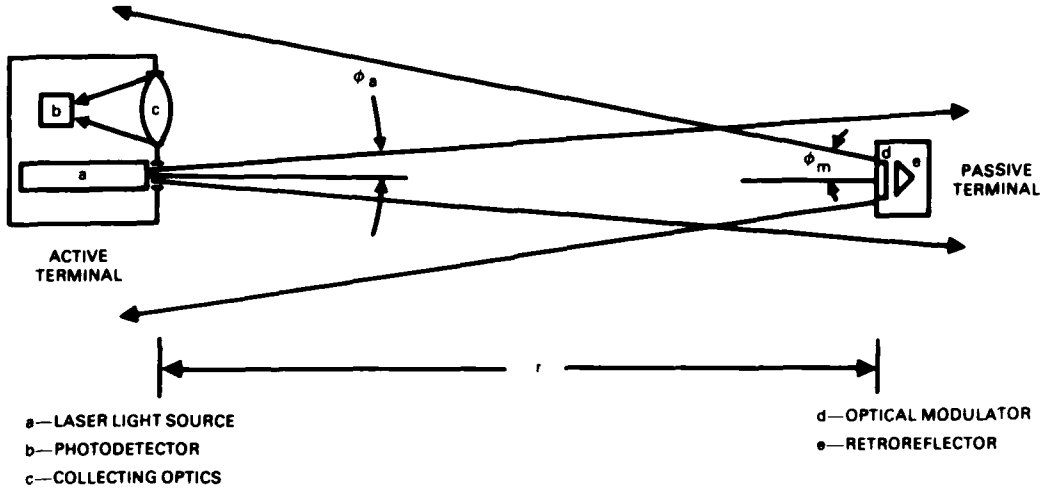

Figure A-1. Simplified diagram of the atmospheric communications link.

and

$$\Omega_m = 2\pi(1 - \cos\phi_m). \tag{A-9}$$

Equation (A-7) is very useful in telling us what sort of gains or losses result by changing the values of the quantities in this equation. The use of Eq. (A-1) through (A-9) allows us to predict the optical communications system performance under a given set of circumstances.

It is of interest to look at limiting forms of Eq. (A-1), that is, those cases for which one of the noise terms dominates. For the case of thermal-noise-limited operation, Eq. (A-1) reduces to the form

$$SNR = (q^2/4kh^2c^2)\,(G^2\eta^2R_1/TB_o)\,(P_s^2\lambda_c^2), \tag{A-10}$$

where we have used

$$f_c = c/\lambda_c. \tag{A-11}$$

λ_c is the wavelength of the laser carrier and c the speed of light in free space (3×10^{10} cm/s). Equation (A-10) reduces to

$$SNR = (1.2)\,(10^{14})\,(G^2\eta^2R_1/TB_o)\,(P_s^2\lambda_c^2) \tag{A-12}$$

when R_1 is expressed in ohms, T in degrees Kelvin, B_o in hertz, P_s in watts, and λ_c in angstroms. For the case of dark-current-limited operation, Eq. (A-1) simplifies to the following form:

$$SNR = (q/2h^2c^2)\,(\eta^2/B_oI_d)\,(P_s^2\lambda_c^2). \tag{A-13}$$

Equation (A-13) reduces to the form

$$SNR = (2.0)\,(10^{13})\,(\eta^2/B_oI_d)\,(P_s^2\lambda_c^2) \tag{A-14}$$

if B_o is expressed in hertz, I_d in milliamperes, P_s in watts, and λ_c in angstroms. For the case of background-limited operation, Eq. (A-1) yields the form

$$SNR = (1/2hc)(\eta/B_o)(P_s^2\lambda_c/P_b). \quad \text{(A-15)}$$

This equation simplifies to

$$SNR = (2.5)(10^{14})(\eta/B_o)(P_s^2\lambda_c/P_b) \quad \text{(A-16)}$$

if B_o is expressed in terms of hertz, P_s in watts, P_b in watts, and λ_c in angstroms. Finally, for photon-shot-noise-limited operation, Eq (A-1) takes on the form

$$SNR = (1/2hc)(\eta/B_o)(P_s\lambda_c). \quad \text{(A-17)}$$

Equation (A-17) reduces to

$$SNR = (2.5)(10^{14})(\eta/B_o)(P_s\lambda_c) \quad \text{(A-18)}$$

when B_o is in hertz, P_s in watts, and λ_c in angstroms.

With the use of Eq. (A-12), (A-14), (A-16), and (A-18), Eq. (A-1) can be expressed in the form

$$SNR = \frac{(2.5)(10^{14})(\eta/B_o)(P_s\lambda_c)}{1 + (P_b/P_s) + (12.4I_d/\eta P_s\lambda_c) + (2.1T/G^2\eta P_s\lambda_c R_1)} . \quad \text{(A-19)}$$

This equation clearly demonstrates for the optimum case, namely, photon-shot-noise-limited operation, that the following inequalities must be satisfied:

$$P_b \ll P_s$$

$$I_d \ll \eta P_s\lambda_c/10$$

$$T \ll G^2\eta P_s\lambda_c R_1/2.$$

APPENDIX B

SYSTEM EQUATIONS FOR THE AIR-TO-UNDERWATER COMMUNICATIONS LINK

This appendix presents the fundamental equations pertinent to describing the performance of an optical communications system utilizing the retroreflector/modulator concept for air-to-underwater communications. Since the system employed for this channel is basically the same as that employed for the line-of-sight atmospheric communications channel, the system equations are very similar. A detailed discussion of the atmospheric communications system equations is presented in Appendix A. It is highly recommended that Appendix A be read prior to any further reading.

As with the atmospheric communications system approach, the methods of direct detection are employed. As discussed in Appendix A, the SNR at the receiver output is given by

$$SNR = (G^2 S_d^2 P_s^2 R_1) \Big/ (N_T + N_D + N_B + N_P), \tag{B-1}$$

where again

G = effective gain of the photodetector
S_d = photodetector responsivity
P_s = received signal power
R_1 = effective load resistance
N_T = thermal noise term
N_D = detector dark current noise term
N_B = background noise term
N_P = photon shot noise term

The only term here whose character is different from the terms described in Appendix A is the received signal power term, P_s.

For the air-to-underwater communications channel, the received signal power is dependent upon characteristics of the active terminal light source, the outlink channel geometry, the passive terminal retroreflector/modulator combination, the backlink channel geometry, and the active terminal optical receiver. That is,

$$P_s = \begin{bmatrix}\text{Active Terminal}\\ \text{Light Source}\end{bmatrix} \begin{bmatrix}\text{Outlink}\\ \text{Channel}\end{bmatrix} \begin{bmatrix}\text{Passive Terminal}\\ \text{Retromodulator}\end{bmatrix} \begin{bmatrix}\text{Backlink}\\ \text{Channel}\end{bmatrix} \begin{bmatrix}\text{Active Terminal}\\ \text{Optical Receiver}\end{bmatrix}$$

Referring to Fig. B-1, the mathematical expression for the signal power, P_s, is given by

$$P_s = (P_a/\Omega_a)(e^{-bh}Te^{-b'd}/r_1^2)(A_mE_mM_m/\Omega_m)(e^{-bh}Te^{-b'd}/r_2^2)(E_c A_d) \quad \text{(B-2)}$$

where

P_a = transmitter power of the active terminal
Ω_a = solid angle of the transmitted laser light cone
A_m = area of the retroreflector/modulator entrance aperture
E_m = transmission efficiency of the retroreflector/modulator
M_m = retroreflector/modulator transmitter modulation index
Ω_m = solid angle of the retroreflected light cone in water
E_d = transmission efficiency of the active-terminal receiver
A_d = area of the active-terminal optical receiver aperture
h = altitude of active transmitter above air-water interface
d = depth of passive transmitter below air-water interface
b = atmospheric extinction coefficient
b' = underwater extinction coefficient
T = transmission efficiency of the air-water interface

The quantities r_1 and r_2 appearing in Eq. (B-2) are defined by

$$r_1 = h + d[(1 - \sin^2\phi_a) / (n^2 - \sin^2\phi_a)]^{1/2} \quad \text{(B-3)}$$

and

$$r_2 = d + h[(1 - \sin^2\phi_m) / (1/n^2 - \sin^2\phi_m)]^{1/2} \quad \text{(B-4)}$$

where

n = index of refraction of water
ϕ_a = half-angle of the transmitted laser light cone
ϕ_m = half-angle in water of the retroreflected light cone.

Equation (B-2) corresponds to the case when the transmitted light beam spot size at the passive terminal receiver is larger than the passive-terminal entrance aperture, which holds for the geometries considered. The quantities r_1 and r_2 take on a more simplified form for the case when ϕ_a and ϕ_m are small, that is,

$$r_1 \simeq h + d/n \quad (\text{small } \phi_a) \quad \text{(B-5)}$$

and

$$r_2 \simeq d + nh \qquad (\text{small } \phi_m)\,. \tag{B-6}$$

The transmission efficiency of the air-water interface, T, for the case of a perfectly flat interface is determined through the Fresnel coefficients (Ref. 6). However, for the case of a randomly varying air-water interface the quantity T has associated with it additional losses due to beam spreading. The randomly varying air-water interface case is further treated in Appendix F.

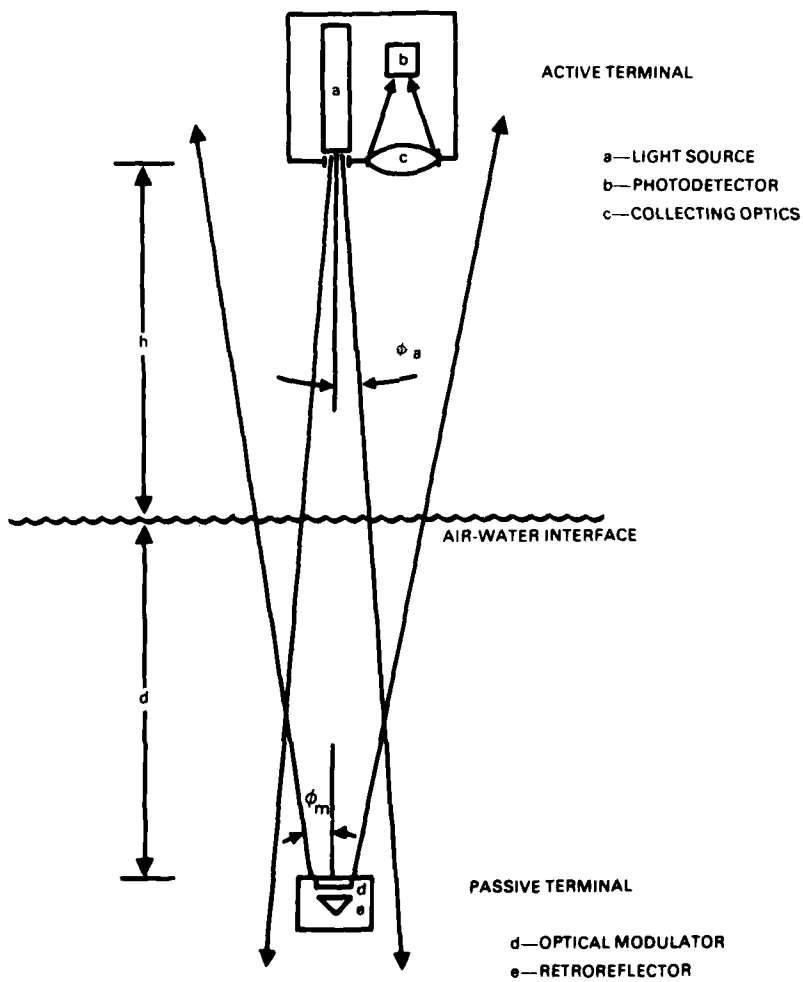

Figure B-1. Simplified diagram of the air-to-underwater communications link.

APPENDIX C

LITHIUM NIOBATE POCKELS EFFECT CRYSTALS

The Pockels effect is the alteration of the refractive properties of a piezoelectric crystal caused by the application of a strong external electric field. The effect is linearly related to the electric field strength. The basic configuration of interest, shown in Fig. C-1, consists of an electrooptical crystal having a set of interdigital electrodes fabricated on one of the large optical surfaces of the crystal and a set of driver electronics. Application of a potential difference across the terminals of the crystal sets up a spatially periodic electric field distribution within the crystal, which in turn gives rise to a spatially periodic variation in its optical indices of refraction. The result is that we have a means for realizing a phase diffraction grating whose diffractive properties can be altered by the application of an external electric field. The diffraction grating modulator has the property that the input beam of light is split into a zeroth-order (the order of interest) beam and a number of higher order diffracted beams. By changing the magnitude of the applied voltage it is possible to change the distribution of light energy appearing in the various orders. The result of interest is that the zeroth diffraction order can be amplitude modulated in time.

THEORY OF OPERATION

In most crystals, the interaction of electromagnetic radiation (light) with the crystalline material is a highly involved and complicated process. Fortunately, the theoretical models describing this interaction are well developed and give tremendous insight into how the crystal should be cut, polished, and oriented with respect to the direction of the applied electric field to take full advantage of the electrooptic Pockels effect. In addition, these models indicate the preferred directions of light propagation within the crystal and the preferred polarization states. For the purpose of this study, a classical electromagnetic approach to the problem is quite acceptable.

Basic electromagnetic theory holds that the stored electric field energy density, W_e, associated with an electromagnetic wave in a material in the absence of any applied electric field is given by the simple equation

$$W_e = (1/8\pi)\,\bar{E}\cdot\bar{D}, \tag{C-1}$$

where $\bar{E}$ and $\bar{D}$ are the electric field and electric displacement vectors, respectively, associated with the electromagnetic disturbance. The cgs system of units is employed. The electric field vector, $\bar{E}$, and the displacement vector, $\bar{D}$, are related through the macroscopic polarization vector, $\bar{P}$, by the equation

$$\bar{D} = \bar{E} + 4\pi\bar{P}. \tag{C-2}$$

The basic distinguishing optical feature of the crystalline state is the fact that crystals are generally electrically anisotropic. This means that the polarization, $\bar{P}$, produced in the crystal by the electric field is not just a simple scalar constant times the electric field, but varies in a manner that depends on the direction of the electric field in relation to the crystal lattice.

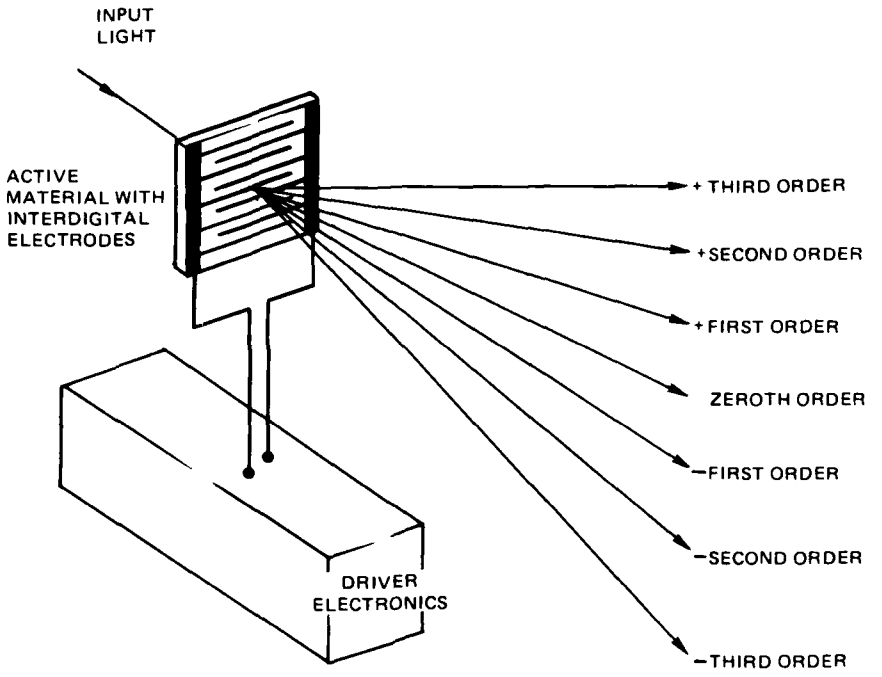

Figure C-1. Electrooptical modulator employing the transverse Pockels effect with interdigital electrodes.

Thus the actual dependence of $\bar{P}$ on $\bar{E}$ is expressible as a tensor relation in the form

$$\bar{P} = \overline{\overline{X}}\,\bar{E}, \tag{C-3}$$

where $\overline{\overline{X}}$ is the susceptibility tensor:

$$\overline{\overline{X}} = \begin{bmatrix} X_{11} & X_{12} & X_{13} \\ X_{21} & X_{22} & X_{23} \\ X_{31} & X_{32} & X_{33} \end{bmatrix} \tag{C-4}$$

There exists a set of coordinate axes, called the principal axes, such that the susceptibility tensor assumes the diagonal form

$$\overline{\overline{X}} = \begin{bmatrix} X_{11} & 0 & 0 \\ 0 & X_{22} & 0 \\ 0 & 0 & X_{33} \end{bmatrix} \tag{C-5}$$

The three X's in Eq. (C-5) are known as the principal susceptibilities. In the principal axes frame we thus find from Eq. (C-2), (C-3), and (C-5) that the components of $\bar{E}$ and $\bar{D}$ are

related through the scalar equations

$$\begin{aligned} D_x &= n_1^2 E_x \\ D_y &= n_2^2 E_y \\ D_z &= n_3^2 E_z \end{aligned} \tag{C-6}$$

where the n's are the principal indices of refraction and are given by the equations

$$\begin{aligned} n_1^2 &= 1 + 4\pi X_{11} \\ n_2^2 &= 1 + 4\pi X_{22} \\ n_3^2 &= 1 + 4\pi X_{33} \end{aligned} \tag{C-7}$$

With Eq. (C-6), the equation for the electric field energy density stored can be rewritten in the form

$$8\pi W_e = D_x^2 / n_1^2 + D_y^2 / n_2^2 + D_z^2 / n_3^2 . \tag{C-8}$$

Equation (C-8) tells us that the constant energy (W_e) surfaces in (D_x,D_y,D_z) space are ellipsoids. For convenience let us write x, y, z in place of $D_x/(8\pi W_e)^{1/2}$, $D_y/(8\pi W_e)^{1/2}$, $D_z/(8\pi W_e)^{1/2}$ and consider these as Cartesian coordinates in space. Then Eq. (C-8) reduces to

$$x^2/n_1^2 + y^2/n_2^2 + z^2/n_3^2 = 1 . \tag{C-9}$$

This equation is commonly referred to as the index ellipsoid equation, the optical indicatrix equation, or the reciprocal ellipsoid equation. The properties of the index ellipsoid described by Eq. (C-9) can be seen from a simple example. If an electromagnetic plane wave propagating through the crystal has its normal lying along the z-direction, then we consider the ellipse formed by the index ellipsoid and the z = 0 plane. The directions of the major and minor axes of this ellipse are those of the two allowed polarization eigenstates; for this case the x- and y- directions specify the allowed polarizations. The refractive indices associated with these polarization eigenstates are given by the length of the semiaxes of the ellipse, for this case n_1 and n_2. In a more general case, the wave normal direction can be chosen arbitrarily, and the two indices can be obtained as the semiaxes of the elliptical section perpendicular to the arbitrary direction.

For the case of materials in the presence of an externally applied electric field, such as electrooptical crystals exhibiting the Pockels effect, the indices of refraction appearing in the index ellipsoid equation change in magnitude with the application of the external electric field. In addition, certain types of electrooptical crystals have the property that the index ellipsoid actually changes orientation as a result of the applied electric field. For these types of crystals the principal axes associated with the crystal will change direction with the application of the external field. In order to handle these additional effects, a more generalized index ellipsoid equation must be used. It has been shown that if the bound outer electrons in the crystalline material, which are primarily responsible for the resulting macroscopic polarization, $\bar{P}$, are treated as aharmonic oscillators (i.e., nonlinear restoring forces), then the

resulting index ellipsoid equation of interest takes on the form

$$(1/n_1^2 + a_{11})x^2 + (1/n_2^2 + a_{22})y^2 + (1/n_3^2 + a_{33})z^2$$

$$+ 2\,a_{23}\,yz + 2a_{31}\,zx + 2\,a_{12}\,xy = 1. \qquad \text{(C-10)}$$

In general, however, x, y, and z no longer correspond to the principal directions. The coefficients a_{ij} appearing in Eq. (C-10) are related to the Cartesian components of the externally applied electric field, $\bar{E}$, by the matrix equation

$$\begin{bmatrix} a_{11} \\ a_{22} \\ a_{33} \\ a_{23} \\ a_{31} \\ a_{12} \end{bmatrix} = \begin{bmatrix} r_{11} & r_{12} & r_{13} \\ r_{21} & r_{22} & r_{23} \\ r_{31} & r_{32} & r_{33} \\ r_{41} & r_{42} & r_{43} \\ r_{51} & r_{52} & r_{53} \\ r_{61} & r_{62} & r_{63} \end{bmatrix} \begin{bmatrix} E_x \\ E_y \\ E_z \end{bmatrix} \qquad \text{(C-11)}$$

The 3 x 6 matrix of coefficients r_{ij} is commonly known as the electrooptic tensor. All electrooptic Pockels crystals have such a tensor uniquely associated with them. The form, but not the magnitude, of the tensor coefficients r_{ij} can be derived from group symmetry considerations, which dictate the particular 18 r_{ij} coefficients that are zero and the relationships that exist between the remaining coefficients. The indices of refraction appearing in Eq. (C-10) represent the principal indices of refraction of the crystal in the absence of an applied electric field. We see from Eq. (C-11) that when the applied electric field is zero, the coefficients a_{ij} are also zero, implying that the index ellipsoid equation in Eq. (C-10) degenerates to the specialized version represented by Eq. (C-9). Therefore, using Eq. (C-10) and (C-11) with a knowledge of the values of the nonzero Pockels coefficients allows us to adequately describe the interaction of light with an electrooptic crystal exhibiting the Pockels effect.

The Pockels electrooptic crystal $LiNbO_3$ belongs to the trigonal 3M (C_{3v}) class of crystals. The electrooptic tensor describing this crystal is of the form

$$\begin{bmatrix} 0 & -r_{22} & r_{13} \\ 0 & r_{22} & r_{13} \\ 0 & 0 & r_{33} \\ 0 & r_{42} & 0 \\ r_{42} & 0 & 0 \\ -r_{22} & 0 & 0 \end{bmatrix}$$

where the nonzero Pockels coefficients have the values

$$r_{13} = 9.6 \times 10^{-12} \text{ m/V}$$
$$r_{22} = 6.6 \times 10^{-12} \text{ m/V}$$
$$r_{33} = 31.0 \times 10^{-12} \text{ m/V}$$
$$r_{42} = 32.0 \times 10^{-12} \text{ m/V}$$

for 0.633-μm light. In addition, the indices of refraction for this wavelength are given by

$$n_1 = n_o = 2.291$$
$$n_2 = n_o = 2.291$$
$$n_3 = n_e = 2.200 \ .$$

It is noted that the $LiNbO_3$ crystal is a negative uniaxial crystal whose optic axis lies along the z-direction. For a uniaxial crystal, the quantities n_o and n_e are referred to as the ordinary and extraordinary indices of refraction, respectively. By going back to the index ellipsoid equation and using the electrooptic tensor information for $LiNbO_3$, we find that the optimum geometry for using $LiNbO_3$ as an optical modulator is the transverse mode of operation. This corresponds to the case in which the applied electric field is approximately at right angles to the direction of light propagation. To keep voltage levels down, an interdigital electrode configuration, as shown in Fig. C-2, is preferred over the parallel-plate electrode geometry normally used. In this figure is depicted a y-cut $LiNbO_3$ crystal with the interdigital electrodes lying perpendicular to the z-axis (optic axis) of the crystal. Wave propagation would normally be along the y-direction.

Our analytical model for the crystal modulator assumes that the crystal occupies the half-space $y \leq 0$, the interdigital array is of infinite extent in the x- and z-directions, and the electrode thickness is vanishingly small. For light propagating parallel to the y-axis, the phase change $\Delta\phi_i$ is given by the equation (Ref. 7)

$$\Delta\phi_i(z) = \frac{\pi}{\lambda} n_i^3 r_{i3} \int_{-\infty}^{0} E_z(y,z)dy \qquad i = 1, 3 \tag{C-12}$$

where E_z is the component of applied electric field parallel to the optic axis of the crystal, λ is the free-space wavelength, n_i is the refractive index, and the subscripts i = 1 and 3 refer to incident beam polarization along the x- and z-axes, respectively. The integral in Eq. (C-12) can be evaluated using Gauss' law, which becomes

$$\int_S \bar{D} \cdot d\bar{S} = Q(y \to 0^-)/2 \tag{C-13}$$

for the surface S and is illustrated in Fig. C-3, where $Q(y \to 0^-)$ is the charge on the bottom surface of an electrode. By symmetry, D_z vanishes for a plane that bisects an electrode, and symmetry arguments (Ref. 8) can also be used to show that $D_y = 0$ in the plane y = 0. Since $|E| \to 0$ for $y \to -\infty$, the integral in Eq. (C-13) reduces to

$$\int_S \bar{D} \cdot d\bar{S} = \epsilon_3 L \int_{-\infty}^{0} E_z(y,z)dy \tag{C-14}$$

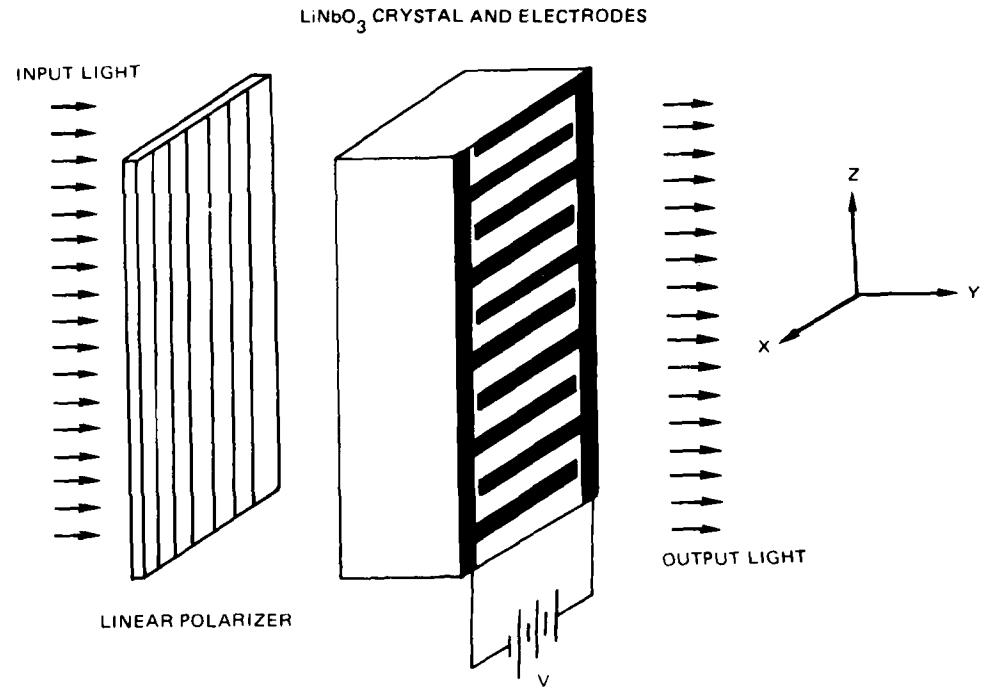

Figure C-2. Tunable diffraction grating modulator geometry for the $LiNbO_3$ crystal.

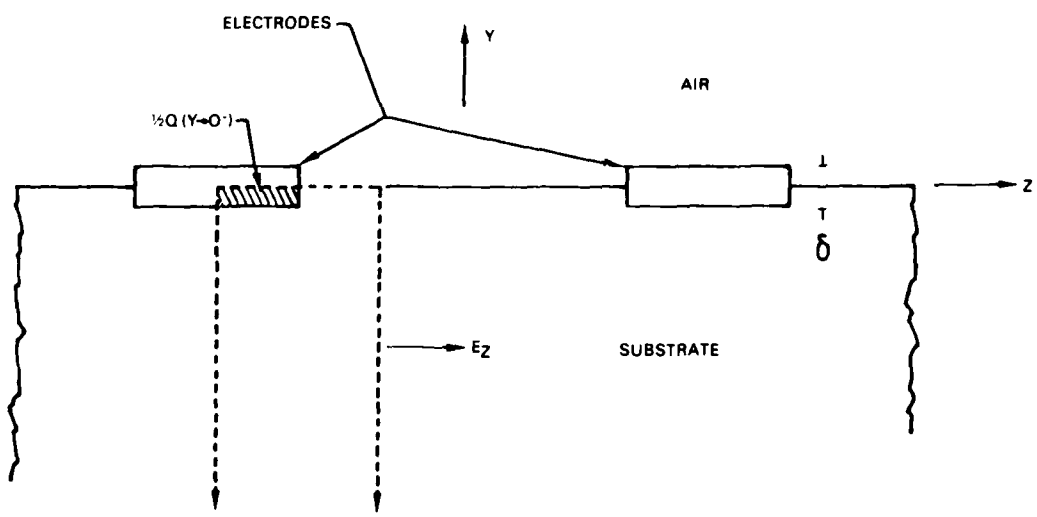

Figure C-3. Surface over which the Gauss law integral is calculated. The surface at y = 0 bisects the electrode, and encloses charge only on the bottom. The electrode thickness is assumed to be vanishing small.

where L is the electrode length. Since this expression holds for any value of z in the gap between electrodes, it follows from Eq. (C-12) and (C-13) that $\Delta\phi_i$ is uniform (independent of z) in the gap and is given by,

$$\Delta\phi_i = \pi n_i^3 r_{i3} Q(y \to 0^-)/(2\lambda\epsilon_3 L) . \qquad \text{(C-15)}$$

But, for the assumed electrode configuration (Ref. 8)

$$Q(y \to 0^-) = (\epsilon_1\epsilon_3)^{1/2} LV K(k)/K'(k) \qquad \text{(C-16)}$$

with V the applied voltage, $k = \cos[(\pi/2)(g/d)]$, g the clear aperture between electrodes, d the electrode center-to-center spacing, K(k) the complete elliptic integral of the first kind, and $K'(k) = K[(1-k^2)^{1/2}]$. ϵ_1 and ϵ_3 are the dielectric coefficients associated with the x- and z-directions, respectively. Combining Eq. (C-15) and (C-16) yields

$$\Delta\phi_i = \pi(\epsilon_1/\epsilon_3)^{1/2} n_i^3 r_{i3} V K(k)/2\lambda K'(k) \qquad i = 1, 3. \qquad \text{(C-17)}$$

With the use of the far-field diffraction integral equations (Ref. 9), the light intensity in the m^{th} diffraction order, $I_i(m,V)$, is predicted to be

$$I_i(m,V) = I_i(0,0) \frac{\sin^2(m\pi g/2d)}{(m\pi g/2d)^2} \cos^2(m\pi/2 + \pi V/2v_{\pi i}) \qquad i = 1, 3 \qquad \text{(C-18)}$$

where $v_{\pi i}$ is the voltage required for a relative phase change of one-half wavelength (π radians) between adjacent interelectrode gaps. From Eq. (C-18), with $\Delta\phi_i = \pi/2$, it is found that

$$v_{\pi i} = (\epsilon_3/\epsilon_1)^{1/2} \lambda K'(k)/n_i^3 r_{i3} K(k) \qquad i = 1, 3. \qquad \text{(C-19)}$$

LABORATORY EXPERIMENTAL RESULTS

The results reported here concern modulator crystal devices fabricated from acoustic-grade y-cut $LiNbO_3$ plates* with dimensions x = 45 mm, y = 3 mm, and z = 55 mm. The large faces were parallel to within 2 min of arc and were polished to a flatness of $\lambda/2$. Interdigital aluminum electrodes, 0.1 μm thick and 0.1 mm wide with 1.0-mm center-to-center spacings, were delineated by photolithography on one of the large faces. The effective area of the interdigital electrode structure was 16.1 cm^2 (3.5 x 4.6 cm). The electrodes were oriented perpendicular to the z-axis (optic axis) in order to make use of the large r_{33} electrooptic coefficient of lithium niobate. Figure C-4 shows just the $LiNbO_3$ crystal, with interdigital electrodes, bus bars, and connecting wires.

Experimental results in the laboratory were obtained with a collimated 0.633-μm HeNe laser beam incident normal to the crystal surface and a Fourier transforming lens to isolate the various diffraction orders. The measured dependence of intensity on applied dc voltage for the first two diffraction orders is plotted in Fig. C-5 for both x- and z-polarizations. Measurements were made for both positive and negative voltages, and it was found that variations in intensity for changes from +V to -V were usually less than 2% and never greater than 5%. The curves in Fig. C-5, are averages for both voltage polarities. The zeroth-order

* Crystals grown, cut, and polished by Union Carbide Co., San Diego, CA.

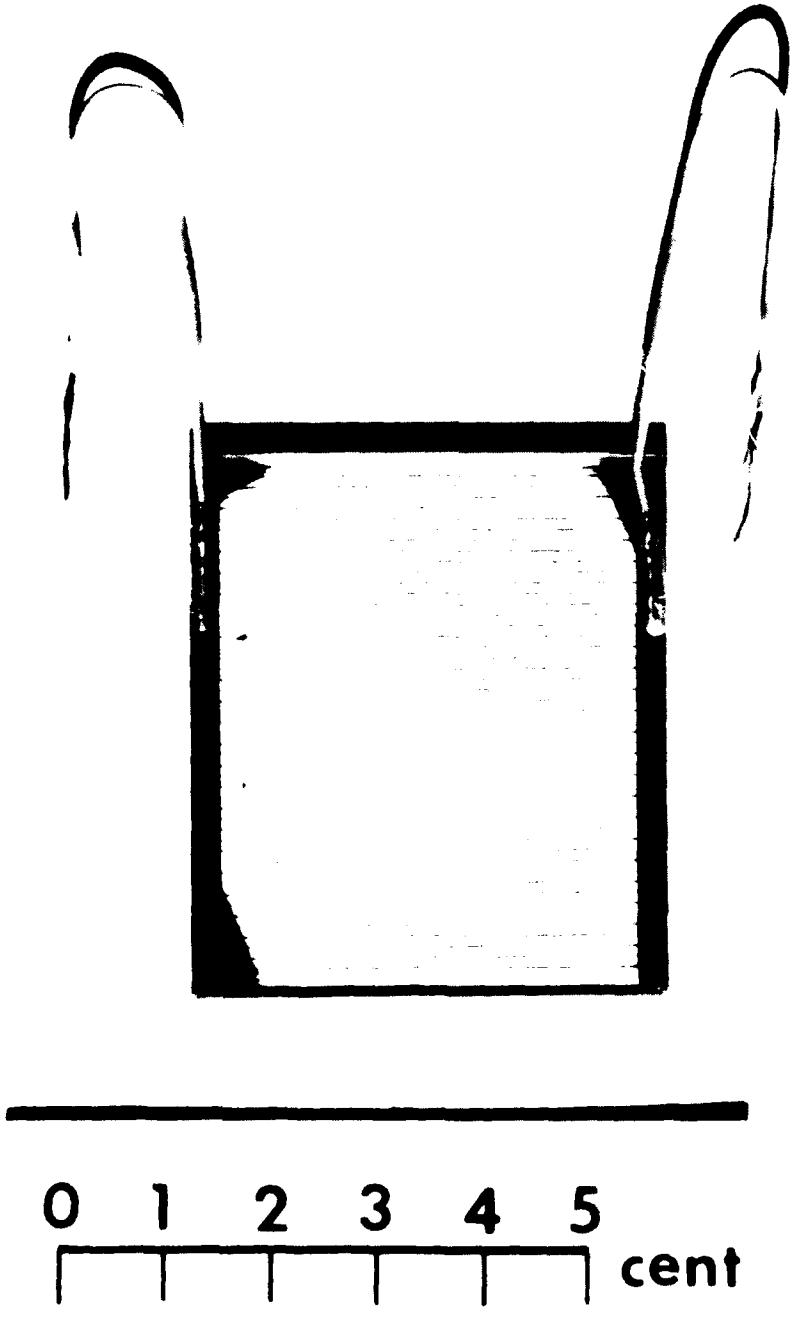

Figure C-4. Lithium niobate crystal, with interdigital electrodes, bus bars, and connecting wires.

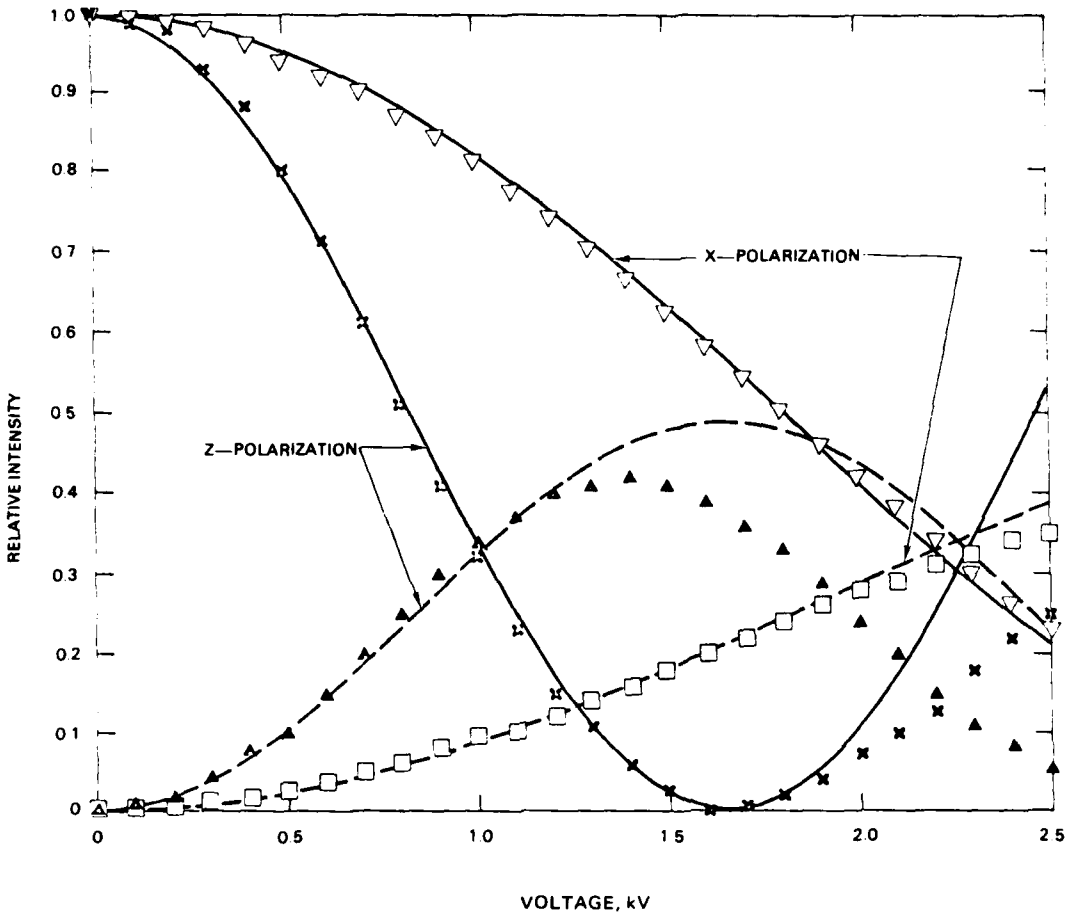

Figure C-5. Comparison of measured and predicted dependence of intensity on applied voltage for zeroth order (solid curves) and first order (dashed curves).

extinction ratio for z-polarization was 100:1 for V = 1650 V for a single-pass transmission. The data are compared with theoretical curves plotted from Eq. (C-18), using the values $v_{\pi 3}$ = 1650 V and $v_{\pi 1}$ = 3600 V, which give the best fit to measured curves for the zeroth order. These experimentally determined values of v_π compare with the theoretical values $v_{\pi 3}$ = 2270 V and $v_{\pi 1}$ = 6520 V calculated from Eq. (C-19), using published values for low-frequency optical and dielectric constants (Ref. 10) of $LiNbO_3$. It is noted that the predicted values for v_π are substantially greater than measured values for both polarizations, and the data of Fig. C-5 deviate significantly from predicted behavior for z-polarization at the higher voltages. Data for higher diffraction orders also showed significant differences when compared with theoretical plots. No explanation for these discrepancies is readily apparent. It should also be mentioned that the theoretical value of 175 pF for the capacitance of the device, obtained from the formula (Ref. 8)

$$C = [\epsilon_0 + (\epsilon_1 \epsilon_3)^{1/2}]\ LK(k)/K'(k), \qquad \text{(C-20)}$$

where L is the total length of the interdigital pairs, is slightly higher than the measured value of 165 pF.

APPENDIX D

LEAD LANTHANUM ZIRCONATE TITANATE KERR EFFECT CERAMICS

The Kerr effect is the occurrence of induced birefringence in a transparent isotropic medium when it is placed in an external electric field. The medium behaves like a uniaxial crystal whose optic axis lies along the direction of the applied electric field. The modulation effect is related to the square of the electric field strength. The geometry used for the conventional Kerr-type modulators is depicted in Fig. D-1. The device shown consists of two parallel-plate conductors sandwiching the electrooptic Kerr material. If a polarizer and analyzer are crossed and are oriented at ±45 deg with respect to the electric axis of the modulator, no light is transmitted except when the electric field is turned on. By changing the magnitude of the applied electric field as a function of time, it is thereby possible to also change the transmission of the Kerr modulator with time.

PLZT is presently receiving considerable attention as an optical Kerr shutter and modulator. The geometry of present PLZT devices uses an interdigital electrode approach to keep voltage levels down, as depicted in Fig. D-2. PLZT has the advantage that it is a polycrystalline ceramic, which allows it to be formed with apertures up to 13 cm in diameter by means of present-day hot-pressing techniques. Its half-wave voltage is on the order of several hundred volts, it has kilohertz response times, and it can be fabricated rather inexpensively.

LABORATORY OPERATION AND RESULTS

PLZT is a clear ferroelectric ceramic whose optical transmission properties can be altered by the application of an external electric field. During the last few years a considerable amount of experimental work has been performed by the government and private industry to ascertain the basic properties of this ceramic material. No unified theory equivalent to the index ellipsoid approach used to describe the electrooptic Pockels effect has yet emerged to explain PLZT behavior.

A particular area of concern at various laboratories has been to alter the optical transmission characteristics of the PLZT ceramic by the application of an external electric field. A variety of techniques have been explored. The most common one in use today entails fabricating a set of interdigital electrodes on the two large surfaces of a thin PLZT ceramic wafer and operating the material in a transverse mode. There are presently a number of application areas where PLZT is being used in a transverse mode of operation. For the most part, however, these applications require that the ceramic be used only in an on/off optical shutter mode of operation. For example, PLZT is currently being developed as a lens element for nuclear flash-blindness prevention goggles, as a lens element for glasses used for stereoscopic TV viewing, and as a lens element in welder's helmets. Very little work has been done in evaluating these ceramic materials for their analog modulation capabilities, particularly for a large-area ceramic wafer.

To investigate the potential usefulness of PLZT as a large-aperture optical modulator, 10-cm-diameter PLZT ceramic wafers were purchased from Honeywell, Inc. The wafer material consists of 65% lead zirconate and 35% lead titanate, with 9.5 atomic percent

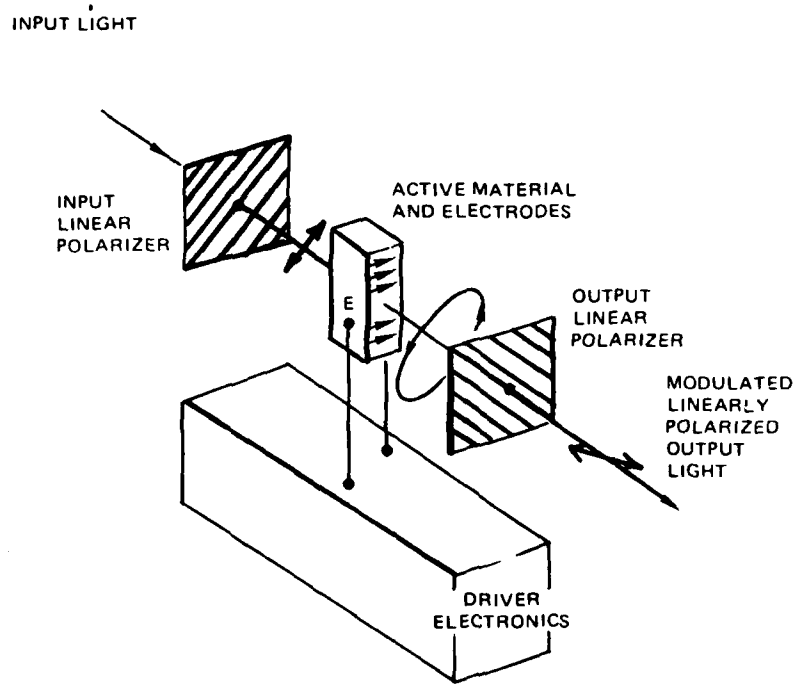

Figure D-1. Electrooptic modulator employing the transverse Kerr effect.

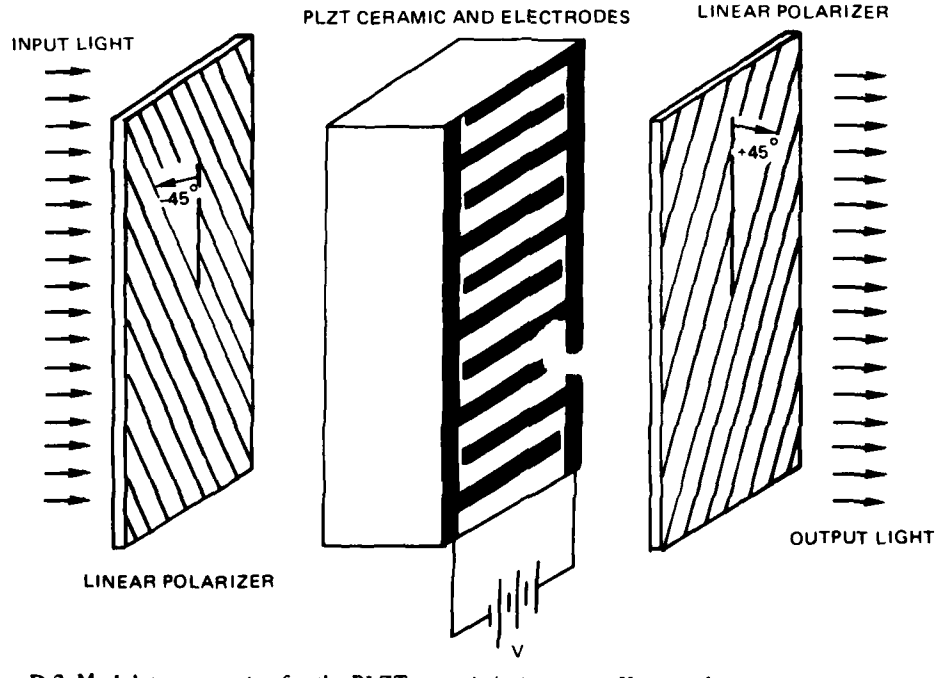

Figure D-2. Modulator geometry for the PLZT ceramic in transverse Kerr mode.

of the lead replaced with lanthanum. This particular composition exhibits a large transverse quadratic effect with minor hysteresis effects. The most important property of interest is the change in the optical transmission of the ceramic with applied voltage. The curve in Fig. D-3 represents the transmission response of a 10-cm-diameter PLZT wafer, for two-way transmission using 0.633-μm light, as a function of applied dc voltage. A combination of gold and chrome interdigital electrodes, 1 μm thick, located on both surfaces of the ceramic wafer was used for electrically exciting the ceramic. The center-to-center spacing between electrodes is about 1.02 mm. For the two-way transmission experiment, a single polarizer was used that served both as an input polarizer and an output analyzer. The transmission axis of the polarizer was oriented 45 deg from the interdigital electrode fingers on the PLZT wafer. As seen from the experimental data in Fig. D-3, the transmission response of the ceramic is fairly flat from zero to about 400 V. Above this level the transmission falls off rapidly to a minimum at about 600 V, and it then begins to increase with a further increase in voltage. The associated depth of modulation, defined by the equation

$$DM = (T_{max} - T_{min})/(T_{max} + T_{min}), \quad \text{(D-1)}$$

was measured at better than 90% based on these data. T_{max} and T_{min} represent the maximum and minimum values of the transmission of the ceramic, from Fig. D-3. An important

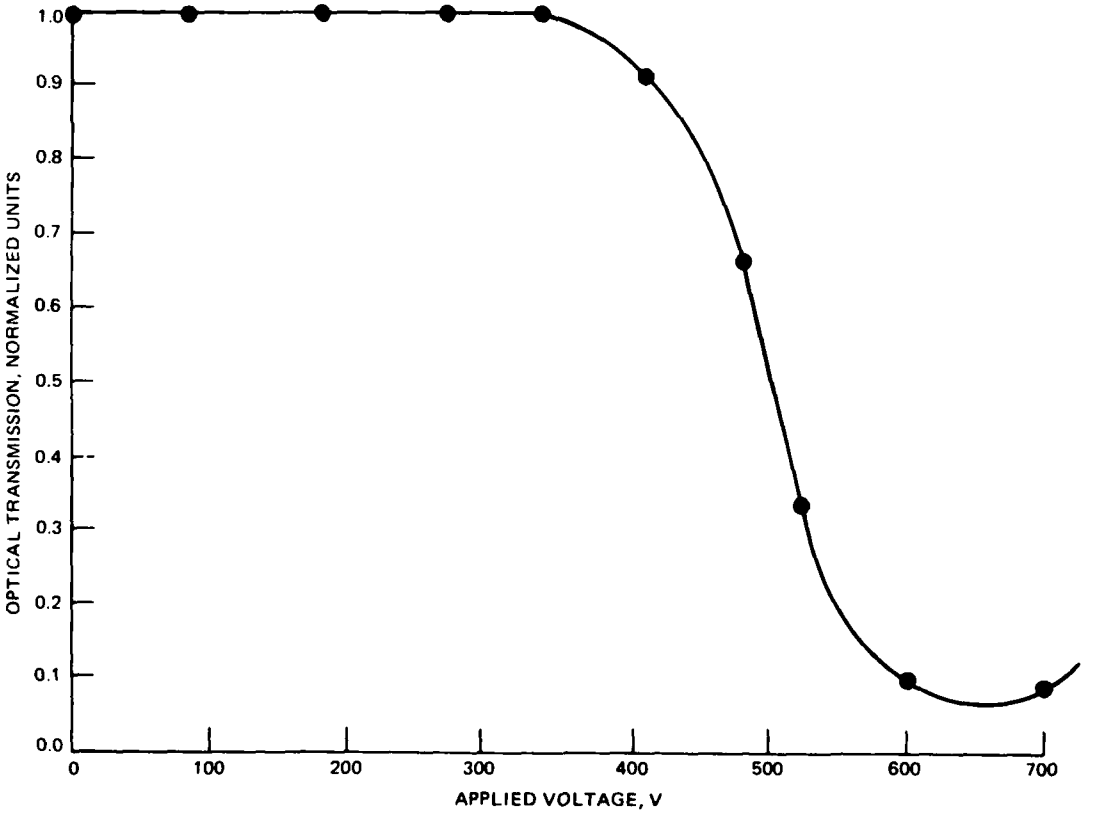

Figure D-3. Transmission characteristics of PLZT as a function of applied voltage.

observation and very positive result is that this transmission curve was relatively insensitive to angles of incidence up to ±20 deg. The curve in Fig. D-3 would thus indicate that biasing the PLZT wafer to 500 V dc and then swinging the voltage plus and minus 100 V about the dc bias may be a very desirable way to modulate the PLZT. In order to test this, a special-purpose electronic driver was designed and built at NOSC. This driver has the capability of electrically biasing the ceramic up to 600 V dc and swinging about this bias up to ±200 V for frequencies in the kilohertz range. The capacitance of the ceramic wafer is approximately 65 nF. The schematic diagram, Fig. D-4, shows the electronic driver circuitry, and Fig. D-5 shows the electronic biasing circuitry. Using this electronic driver and the 10-cm PLZT ceramic modulator, we have been able to demonstrate successful optical communications in the laboratory, using 0.633-μm light, for modulation frequencies between 5 and 24 kHz.

Figure D-6 shows how the signal level varies as a function of the applied dc bias voltage, with the ac swing voltage as the parameter for a 5-kHz modulation. These curves indicate the signal amplitude levels out between 500 and 600 V, indicating that a bias voltage in this range appears to be optimum for the ceramic wafer under test. It is also noted that the amplitude level can be increased by increasing the ac voltage swing. Plus and minus 150 V (300 V peak-to-peak) was the limit to which the present driver could be pushed with the 10-cm-diameter modulator. Figure D-7 depicts experimental data, similar to those presented in Fig. D-6, at a modulation frequency 18 kHz.

One last laboratory measurement made on the 10-cm PLZT ceramic wafer concerns the change of modulator capacitance with ceramic temperature. Shown in Fig. D-8 is a plot of modulator capacitance with temperature.

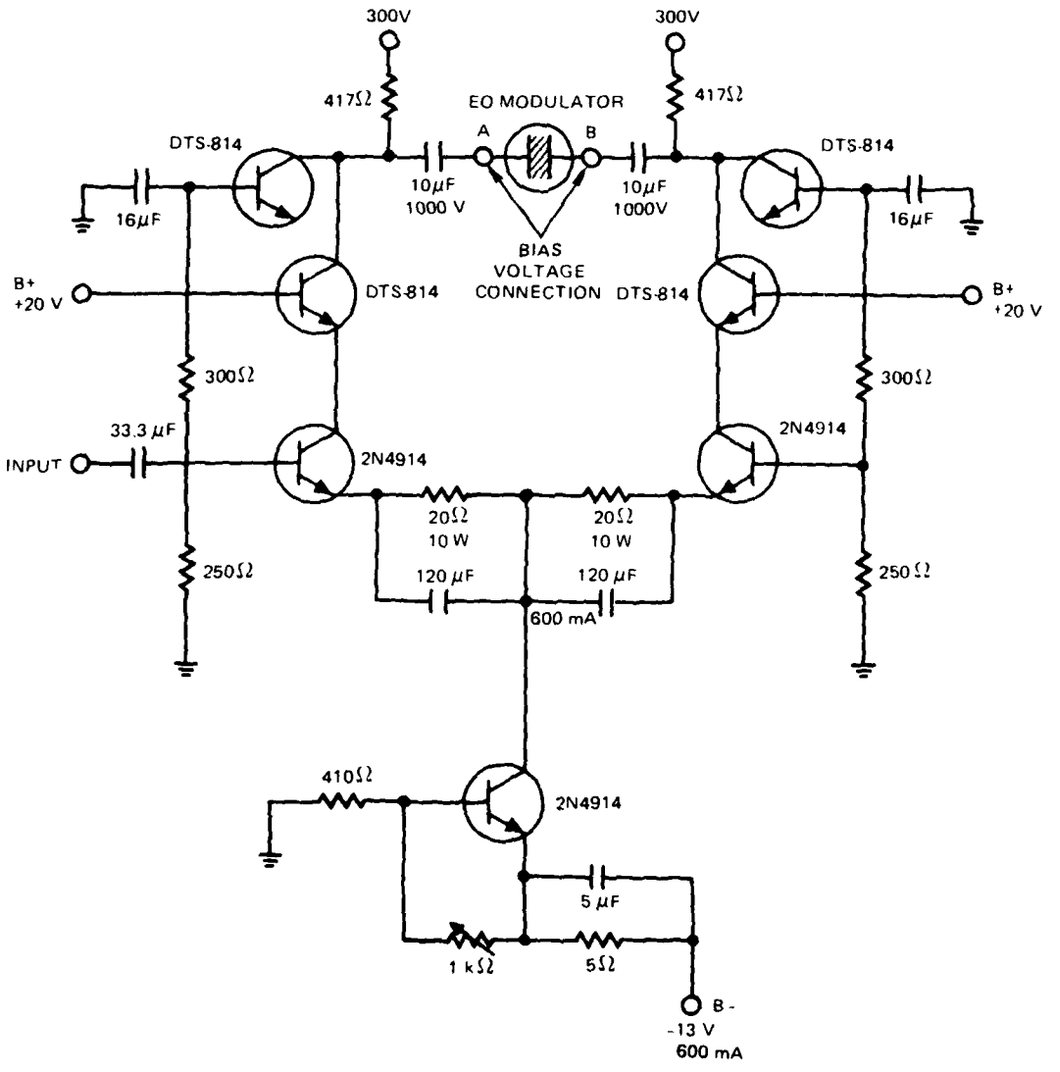

Figure D-4. Electronic driver modulator circuitry.

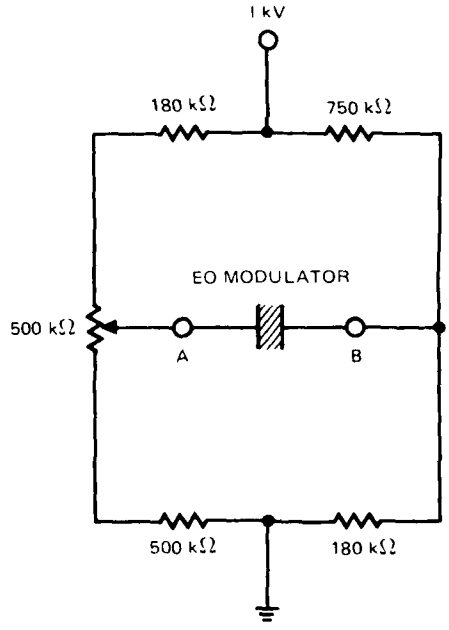

Figure D-5. Electronic driver biasing circuitry.

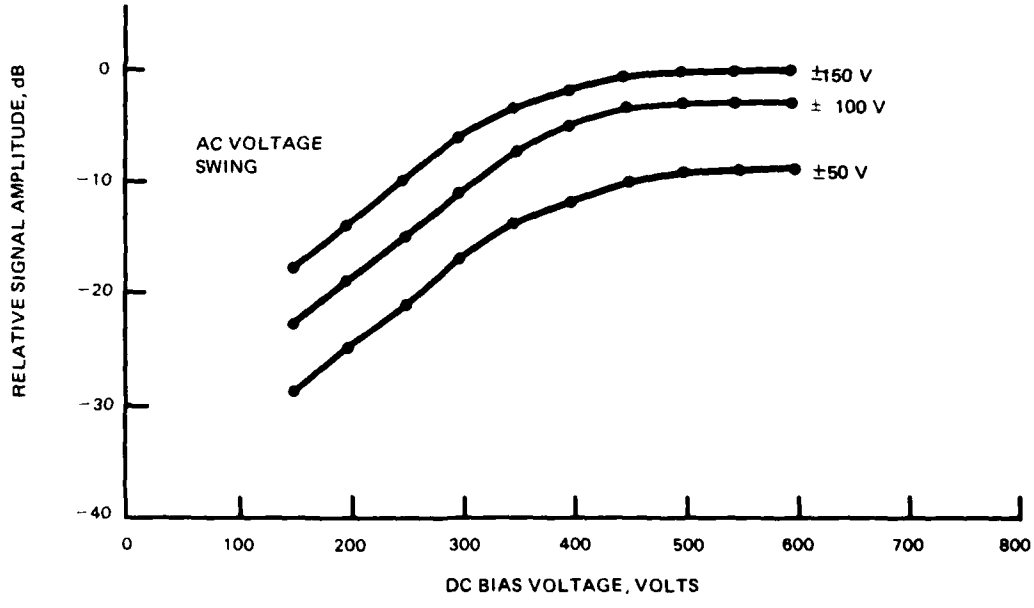

Figure D-6. Relative signal amplitude level versus dc bias voltage at 5-kHz modulation.

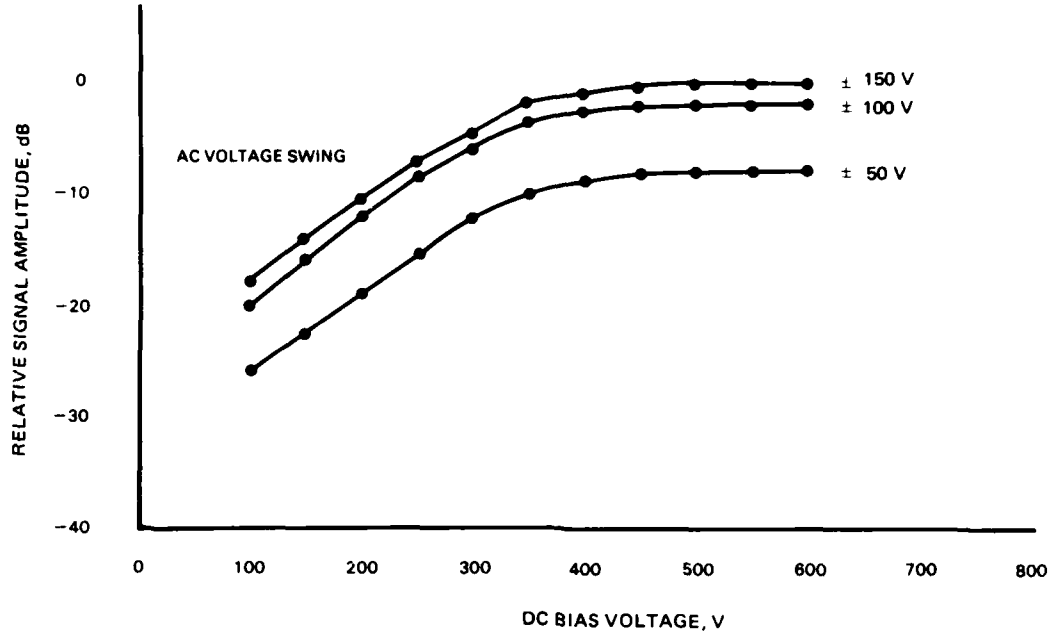

Figure D-7. Relative signal amplitude level versus dc bias voltage at 18-kHz modulation.

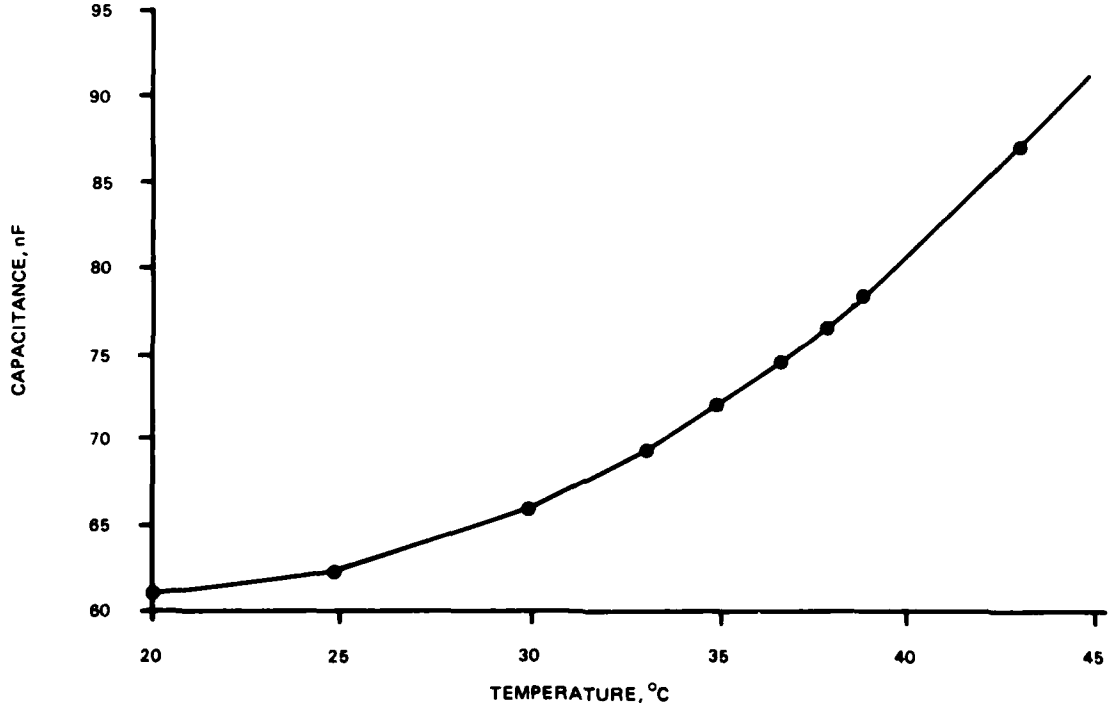

Figure D-8. Change in PLZT (10-cm) capacitance as a function of temperature.

APPENDIX E

LARGE-APERTURE MULTI-ELEMENT PLZT OPTICAL MODULATOR

This appendix presents a description of a large-aperture multi-element PLZT optical modulator developed and fabricated by Honeywell, Inc. for NOSC under NELEX 304 sponsorship.

BACKGROUND

As indicated, the high antenna gain normally associated with optical-quality corner-cube retroreflectors (typically 120 dB for a 5-cm aperture) is spoiled as a result of the degrading refraction effects of a randomly varying air-water interface. This, of course, results in a severe loss (many tens of dB) in the S/N level at the active-terminal receiver. In order for the optical retroreflector/modulator approach for air-to-underwater optical communications to have impact for realistic operating environments, it is necessary to compensate for the losses incurred at the air-water interface.

An examination of the S/N equations previously employed indicates there are a number of ways to gain back the losses at the interface. For example, increasing light source power levels, increasing detector sensitivity, reducing optical component transmission losses, or increasing the effective area of the retroreflector/modulator aperture are just a few of the obvious ways of increasing the system's performance. However, improvements of just a factor of 2 (3 dB) in light power levels, detector sensitivity, or optical transmission losses usually involve disproportionate increases in expenditures due to either the introduction of new technologies or improvements in existing technologies.

It was decided, as a first attempt, to gain back losses at the air-water interface by increasing the retroreflector/modulator aperture area. As a result of this decision, NELEX 304 sponsored the development and fabrication of a large-aperture optical modulator. Based on knowledge acquired at NOSC in the employment of optical modulators in past optical communications experiments, the decision to develop a large-aperture multi-element PLZT array modulator was made. The industrial company tasked to perform the work was Honeywell, Inc. of Minneapolis, Minnesota, under Contract No. N66001-79-C-0096.

STATEMENT OF WORK

The work to be performed by Honeywell, Inc. in the fabrication of a multi-element PLZT modulator array was as follows:

(Task 1: Fabricate, polish, anneal, and electrode 10-cm-diameter PLZT wafers.) The array will consist of thirty-seven (37) 10-cm-diameter PLZT modulators arranged in a closed-pack configuration to maximize the active modulator area (~68%). The composition to be used for the PLZT ceramic wafers is 9.5-65/35, where 9.5 is the % lanthanum and 65/35 is the zirconate/titanate ratio. Each wafer will be 0.36 mm thick. On the large surfaces of each wafer interdigital electrodes will be electroplated. Each electrode will be approximately 0.05 mm wide and the center-to-center spacing between electrodes will be 1.02 mm.

(Task 2: Bond PLZT wafers between glass plates, attach electrical contacts, and mount in protective ring.) The electroded PLZT wafers will be bonded between two fused silica plates of approximately 2.5 mm thickness using a resilient bonding agent. Fused silica glass plates assure good blue transmission. The bonding material used will be a transparent silicon gel possessing excellent shock-absorbent and sealant properties. A 0.13-mm-thick layer will be between the PLZT and glass on each side. The PLZT modulators will be mounted in protective plastic rings. Electrical connections will be provided by means of solderable terminals. Polarizing elements will not be bonded to the modulators but will be provided as separate components. These will be plastic, visible-spectrum polarizers (HN38) from Polaroid Corporation.

(Task 3: Finalize design and build array frame.) The array frame will be constructed of Delrin and will be of an opaque color. Each of the PLZT wafers mounted in the plastic protective sleeves will be easily inserted into the array frame. Final design considerations involve a watertight seal surrounding the electrical contacts to the PLZT lens elements. This can be most practically done with an RTV compound.

(Task 4: Test and evaluation of individual array elements.) The individual bonded PLZT modulators will be transparent from 0.4 to 7.0 μ. The frequency response of each modulator will be such that frequencies from 0 to beyond 10 kHz can be accommodated. The typical capacitance of each modulator element will be 0.06 μF with an operating voltage requirement of between 700 and 800 V for single-pass transmission. Laboratory testing will determine the following:

- Maximum transmission of each PLZT modulator element
- On-off ratio of each element
- Half-wave voltage of each element
- Capacitance of each element.

(Task 5: Final assembly and test.) The individual PLZT modulator elements will be mounted into the array frame. Electrical connections to each individual element will be made. The individual assembled elements will be electrically and optically tested to ensure performance prior to shipment.

(Task 6: Delivery.) The assembled array will be packaged and ready for delivery 168 days after date of contract. An informal technical report containing test results will be made 168 days after date of contract.

The program schedule is shown on next page.

HONEYWELL, INC. PROGRAM SCHEDULE FOR
FABRICATION OF MULTI-ELEMENT ARRAY MODULATOR

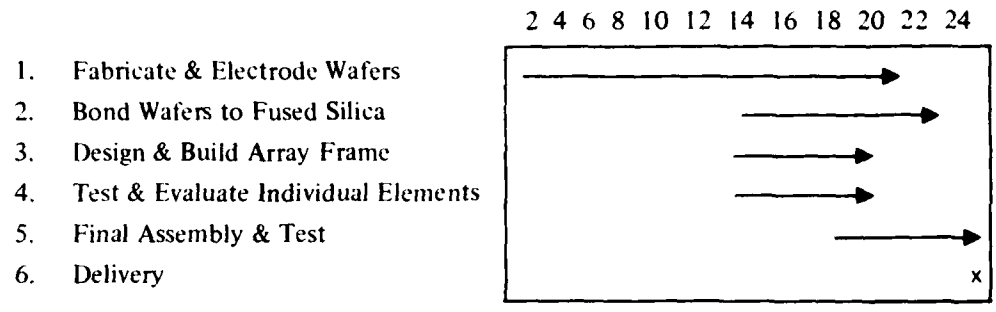

FINISHED MODULATOR ARRAY

The large-aperture multi-element PLZT modulator was completed on schedule and delivered to NOSC in early August 1979. The completed array is shown in Fig. E-1. As mentioned, the array consists of 37 PLZT ceramic modulators, each with a clear aperture of 10 cm. Figure 2 shows two of the 37 ceramic modulator elements with interdigital electrodes and plastic protective sleeves clearly delineated. Again it is noted that the individual PLZT modulators shown in Fig. E-2 can be easily retracted or inserted into the array frame shown in Fig. E-1.

There are six electrical connectors mounted on the array frame. Each connector is identified by a number from 1 to 6. This implies that each connector provides electrical continuity to either six or seven modulators within the array. Each connector has eight pins, which are identified by a letter from A to H. Pin H serves as ground relative to the other pins. Shown in Fig. E-3 is the wiring key for the array. As seen in this figure, each of the 37 circular slots within the array frame is identified by a number and a letter. For example, circular slot 3E is connected to connector 3, pin E. Table E-1 summarizes the individual PLZT modulator characteristics as measured by Honeywell, Inc. As seen in this table, there are measurements for 38 modulators, one being a spare. Each modulator is identified by a number from 1 to 38. In addition, each modulator has associated with it a boule number identifying which boule the ceramic modulator was fabricated from. There are four characteristics of interest listed in Table E-1 for each of the 38 modulators, namely, the on/off ratio, maximum transmission, half-wave voltage, and capacitance.

The on/off ratio represents the ratio of the "on" transmission to the "off" transmission for that modulator. That is, each modulator was placed between crossed polarizers made from HN38 Polaroid sheet and illuminated with a 5000-Å collimated light beam. The transmission in the off state (zero applied voltage) was measured as well as the transmission in the fully on state (voltage equal to the half-wave voltage). Dividing the on-state transmission value by the off-state transmission value and expressing as an optical density (O.D.) gives the on/off ratio. Note that measurements were made for single-pass transmission only. The maximum transmission (also referred to as the fully on-state transmission) corresponds to the transmission of the modulator and polarizers for single-pass transmission when the modulator is mounted between crossed polarizers and operating at the half-wave voltage.

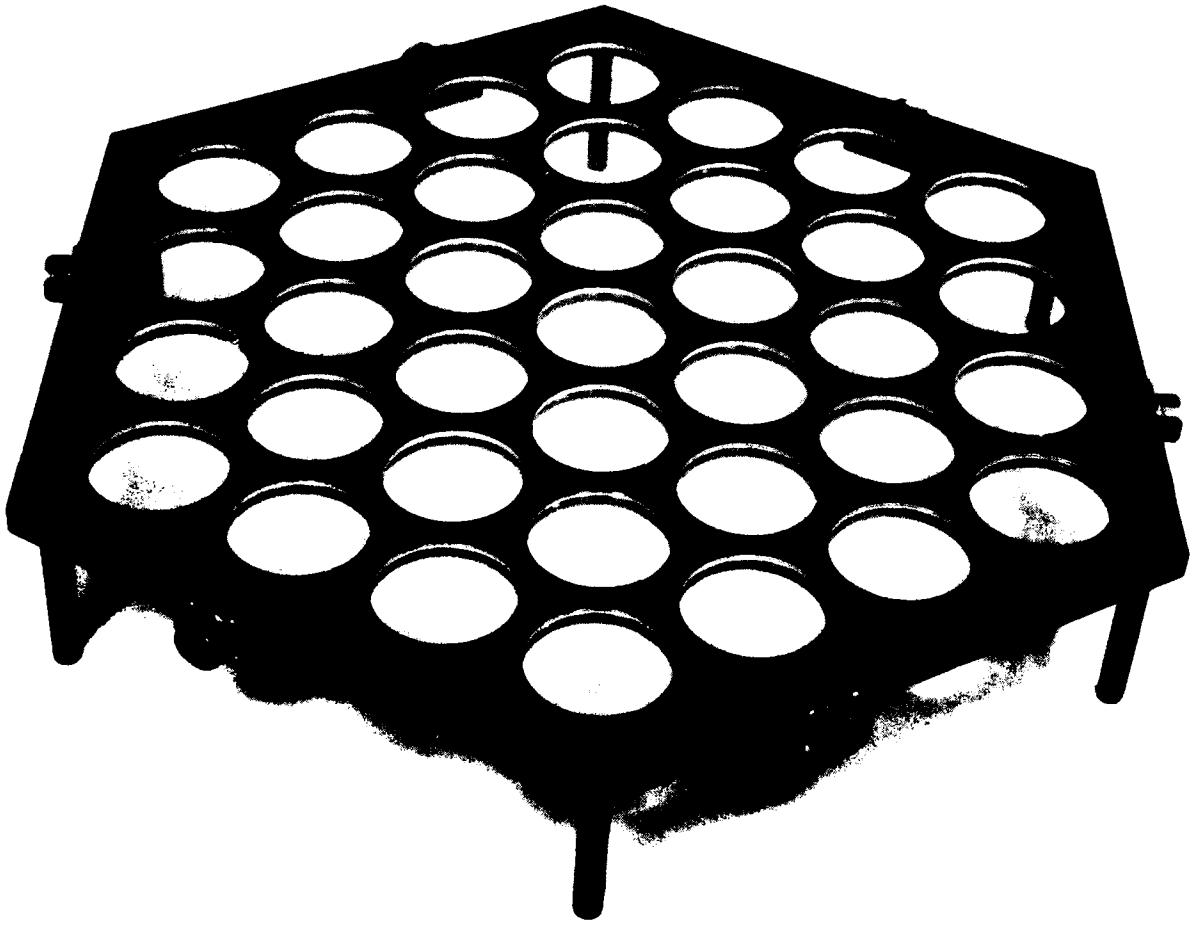

Figure E-1. Multi-element PLZT modulator array.

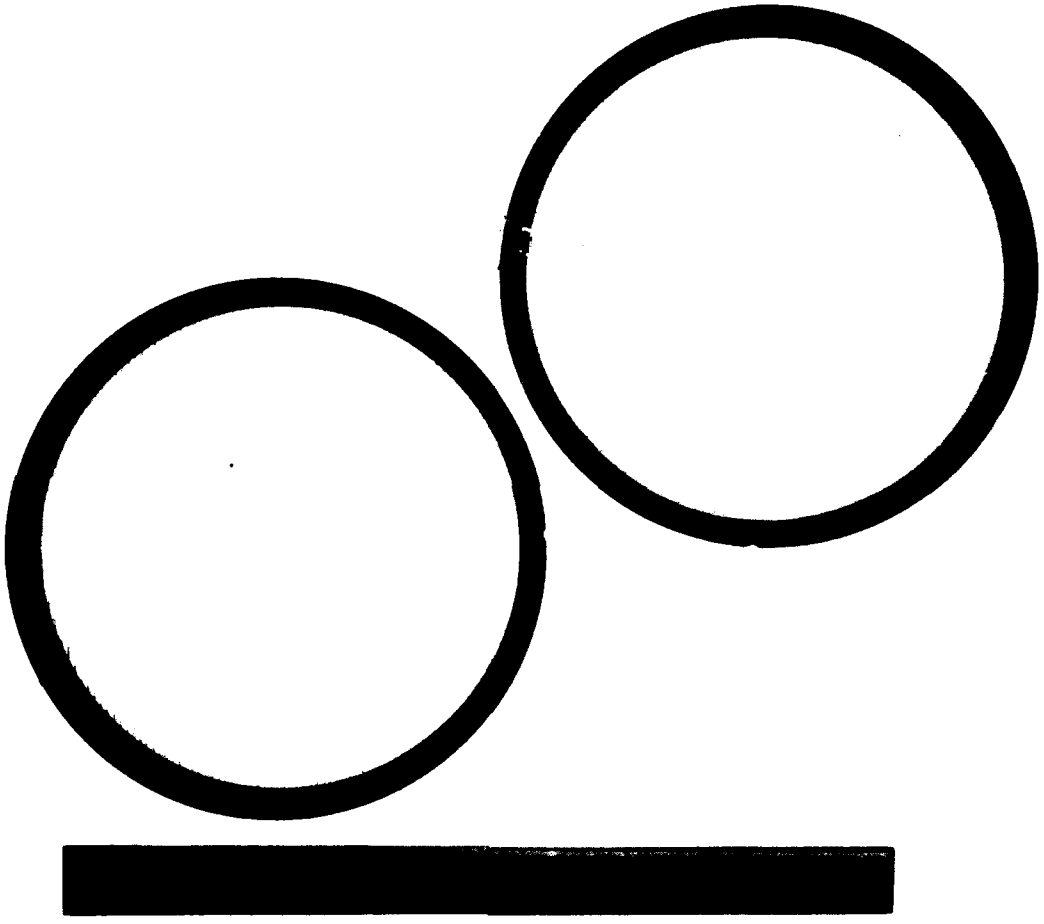

Figure E-2. Two 10-cm-diameter PLZT modulators.

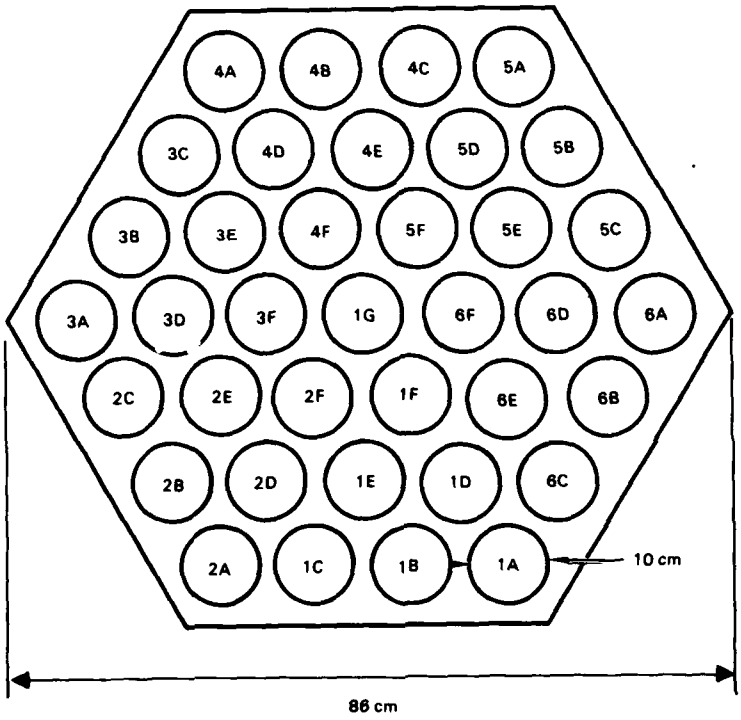

Figure E-3. Wiring key for the multi-element array.

The capacitance of each PLZT modulator was measured at 25°C.

There are certain safety considerations which must be taken into account when operating the modulator array. With the array energized to its rated voltage of 1000 V, and using a typical value of 50 nF as the capacitance for a 10-cm-diameter element, from the work equation, $W = \frac{1}{2} CV^2$, it can be shown that the stored energy per element is of the order of 0.025 J. Therefore, for the total 37 elements, the potential energy approaches 1 J, a potentially lethal hazard. In addition to affixing "high voltage" warning labels to the array modulator, it is recommended that a grounding plug be fabricated to bleed off any residual voltage that may be stored and also to prevent inadvertent charging of the array during maintenance work. It is also recommended that a matching set of sockets (Amphenol 22-235) be procured to make up grounding caps for the frame receptacles. Each pin should be connected to common through a 1000-ohm load resistor and the cap socket protected with a suitable potting compound. Deenergizing of wafers should always be accomplished through a current-limiting resistor, not lower than 500 ohms, or damage to the wafer electrodes can occur.

Wafer Number	Boule	On/Off Ratio, O.D.*	Maximum Transmission, %	Half-Wave Voltage, V	Capacitance, nF
1	3109-H2-1	4.15	18.0	950	63.5
2	3104-H6-1	4.10	19.0	860	63.3
3	3109-H2-1	4.15	18.6	960	62.9
4	3112-H4-1	3.77	18.3	840	62.8
5	3104-H6-1	4.05	18.4	850	65.3
6	2998-H4-2	3.92	18.0	825	64.4
7	2998-H4-2	4.12	17.8	820	64.4
8	3112-H4-1	4.00	18.2	850	63.4
9	3112-H4-1	4.00	17.0	850	64.4
10	3112-H4-1	4.10	18.5	850	62.8
11	3109-H2-1	4.10	17.5	950	63.0
12	3112-H4-1	4.05	18.6	850	64.3
13	3104-H6-1	3.72	18.0	860	64.6
14	2998-H4-2	3.92	17.5	825	65.1
15	3112-H4-1	4.05	18.0	850	63.4
16	3112-H4-1	4.05	18.4	850	64.7
17	2998-H4-2	3.66	18.7	825	63.0
18	3109-H2-1	4.10	17.5	950	64.2
19	3109-H2-1	3.68	17.6	950	63.4
20	3106-H4-1	3.96	18.3	860	65.4
21	3104-H6-1	3.92	19.0	860	65.2
22	3104-H6-1	4.15	18.8	860	64.9
23	3104-H6-1	3.72	18.8	860	66.0
24	3109-H2-1	4.10	18.0	950	65.5
25	3109-H2-1	4.05	18.0	950	65.8
26	3109-H2-1	3.96	18.0	950	65.3
27	3109-H2-1	3.96	18.2	955	63.4
28	3112-H4-1	4.10	17.8	850	65.1
29	3112-H6-2	4.10	17.2	845	65.9
30	2998-H4-2	3.64	17.0	825	66.5
31	3112-H6-2	4.19	17.6	845	66.8
32	3109-H2-1	4.22	17.0	950	65.5
33	3109-H2-1	4.10	16.8	955	64.4
34	2998-H4-2	4.10	16.8	820	67.6
35	3112-H6-2	4.00	15.5	845	64.5
36	2998-H4-2	4.00	18.3	825	64.1
37	2998-H4-2	3.59	16.0	820	65.5
38	3112-H4-1	4.22	13.0	850	64.6

* Optical density

Table E-1. Individual PLZT Wafer Characteristics.

APPENDIX F

BEAM-SPREADING LOSSES INCURRED AT THE AIR-WATER INTERFACE

A good quality corner-cube retroreflector has an antenna gain over 120 dB (~5 cm aperture) when illuminated with visible light. Placing such a retroreflector underwater and illuminating it with a light source located above the air-water interface would give rise to a retroreflected beam whose angular extent would greatly depend upon water wave activity characteristics at the interface. Hence, the high antenna gain of the retroreflector would be spoiled as a result of refraction at the randomly varying air-water interface. In this appendix a model for predicting the magnitude of losses incurred at the air-water interface due to beam broadening at a randomly varying air-water interface is developed. The approach will be to analyze the equivalent two-dimensional problem, that is, illuminate a two-dimensional corner cube located underwater near the interface with a collimated light beam and determine the variance in beam-spread angle as a function of air-water interface wave parameters. The problem will be treated as a random-variable problem.

The geometry depicted in Fig. F-1 will serve as a starting point. Shown in this figure is a two-dimensional corner-cube retroreflector located near the air-water interface. A sinusoidal wave of period P, amplitude A, and arbitrary phase δ exists at the interface. Mathematically, the wave height at any spatial position x is described by

$$y = A \sin(2\pi x/P + \delta) \tag{F-1}$$

whereas the wave slope is given by

$$dy/dx = 2\pi(A/P) \cos(2\pi x/P + \delta). \tag{F-2}$$

Tracing an arbitrary ray of light along the y-direction, it is seen that the ray is refracted at the interface, enters the corner cube and is reflected twice before emerging from the cube at a different spatial location, and then undergoes a second refraction at the interface. As a result of the translation of the ray within the corner cube, the ray will see a different wave slope as it exits the air-water interface. This implies the outgoing and incoming rays in air will not be parallel in general. Let x_i represent the x-coordinate of the incoming ray and x_o the x-coordinate of the outgoing ray. Let the radius of the corner cube be r_o. The index of refraction of air will be taken as unity and that of water will be 1.33. A number of angles are employed in Fig. F-1; however, the important angle of interest is the angle γ, which is a measure of how much the outgoing ray deviates in direction from the ideal retroreturn direction.

With the use of Snell's law of refraction, the incoming and outgoing rays obey the following equations at the interface,

$$\sin\theta = n \sin\phi \tag{F-3}$$

and

$$\sin\beta = n \sin(\alpha - \theta + \phi) \tag{F-4}$$

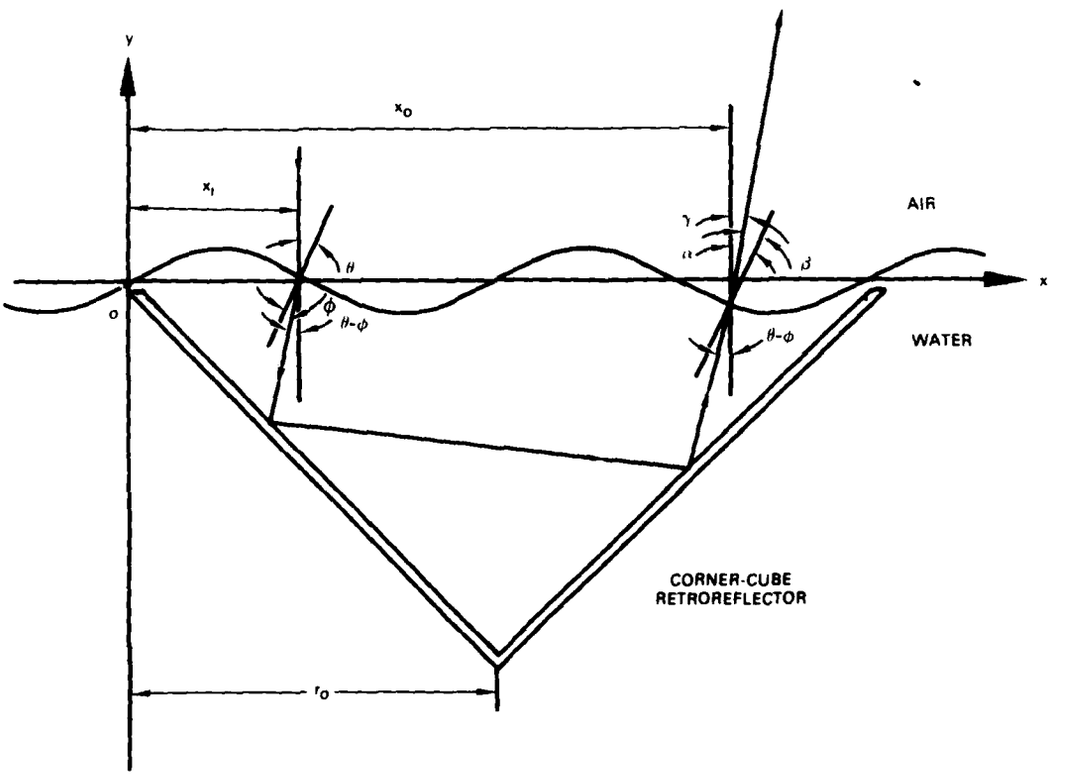

Figure F-1. Geometry for a two-dimensional corner-cube retroreflector near the air-water interface with wave activity.

where n = 1.33. From geometrical considerations

$$\gamma = \alpha - \beta \quad . \tag{F-5}$$

In addition,

$$\tan\theta = (dy/dx)_{x=x_i} \tag{F-6}$$

$$\tan\alpha = (dy/dx)_{x=x_o} \tag{F-7}$$

and

$$x_i = 2\, r_o \rho \tag{F-8}$$

$$x_o = 2 r_o (1 - \rho) \tag{F-9}$$

where $0 \leq \rho \leq 1$. To simplify the analysis the small-angle approximation will be invoked. This implies that the sine terms in the Snell's law equations may be replaced by their corresponding angle arguments. The small-angle approximation only applies for those cases in which the ratio of the wave amplitude to wave period is small. With the use of the preceding equations and the small-angle approximation, it can easily be shown that the angle γ is given by the following expression,

$$\gamma = 2\pi(n-1)(A/P)\,[\cos(4\pi r_o \rho/P + \delta) - \cos(4\pi r_o(1-\rho)/P + \delta)]. \tag{F-10}$$

Using the trigonometric identity

$$\cos(A) - \cos(B) = -2 \sin(\frac{A+B}{2}) \sin(\frac{A-B}{2}) \tag{F-11}$$

Eq. (F-10) can be rewritten in the following form

$$\gamma = 4\pi(n-1)\,(A/P) \sin(2\pi r_o/P + \delta) \sin(2\pi r_o/P - 4\pi r_o \rho/P)\ . \tag{F-12}$$

There are two quantities in the above equation which will be treated as random variables. They are δ and ρ, where

$$-\pi \leq \delta \leq \pi \tag{F-13}$$

$$0 \leq \rho \leq 1, \tag{F-14}$$

which implies

$$-1 \leq 1 - 2\rho \leq 1\ . \tag{F-15}$$

If δ and ρ are treated as random variables, then γ will also be a random variable. The first sine term in Eq. (F-12) contains information about the random position of the wave in relation to the corner-cube retroreflector, whereas the second sine term contains information about the relative position of the input ray to the corner cube. For simplicity the following substitutions are made,

$$z = \gamma$$
$$x = \delta/\pi$$
$$y = 1 - 2\rho$$
$$a = 2r_o / P$$
$$c = 4\pi\,(n-1)\,(A/P)\ .$$

This implies that Eq. (F-12) may be rewritten as follows:

$$z = c \sin(\pi a + \pi x) \sin(\pi a y) \tag{F-16}$$

where now

$$-1 \leqslant x \leqslant +1 \tag{F-17}$$

$$-1 \leqslant y \leqslant +1 \tag{F-18}$$

$$-c \leqslant z \leqslant +c \quad . \tag{F-19}$$

It will be assumed that the random variables x and y are uniformly distributed between -1 and +1. This implies that their corresponding probability density functions are given by

$$f_x(x) = \begin{cases} 1/2 & -1 \leqslant x \leqslant 1 \\ 0 & \text{otherwise} \end{cases} \tag{F-20}$$

$$f_y(y) = \begin{cases} 1/2 & -1 \leqslant y \leqslant 1 \\ 0 & \text{otherwise} \end{cases} \quad . \tag{F-21}$$

Our primary aim now is to determine the probability density function $f_z(z)$ associated with the random variable z. To do so, two new intermediate random variables will be introduced, namely, u and v, where

$$u = \sin(\pi a + \pi x) \tag{F-22}$$

$$v = \sin(\pi a y) \tag{F-23}$$

Equation (F-16) becomes

$$z = c\, u\, v \tag{F-24}$$

The probability density functions $f_u(u)$ and $f_v(v)$ associated with the random variables u and v, respectively, are given by (Ref. 11)

$$f_u(u) = \begin{cases} \pi^{-1} (1 - u^2)^{-1/2} & |u| < 1 \\ 0 & \text{otherwise} \end{cases} \tag{F-25}$$

$$f_v(v) = \begin{cases} (2\pi a)^{-1} (1 - v^2)^{-1/2} & |v| < \sin(\pi a) \\ 0 & \text{otherwise} \end{cases} \tag{F-26}$$

for $a \leqslant 1/2$ and

$$f_v(v) = \begin{cases} \pi^{-1} (1 - v^2)^{-1/2} & |v| < 1 \\ 0 & \text{otherwise} \end{cases} \tag{F-27}$$

for $a > \frac{1}{2}$. The first expression for $f_v(v)$ corresponds to the case when the corner-cube diameter is less than or equal to one-half a wave period. The second expression represents the case in which the retroreflector diameter is greater than one-half a wave period. For this analysis, only the latter expression for $f_v(v)$ will be of interest.

From Eq. (F-24) we recall the random variable z is a function of two random variables,

$$z = g(u,v) = c\,u\,v \quad . \tag{F-28}$$

If we introduce an auxiliary random variable w where

$$w = h(u,v) = u, \tag{F-29}$$

then the desired probability density function $f_z(z)$ may be obtained from the joint probability density function $f_{zw}(z,w)$ for z and w through the integral equation

$$f_z(z) = \int_{-\infty}^{\infty} f_{zw}(z,w)\,dw \quad . \tag{F-30}$$

See Ref. 11 for further details. The random variables u and v are independent; hence their joint density function $f_{uv}(u,v)$ is simply given by

$$f_{uv}(u,v) = f_u(u)\,f_v(v) \quad . \tag{F-31}$$

The joint probability density function $f_{zw}(z,w)$ is related to the joint density function $f_{uv}(u,v)$ through the following equation (Ref. 11)

$$f_{zw}(z,w) = f_{uv}(w,z/cw) \,/\, \left|J(w,z/cw)\right| \tag{F-32}$$

where J(u,v) is the Jacobian of the transformation given by Eq. (F-28) and (F-29). The Jacobian is given by

$$J(u,v) = \begin{vmatrix} \partial g/\partial u & \partial g/\partial v \\ \partial h/\partial u & \partial h/\partial v \end{vmatrix} = -c\,w \quad . \tag{F-33}$$

This implies

$$f_{zw}(z,w) = f_u(w)\,f_v(z/cw) \,/\, c\,|w| \tag{F-34}$$

which further implies

$$f_z(z) = \int_{-\infty}^{\infty} \frac{f_u(w)\,f_v(z/cw)}{c\,|w|}\,dw \quad . \tag{F-35}$$

The product of $f_u(w)$ and $f_v(z/cw)$ is nonzero only under the following set conditions:

$$\{ |w| < 1 \} \cap \{ |z/cw| < 1 \} = \{ |z/c| < w < 1 \} \cup \{ -1 < w < -|z/c| \},$$

which implies

$$f_z(z) = 2 \int_{|z/c|}^{1} \frac{dw}{\pi^2 cw \sqrt{1 - w^2} \sqrt{1 - z^2/c^2 w^2}} . \tag{F-36}$$

From a table of integrals (Ref. 12) we find

$$f_z(z) = (2/c\pi^2) K \left(\sqrt{1 - z^2 c^2} \right), \tag{F-37}$$

where K(q) is the complete elliptic integral. Given the probability density function $f_z(z)$, the mean value μ and the variance σ^2 can easily be determined. We find

$$\mu = \int_{-\infty}^{\infty} z f_z(z) dz = 0 \tag{F-38}$$

and

$$\sigma^2 = \int_{-\infty}^{\infty} (x-\mu)^2 f_z(z) dz = (4/\pi^2) c^2 (1/2)(1/2 + G), \tag{F-39}$$

where G is Catalan's constant (Ref. 12) and is given by

$$G = 0.915965594 \ldots$$

Substitution for c gives

$$\sigma^2 = 32(1/2 + G)(n - 1)^2 (A/P)^2. \tag{F-40}$$

For the standard deviation we thus obtain,

$$\sigma = 2.24(A/P) . \tag{F-41}$$

Equation (F-41) represents the standard deviation associated with beam spreading arising from the air-water interface only. The modulated retroreflectors described in this report have associated with them intrinsic beam spreading due to diffraction, which in turn depends on the diameter of the entrance aperture and optical quality of the modulator/retroreflector combination. It will be assumed that the probability density function describing beam spreading due to the intrinsic diffractive properties of a modulated retroreflector is independent of the probability density function associated with beam spreading from the air-water interface. Hence the probability density function describing beam spreading arising from both effects is simply the convolution of the individual probability density functions. This implies the variance associated with the total beam spread from both mechanisms is simply the sum of the individual variances of each mechanism. Let σ_o^2 represent the variance associated with

beam spreading due to the intrinsic diffractive properties of the modulated retroreflector and σ^2 the variance for the air-water interface [see Eq. (F-40)]. The total variance σ_t^2 for both processes is

$$\sigma_t^2 = \sigma_o^2 + \sigma^2 \tag{F-42}$$

and the standard deviation

$$\sigma_t = \sqrt{\sigma_o^2 + \sigma^2} \ . \tag{F-43}$$

For the case of a perfectly flat air-water interface (A/P=0) we have

$$\sigma = 0 \ , \tag{F-44}$$

which implies

$$\sigma_t = \sigma_o \ , \tag{F-45}$$

which corresponds to beam spreading due to the intrinsic diffractive properties of the modulated retroreflector only. In Appendix B the system equations for air-to-underwater optical communications using retromodulation techniques are presented. From these equations, it is obvious for the case of background-limited operation, the SNR is directly proportional to the square of the received signal power, P_s, which in turn is inversely proportional to the solid angle of the modulated retroreflector return light cone. For the case of surface wave activity that gives rise to beam spreading equivalent to the two-dimensional problem previously described, the SNR satisfies the following relation:

$$\text{SNR} = K/\sigma_t^2 \ , \tag{F-46}$$

where K is a constant of proportionality, whereas

$$\text{SNR} = K/\sigma_t^4 \tag{F-47}$$

for the three-dimensional problem. Let us define the quantity R as the ratio of the SNR in the presence of wave activity to the SNR in the absence of wave activity, that is,

$$R = \frac{\text{SNR}_{\text{wave activity}}}{\text{SNR}_{\text{no wave activity}}} \tag{F-48}$$

with all other quantities remaining the same. For the two-dimensional problem we find

$$R = \sigma_o^2/(\sigma_o^2 + \sigma^2) \tag{F-49}$$

and for the three-dimensional problem

$$R = \sigma_o^4/(\sigma_o^2 + \sigma^2)^2 \ . \tag{F-50}$$

Shown in Fig. F-2 and F-3 are parametric plots of $10 \log_{10}(R)$ versus (A/P) for the two- and three-dimensional cases, respectively. The parameter is σ_o, the standard deviation associated with beam spreading due only to the modulated retroreflector. The quantity $10 \log_{10}(R)$ represents the additional losses in decibels introduced by the air-water interface over and above the losses already due to the intrinsic diffractive properties of the modulated retroreflector. It is noted that for a modulated retroreflector with very high antenna gain, that is, small σ_o, the air-water interface has a very large effect on introducing additional beam-spreading losses. If, however, the antenna gain is small, that is, large σ_o, then the air-water interface has a much smaller effect on spreading losses. For example, for the two-dimensional case, if the surface wave amplitude-to-period ratio is, say, 1/100, then the air-water interface would introduce an additional 75-dB loss over that for a flat interface for a modulated retroreflector with a σ_o of 8 arc-s. For a modulated retroreflector with a σ_o, of, say, 1 deg, the additional spread losses due to the air-water interface would only be 4 dB.

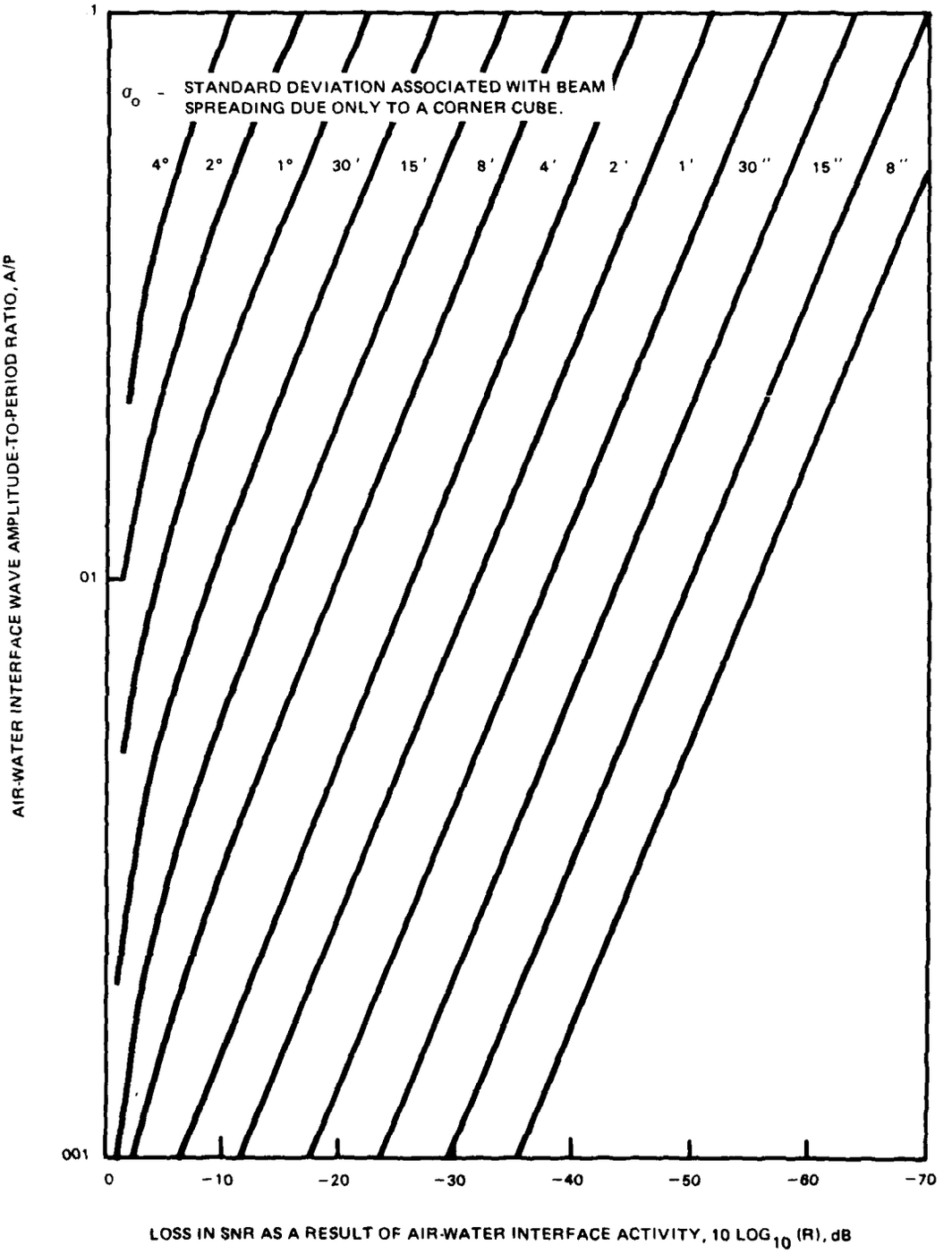

Figure F-2. Beam-spread losses due to wave activity at the air-water interface for two dimensions.

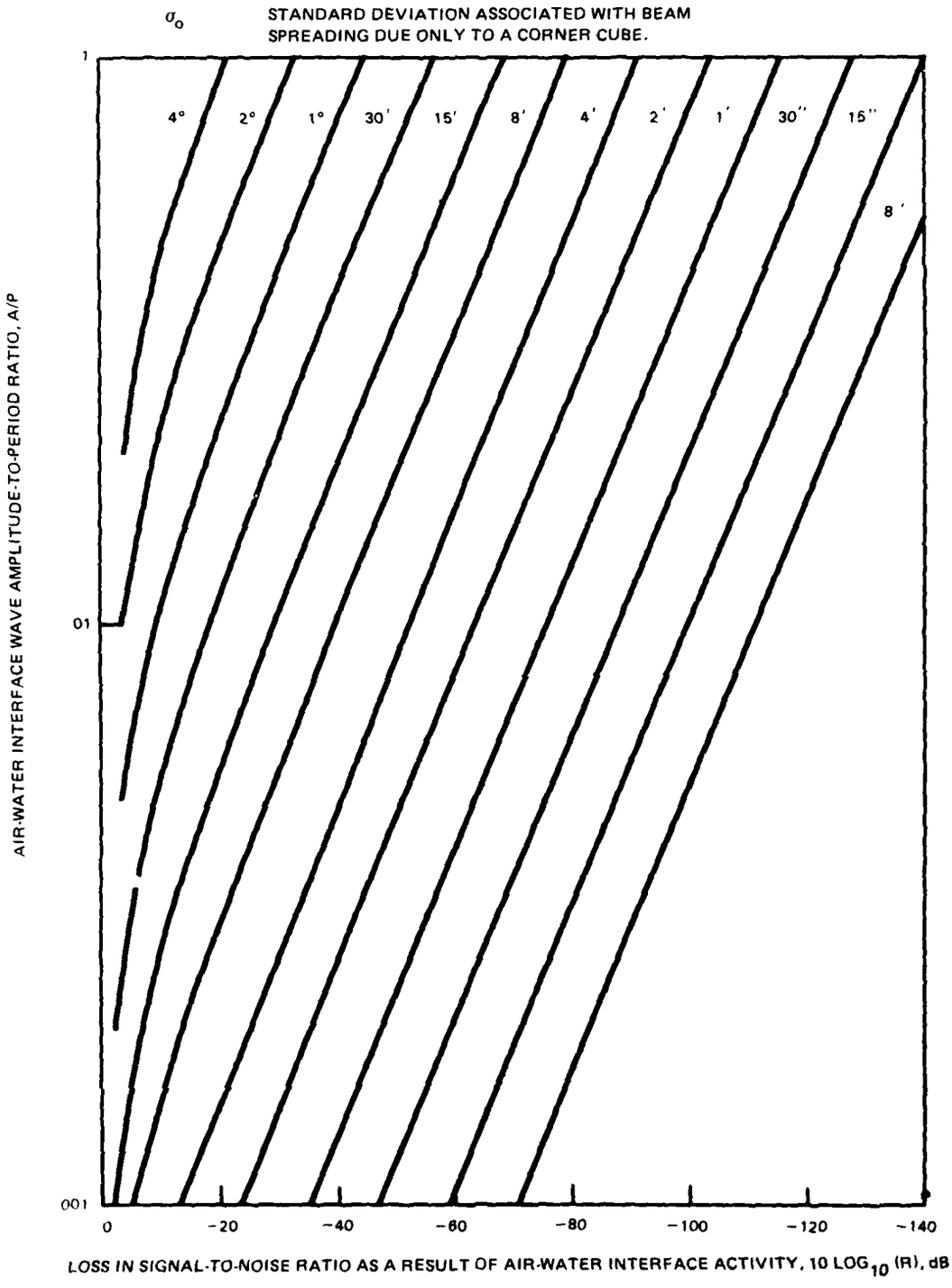

Figure F-3. Beam-spread losses due to wave activity at the air-water interface for three dimensions.

INDEX OF PHOTOGRAPHS

Figure	NOSC File Number
4	LRO 2247-12-76A
6	LRO (A) 66-6-77
9	LRO (A) 784-7-80
10	LRO (A) 783-7-80
17	LRO (A) 361-3-78
27	LRO 3701-10-78B
C-4	LRO 4590-12-78B
E-1	(Honeywell photograph)
E-2	LRO (A) 632-7-79

END

DATE
FILMED
4-82

DTIC